Selective and efficient synthesis of ethanol from dimethyl ether and syngas

Rasmussen, Dominik Bjørn

Publication date:
2015

Document Version
Publisher's PDF, also known as Version of record

Selective and Efficient Synthesis of Ethanol from Dimethyl Ether and Syngas

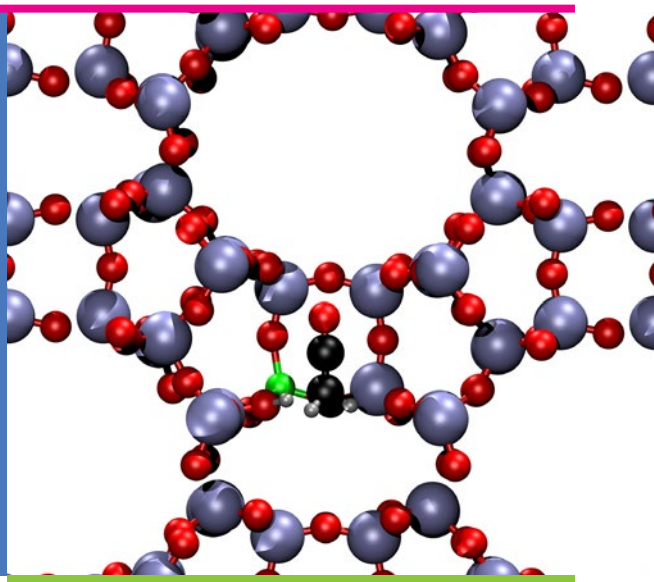

Dominik Bjørn Rasmussen

PhD Thesis

June 2015

DTU Chemical Engineering
Department of Chemical and Biochemical Engineering

Technical University of Denmark

Selective and Efficient Synthesis of Ethanol from Dimethyl Ether and Syngas

PhD Thesis

Denmark, 2011-2015

Written by

Dominik Bjørn Rasmussen

Combustion and Harmful Emission Control

Department of Chemical and Biochemical Engineering

Technical University of Denmark

Supervised by

Assistant Professor Jakob Munkholt Christensen

Doctor Burçin Temel McKenna

Doctor Felix Studt

Doctor Poul Georg Moses

Associate Professor Jan Rossmeisl

Associate professor Anders Riisager

Professor Anker Degn Jensen

I dedicate this thesis to my parents and my sister,
who always supported me in my endeavors

DTU Chemical Engineering
Department of Chemical and Biochemical Engineering

Abstract

The modern society is heavily dependent on fossil fuels, which are a limited resource. The transport sector is responsible for a large share of the combined fuel consumption and there is a strong political and environmental incentive to make it less dependent on oil. Ethanol (EtOH) can play an important role as a gasoline additive or substitute and a catalytic process has been demonstrated, in which dimethyl ether (DME) produced from synthesis gas is converted to methyl acetate (MA), which is subsequently converted to EtOH and methanol (MeOH). MeOH can afterwards be easily converted to DME, using well-established processes. Syngas can be produced from biomass, making the entire process sustainable and environmentally friendly. The main benefit of this method is its unprecedented selectivity towards EtOH, while MeOH, the primary by-product, and the unreacted syngas are easily recycled. The reaction of MA to EtOH and MeOH is facile and can be performed efficiently using known technologies. The formation of MA is on the other hand difficult because no stable and active catalyst have been identified for the reaction yet. Mordenite has been shown to be the most active catalyst for the reaction but it is not sufficiently active or stable to be applied industrially.

In this PhD project, the formation of MA over Mordenite has been studied experimentally and by density functional theory (DFT) calculations. The DFT study of the reaction path has shown that ketene is a reaction intermediate, a result with has been confirmed experimentally using mass spectroscopy. Ketene is a reactive molecule, which easily forms polymers. Consequently, its presence in the catalyst may be one of the reasons for the rapid deactivation.

Additionally, it was demonstrated by DFT calculations that MA is primarily formed in the side pockets of Mordenite and that the reaction of CO with methyl groups is the rate limiting reaction step. Thus, in contrast to the previous DFT studies, the DFT model developed here is fully consistent the experimental results.

An experimental study of the reaction kinetics has shown that MA inhibits the reaction. A kinetic model, taking this effect into account, was developed and it could accurately describe the dependence of the reaction rates on the amount of catalyst and the partial pressures of the reactants. The product inhibition of the reaction rate makes it difficult to scale the process up, as

it sets a limit on the maximum concentration of MA in the catalyst, relatively to the concentrations of the reactants.

A study of the deactivation rate has revealed that for a fixed reaction rate, the deactivation rate of the catalyst increases with increasing DME concentration; for a fixed DME concentration in the feed, the deactivation rate decreases with increasing MA concentration. However, the precise connection is still unknown.

The results of this PhD project contribute significantly to the understanding of the reactions taking place on Mordenite during MA synthesis and form a firm foundation for the future studies.

Resumé

Det moderne samfund er stærkt afhængigt af fossile brændstoffer som er en begrænset ressource. Transportsektoren står for en stor del af det samlede brandstofforbrug og der er et stærkt miljømæssigt og politisk incitament for at gøre den mindre afhængig af olie. Ætanol (EtOH) kan fungere som et benzinsubstitut og en katalytisk proces er blevet demonstreret, hvori dimetylæter (DME) fremstillet af syntesegas omdannes til metylacetat (MA), der efterfølgende omdannes til EtOH og metanol (MeOH). MeOH kan derefter nemt omdannes til DME ved brug af kendte teknologier. Syntesegas kan fremstilles af biomasse og dermed kan hele processen være bæredygtig og miljøvenlig. Fordelen ved denne metode er dens enestående selektivitet for EtOH, mens MeOH, det primære biprodukt, og ikke-reageret syntesegas er nemme at genbruge. Omdannelsen af MA til EtOH er nem og kan udføres effektivt ved brug af kendte teknologier. Fremstillingen af MA er til gengæld besværlig, da det endnu ikke er lykkedes at finde en effektiv katalysator for denne reaktion. Mordenit er blevet vist at være den mest aktive katalysator for reaktionen, men den er ikke tilstrækkelig aktiv eller stabil til at blive brugt industrielt.

I dette PhD-projekt blev dannelsen of MA over Mordenit undersøgt eksperimentelt og vha. tæthedsfuntionalteori-beregninger (DFT). DFT-studiet af reaktionsvejen har vist, at keten er et reaktionsmellemprodukt, et resultat som er blevet bekræftet eksperimentelt vha. massespektroskopi. Keten er et meget reaktivt molekyle, der nemt danner polymerer. Af denne grund kan dets tilstedeværelse i katalysatoren, være én af årsagerne til den hurtige deaktivering.

Desuden, blev det demonstreret med DFT-beregninger at MA hovedsageligt dannes i lommerne af Mordenite og at reaktionen af CO med metylgrupperne er det ratebestemmende reaktionstrin. Dermed, i modsætning til de tidligere DFT-studier, den DFT-model, der blev udviklet her er fuldt konsistent med de eksperimentelle resultater.

Et eksperimentalt studie af reaktionskinetikken har vist, at MA inhiberer reaktionen. En kinetisk model, der tager hensyn til denne effekt, blev udviklet og kunne nøjagtigt beskrive reaktionsratens afhængighed af katalysatorens masse og af reaktanternes partialtryk. Produktinhibering af reaktionsraten gør det svært at skalere processen op, da den sætter en grænse for den maksimale koncentration af MA i katalysatoren i forhold til koncentrationen af reaktanterne.

Et studie af deaktiveringsraten has afsløret, at for en konstant reaktionsrate, deaktiveringsraten stiger med stigende DME koncentration; for en konstant DME koncentration i katalysatorlejet,

aftager deaktiveringsraten for stigende MA koncentration. Den præcise sammenhang er dog stadig væk ikke kendt.

Resultaterne opnået i dette PhD-projekt bidrager betragteligt til forståelsen af de reaktioner der sker på Mordenitkatalysatoren under MA-syntesen og danner et solidt fundament for fremtidige studier.

Preface

This thesis is submitted in candidacy for the PhD degree at the Technical University of Denmark (DTU). The work has been carried out at DTU at the Department of Chemical and Biochemical Engineering (KT) in the research group Combustion and Harmful Emission Control (CHEC) and at the Center for Interface Science and Catalysis (SUNCAT), which is a partnership between the National Accelerator Laboratory (SLAC) and the Department of Chemical Engineering at Stanford University. Professor Anker Degn Jensen from KT has been the main supervisor, with Assistant Professor Jakob Munkholt Christensen from KT, Burçin Temel McKenna from Haldor Topsøe A/S, Felix Studt from SUNCAT, Poul Georg Moses from Haldor Topsøe A/S, Jan Rossmeisl from the Department of Physics at DTU, and Anders Riisager from the Department of Chemistry at DTU as co-supervisors.

I gratefully acknowledge the funding from DTU and the Catalysis for Sustainable Energy (CASE) initiative funded by the Danish Ministry of Science, Technology and Innovation, and the support from Haldor Topsøe A/S.

I would like to thank my supervisors for their guidance during the project. I am most grateful to Jakob Munkholt Christensen for his excellent supervision and infinite support with all aspects of my work. Also, I thank my fellow PhD students and close friends, Anna Trubetskaya and Joachim Bachmann Nielsen, for making my time at KT a very pleasant experience. I also wish to thank the members of the PhD lunch club at KT; our lunches were a nice break from work. Finally, I would like to thank my family and friends for their support.

Kgs. Lyngby, Denmark, May 2015

List of Publications & Conference Contributions

Articles Published in Peer-reviewed Journals

Dominik B. Rasmussen, Jakob M. Christensen, Burcin Temel, Felix Studt, Poul Georg Moses, Jan Rossmeisl, Anders Riisager, and Anker D. Jensen, ”*Ketene as a Reaction Intermediate in the Carbonylation of Dimethyl Ether to Methyl Acetate on Mordenite*”, *Angewandte Chemie International Edition,* 12 MAY 2015, DOI: 10.1002/anie.201410974

Articles in Preparation

Dominik B. Rasmussen, Jakob M. Christensen, Burcin Temel, Felix Studt, Poul Georg Moses, Jan Rossmeisl, Anders Riisager, and Anker D. Jensen, ”Reaction Mechanism of Dimethyl Ether Carbonylation to Methyl Acetate on Mordenite – A Combined DFT/Experimental Study”, To be submitted, 2015

Oral Conference Contributions

Dominik B. Rasmussen, Jakob M. Christensen, Burcin Temel, Felix Studt, Poul Georg Moses, Jan Rossmeisl, Anders Riisager, and Anker D. Jensen, ”*Ketene as a Reaction Intermediate in the Carbonylation of Dimethyl Ether to Methyl Acetate on Mordenite*”, To be given at the 24th North American Meeting (NAM) of the Catalysis Society, June 2015

Dominik B. Rasmussen, Jakob M. Christensen, Burcin Temel, Felix Studt, Poul Georg Moses, Jan Rossmeisl, Anders Riisager, and Anker D. Jensen, ”*Ketene as a Reaction Intermediate in the Carbonylation of Dimethyl Ether to Methyl Acetate on Mordenite”,* To be given at the XII European Congress on Catalysis (EuropaCat), September 2015

Poster Conference Contributions

Dominik B. Rasmussen, Jakob M. Christensen, Burcin Temel, Poul Georg Moses, Jan Rossmeisl, Anders Riisager, and Anker D. Jensen, ”A DFT Study of Dimethyl Ether Carbonylation on Mordenite”, Presented at the 23rd North American Meeting (NAM) of the Catalysis Society, June 2013

Dominik B. Rasmussen, Jakob M. Christensen, Burcin Temel, Poul Georg Moses, Jan Rossmeisl, Anders Riisager, and Anker D. Jensen, ”A DFT Study of Dimethyl Ether Carbonylation on Mordenite”, Presented at the XI European Congress on Catalysis (EuropaCat), September 2013

Dominik B. Rasmussen, Jakob M. Christensen, Burcin Temel, Poul Georg Moses, Jan Rossmeisl, Anders Riisager, and Anker D. Jensen, ”A DFT Study of Dimethyl Ether Carbonylation on Mordenite”, Presented at the 16th Nordic Symposium on Catalysis, June 2014

Table of Contents

1 Introduction

In this chapter an introduction to the DME carbonylation on Mordenite is given. The state of the knowledge about the reaction kinetics and catalyst deactivation when the project was started is summarized. Also, a scope of the PhD project is defined.

1.1 Background of the study

The global economy and modern society are heavily dependent on stable oil prices and supply. Currently, most of the produced transportation fuel is of fossil origin and its continuous use is thereby not sustainable. The steadily increasing prices of fuel and the risk of supply disruptions are factors making renewable fuels an interesting option. Ethanol (EtOH) is a promising alternative to oil derivatives as a transportation fuel [1-3]. It is produced industrially by fermentation of sugars and celluloses or through a reaction of ethylene with steam. Catalytic conversion of syngas to EtOH is a desirable process as it would be more energy-efficient and feedstock-flexible than the other methods. A number of catalysts can convert syngas to EtOH and other higher alcohols (HA) directly, in one step [4-20]; however, their activity as well as selectivity towards ethanol is fairly low. Alternatively, a two-step process can be used, in which DME, efficiently formed from syngas [21], and CO react to methyl acetate (MA) that in turn is converted to methanol (MeOH) and EtOH [22-26]. MeOH can afterwards be easily converted to DME, using well-established processes [21]. Haro et al. showed that conversion of biomass to ethanol, using the two-step process, could be cost-competitive in the near future, in comparison to the fermentation methods [27, 28].

Conversion of DME and syngas to MA proceeds as:

$$CO + CH_3OCH_3 \rightarrow CH_3COOCH_3 \quad \Delta G(438\ K) = -51.0\ kJ/mol \quad K = 1.21 \cdot 10^{6} \qquad (1)$$

The reaction is not limited by the thermodynamics and at equilibrium it would be completely shifted towards the products. The reaction is catalyzed by acidic zeolites, such as H-Mordenite (H-MOR) [29-31], H-ZSM-35 [24], and Keggin-type heteropolyacids [24, 32, 33]. These catalysts are highly selective (> 94 mol %) for DME carbonylation to MA at temperatures 423 K - 463 K. MA is hydrogenated to methanol (MeOH) and EtOH using a hydrogenation catalyst (Cu/ZnO, $Cu/ZnO/Al_2O_3$, Rh/SiO_2, Cu/CeO_2) [22-26], according to the reaction:

$$CH_3COOCH_3 + 2H_2 \rightleftharpoons CH_3CH_2OH + CH_3OH \quad \Delta G(438\ K) = 0.72\ kJ/mol \quad K = 8.20 \cdot 10^{-1} \qquad (2)$$

This reaction is somewhat limited by the thermodynamical equilibrium, so a surplus of hydrogen is needed to achieve a high conversion of MA. The DME carbonylation catalyst can be combined with the hydrogenation catalyst in a dual bed reactor and the reported selectivity of these systems towards MeOH and EtOH are around 51 mol % (on C basis) and 42 mol %, respectively [22-26]. The principal challenge that needs to be solved, before this method can find industrial use, is an increase of the rate of MA synthesis; the following hydrogenation of MA to MeOH and EtOH is facile.

In this study we only investigate carbonylation of DME on H-MOR, which is the most active zeolite catalyst for carbonylation of DME [29-31]. Liu et al. reported that H-ZSM-35 has a similar initial activity to that of H-MOR but a higher long-term stability [24]. The experiments were performed in a single bed reactor, and after 20 h on stream, the conversion of DME on H-MOR decreased to 5% while the conversion of DME on H-ZSM-35 remained stable for 32 h. The coke deposition rates for H-MOR and H-ZSM-35 were measured to 47 μmol C/gh and 13 μmol C/gh, respectively, showing that H-ZSM-35 also deactivates, although at a lower rate. It should be mentioned that these experiments were performed at a temperature higher by 38 K than in the previous work (performed at 438 K), making a direct comparison difficult. However, H-ZSM-35 may be an interesting alternative to H-MOR.

1.2 Structure of Mordenite

Table 1 shows the parameters of the unit cell of natural Mordenite [34]. For purely siliceous framework, the space group of MOR is Cmcm and the unit cell contains 96 Si atoms and 48 O atoms. There are 4 unique sites that are occupied by Al or Si. They are called T1, T2, T3 and T4. A substitution of Si with Al lowers the symmetry to Pbcn [35] and induces a charge imbalance, which is compensated by protons (Brønsted acid sites are formed), alkaline cations (Na, K) or alkaline-earth cations (Mg, Ca, Sr). Additionally, the channels of Mordenite contain various amounts of water.

There are three types of cavities in Mordenite: a) the main channel, parallel to the c-axis and circumscribed by 12 Si atoms (a 12 membered ring = 12-MR), b) a smaller 8-MR, parallel to 12-MR and c) the so-called side pockets, parallel to the b-axis, which are also 8-MR. The side pockets can be entered only from the main channel but do not provide connection between adjacent channels (maximum diameter of sphere that can diffuse along the b-axis is 2.95 Å). Figure 1 shows 12-MR and a side-pocket. In the following the side-pocket will be called 8-MR.

Table 1. Experimentally determined unit cell parameters of natural Mordenite.

Space Group:	Cmcm		
Chemical formula:	$\|Na^{+}_{8}(H_2O)_{24}\|$ $[Al_8Si_{40}O_{96}]$-MOR		
Cell Parameters:			
	a = 18.256 Å	b = 20.534 Å	c = 7.542 Å
	α = 90.000°	β = 90.000°	γ = 90.000°
	Volume =	2827.26 $Å^3$	
Maximum diameter of sphere that can diffuse along:		a: 1.57 Å b: 2.95 Å	c: 6.45 Å

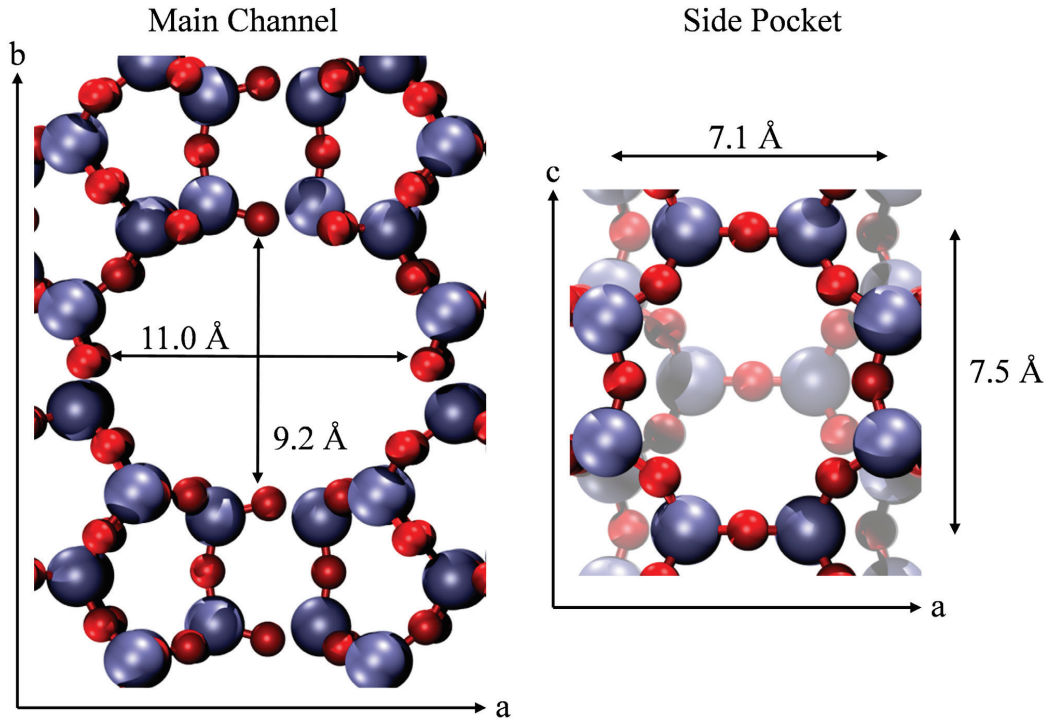

Figure 1. Left: View of the main channel along the c-axis. Right: View of the side pocket mouth along the b-axis. Oxygen – red, Silicon – blue.

1.3 DME carbonylation on H-MOR

Carbonylation of DME on Mordenite involves an induction period of around 4-6 hours followed by a steady-state phase [24, 29-31]. Figure 2 (copied from [31]) shows the synthesis rates of MeOH and MA on H-MOR measured for around 8 h (28 ks). During the induction period of 4.2 h (15 ks), the rate of MA formation increases to its maximum value and appears constant for the rest of the experiment (3.6 h, 13 ks). Figure 3 (copied from [24]) shows the synthesis rates of MA on H-MOR and H-ZSM-35 measured for 20 h and 32 h, respectively. The induction period for H-MOR is around 5 h and afterwards a significant deactivation is observed. The results shown in the two figures are not directly comparable because the experiments were performed at different temperatures, but the trends are similar. During the induction period MA synthesis occurs via following reaction network [29, 31]:

$$CH_3OCH_3 + [SiO(H)Al] \rightleftharpoons CH_3OCH_3\text{-}[SiO(H)Al] \quad (3)$$

$$CH_3OCH_3\text{-}[SiO(H)Al] \rightleftharpoons [SiO(CH_3)Al] + CH_3OH \quad (4)$$

$$CH_3OH + [SiO(H)Al] \rightleftharpoons [SiO(CH_3)Al] + H_2O \quad (5)$$

Reactions (3)-(5) show that water is formed when the Brønsted acid sites on the zeolite are methylated. Reaction (5) is too slow to remove all MeOH molecules before they leave the zeolite, resulting in MeOH signal in Figure 2.

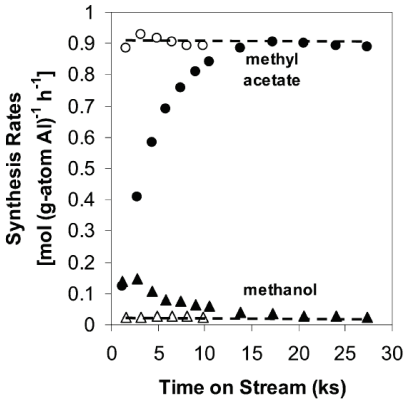

Methyl acetate (●,○) and methanol (▲,△) synthesis rates without DME pretreatment (solid symbols) and with DME pretreatment ($DME_{dosed}/Al = 1$, 7.2 ks He purge, 438 K, open symbols) [HMOR_9.8, 930 kPa CO, 20 kPa DME, 438 K].

Figure 2. MA and MeOH synthesis on H-MOR [31].

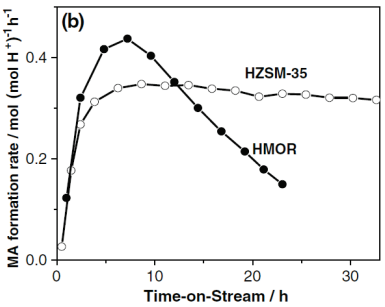

MA synthesis rates over the HZSM-35 and HMOR catalysts. Reaction conditions: 473 K, 1 MPa, $DME/CO/N_2/He/ = 5/50/2.5/42.5$ vol%, 12.5 ml/min

Figure 3. MA formation on H-MOR and H-ZSM-35 [24].

The synthesis of MA at the steady-state proceeds according to the reactions [29, 31]:

$$[SiO(CH_3)Al] + CO \rightarrow [SiO(COCH_3)Al] \quad (6)$$

$$[SiO(COCH_3)Al] + CH_3OCH_3 \rightarrow [SiO(CH_3)Al] + CH_3COOCH_3 \quad (7)$$

The surface methyl groups are in equilibrium with DME in gas-phase through the reaction:

$$CH_3OCH_3 + [SiO(CH_3)Al] \rightleftharpoons [SiO(CH_3)Al] + CH_3OCH_3 \quad (8)$$

Equations (6)-(7) show that MA formation occurs under anhydrous conditions after the induction period. The induction period reflects the initially slow replacement of H^+ with methyl groups. The transient studies of the reactions of DME with CO [29, 31] indicate that the reaction of CO with surface methyl, reaction (6) is the rate limiting step in MA formation.

Figure 4 (copied from [29]) shows the dependence of the MA synthesis rate on the partial pressures of water and CO. The reaction is zeroth-order with respect to the partial pressure of DME, suggesting that the active sites are saturated with DME even at the lowest pressures (0.8 kPa). The formation rate of MA is first-order with respect to the partial pressure of CO, indicating that CO is only weakly bound to the surface or reacts directly from the gas-phase.

In the DFT studies of Boronat et al. [36, 37] no stable adsorption sites of CO were found, supporting the proposed reaction mechanism, in which CO reacts directly from the gas-phase.

Figure 4 shows that a small amount of water in the feed (0.5-1.0 kPa) reduces the MA synthesis rate, increasing the rate of MeOH synthesis by a factor of 14. Boronat et al. [36, 37] suggested that the effect of water may be explained by the fact, that the methyl groups react faster with water than with CO. The energy barriers for the reaction of methyl with water in 12-MR and 8-MR were 0.5 eV lower than for the reactions with CO. However, these values were obtained only at the pure DFT level (without dispersion forces). If the dispersion forces were included (DFT-D) to calculate the Van der Waals forces, the values of the energy barriers significantly changed: 1) in 8-MR, the reaction with CO became 0.5 eV more favorable than the reaction with water, 2) in 12-MR, the reaction with water remained 0.5 eV more favorable than the reaction with CO. The large difference between the energies calculated, using the DFT and DFT-D schemes, and the simplicity of cluster approach (only the atoms close to the active site were modeled at a full DFT level and the effect of the rest of the cluster was included via an effective potential), suggest that the accuracy of the results obtained with DFT-D may be insufficient for proper description of the reaction path.

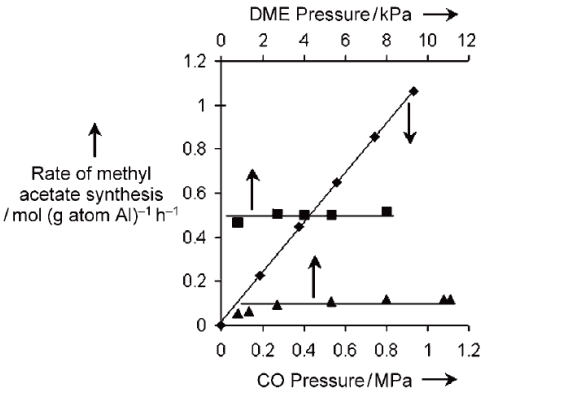

Effects of DME (squares: 0.5 MPa CO, 438 K; triangles: 0.5 kPa H_2O, 0.5 MPa CO, 438 K) and CO (diamonds: 2–16 kPa DME, 438 K) concentration on the rate of methyl acetate formation on H-MOR (Si/Al = 10:1).

Figure 4. Reaction order of MA synthesis with respect to CO and DME partial pressures, for reactions with and without water in the reactant gas [29].

Bhan et al. [30] performed experiments, in which the side pockets of H-MOR were selectively blocked, using Na cations. As a result, the ion-exchanged H-MOR lost its activity for synthesis of MA, showing that 8-MR may be the active sites.

Boronat et al. [36, 37] investigated carbonylation of DME on H-MOR, using DFT methods, and the systems were modeled, using clusters. The study suggested that reaction (6) is the rate limiting step, in agreement with the theoretical studies. Additionally, reaction (7) was shown to be possible only in 12-MR, because the DME molecule is sterically hindered in entering 8-MR. In 8-MR it was proposed that MA is formed in the reaction between surface-acetyl and MeOH:

$$[SiO(COCH_3)Al] + CH_3OH \rightarrow [SiO(H)Al] + CH_3COOCH_3 \quad (9)$$

The discrepancy between this result and the experimental work was explained by noticing that water (and thereby MeOH due to reaction (5)) are always present in the system under reaction conditions. This statement may be inaccurate because in the experimental studies, mentioned here, the inlet gas was let through CaH_2 with the purpose of water removal. However, it must be noted that the formation of coke in H-MOR also yields water.

1.4 Deactivation of Mordenite during DME carbonylation

Mordenite is known to deactivate rapidly (Figure 3), and it is one of the reasons why it is not used industrially as a catalyst for DME carbonylation. In the study of Liu et al. it has been shown that the pretreatment of the catalyst with pyridine significantly improves its resistance towards coking (Figure 5) [38]. Pyridine is able to block the Brønsted acid sites in the main channel, but due to steric constraints it cannot enter the side pockets. Because the synthesis of MA takes place in the side pockets [30], the pretreatment with pyridine only slightly affects the maximum MA formation rate. Pyridine is a bulky molecule and upon its adsorption in the main channels the diffusion limitations for other molecules increase. Thus, the catalyst pretreated with pyridine exhibit a somewhat lower maximum reaction rate [30]. Because blocking the Brønsted acid sites in the main channels improves catalyst stability, Liu et al. concluded that they catalyze the reactions leading to coke formation. Selective dealumination of Mordenite, in which the aluminum atoms in the main channel are removed, has also been demonstrated to enhance the catalyst stability, confirming that the Brønsted acid sites in the main channel are responsible for coking [39].

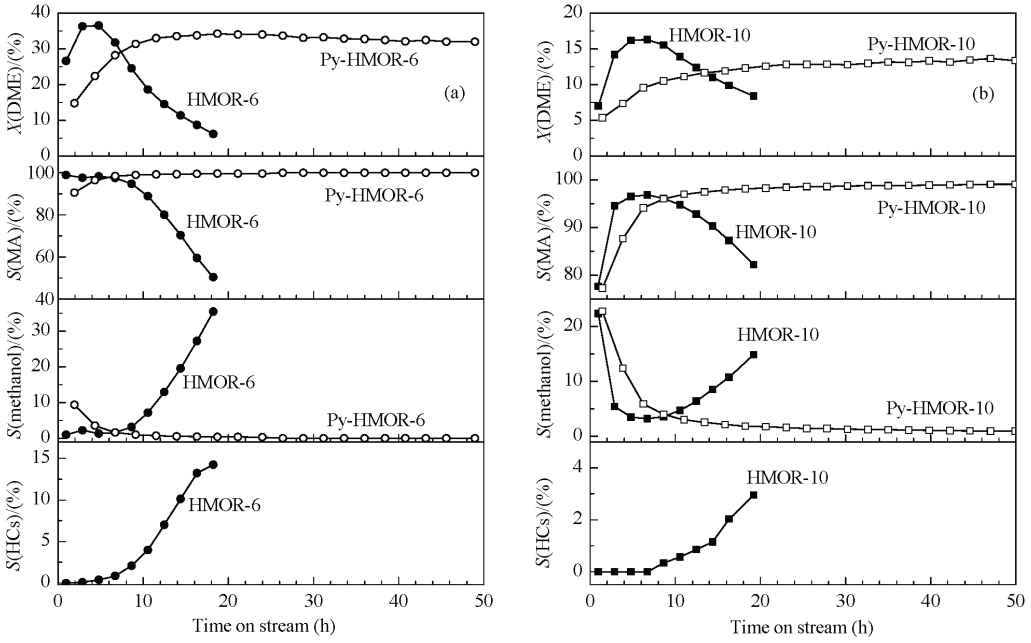

Figure 5. Left: conversion of DME and selectivity for MA, MeOH, and hydrocarbons during DME carbonylation over Mordenite with Si/Al ratio of 6 (HMOR-6) and over the HMOR-6 catalyst pretreated with pyridine (Py-HMOR-6). Right: conversion of DME and selectivity for MA, MeOH, and hydrocarbons during DME carbonylation over Mordenite with Si/Al ratio of 10 (HMOR-10) and over the HMOR-10 catalyst pretreated with pyridine (Py-HMOR-10). Reaction conditions: 473 K, 5% DME, 50% CO, 2.5% N2, 42.5 % He, 1250 Nml/(g·h) [38].

1.5 The scope of this PhD study

In the previous experimental studies of the DME carbonylation on Mordenite, the experiments were performed at pressures up to 10 bar and at differential reaction conditions. It was established that the reaction rate was proportional to the pressure of CO and independent of the DME pressure. Consequently, higher reaction rates and larger conversion degrees of the reactants are expected at higher pressures. In this project, we examine the reaction kinetics at pressures between 10 bar and 100 bar to test whether the pressure dependence of the reaction rate established at low pressures is also valid at high pressures. The reaction conditions, at which high conversion of reactants is achieved, are also important in the industrial context because operating a catalyst at high conversion of reactants reduces the necessary recycle ratio, making the process more economical.

There is a disagreement between the experimental [24, 29-31] and theoretical studies [36, 37] performed so far as regards the reaction mechanism. The previous experimental work strongly suggests that the active sites are in the side-pockets and that the reaction at the steady-state occurs under anhydrous conditions. The theoretical studies showed that surface acetyl in the side pockets

can only react with MeOH, but not with DME. Thus, a small amount of water is necessary in the feed for the MA formation, in disagreement with the assumption of anhydrous experimental conditions. In this study we develop a detailed DFT model for the reaction path for MA synthesis, which is consistent with the experimental data.

Finally, we study the influence of the reaction conditions on the deactivation rate of Mordenite to obtain a better understanding of the reactions leading to coke formation.

2 Methods

2.1 DFT calculations

All DFT [40, 41] calculations in this study were performed, using the grid-based, projector augmented wave, DFT program GPAW [42, 43] and the ASE program package [44]. The Kohn-Sham one-electron valence states [41] were expanded in the basis of real-space grids, with a grid spacing of 0.18 Å. The Brillouin zone of the systems was sampled, using a (1,1,2)-mesh of special **k**-points, of the Monkhorst-Pack [45]. The electronic density was obtained by self-consistent, iterative diagonalization of the Kohn-Sham Hamiltonian with Pulay mixing of the input and output densities. Population of the one-electron Kohn-Sham states was calculated, using an electronic temperature k_bT = 0.1 eV, and the energies were subsequently extrapolated to T = 0 K. The exchange-correlation energy and potential were described within the generalized gradient approximation with BEEF-vdW [46] functional. Structure optimizations were performed using the BFGS algorithm [47-50]. In the calculations of the energy barriers a climbing image nudged elastic band (CINEB) method [51] was used, and the paths were optimized using the fast inertial relaxation engine (FIRE) [52]. The structures and reaction paths were optimized until the residual force component was below 0.03 eV/Å. The convergence was confirmed with respect to the electronic temperature, grid spacing and number of k-points (See appendix 6.3 for details).

The total energies of gas-phase molecules were calculated using the parameters above, unit cells with 10 Å vacuum around the molecule, a (1,1,1)-k point mesh, and k_BT = 0 K.

During the optimization of the unit cell of Mordenite, the grid spacing for the largest unit cells was 0.11 Å. The details of the unit cell optimization of Mordenite are shown in appendix 6.1.

2.2 Experimental work

In the experimental work the Mordenite (SiO_2/Al_2O_3=20) obtained from Zeolyst (CBV21A) was used. The initial ammonium form was converted to the acidic form, H-MOR, by heating it at 773 K (heating rate 1K/min) overnight in a flow of dry air. Before the experiments the catalysts were calcined at 773 K in a flow (200 Nml min^{-1} g^{-1}) of 10 % O_2 in N_2 for 3 h (heating rate 1 K min^{-1}) and cooled down to the reaction temperature.

The DME carbonylation experiments were performed in a high-pressure fixed-bed reactor (Figure 6) [18]. A catalyst bed (0.15 g to 3.00 g, 125-250 μm particle diameter) was placed in a quartz tube

(OD 10 mm, ID 8 mm), inside a stainless steel pressure shell. The pressure shell keeps the pressure outside the quartz tube at the same level as the pressure inside. The reactor temperature is monitored by a K-type thermocouple, located inside the pressure shell. The reported temperature is the average of the temperature along the catalyst bed, and the temperature along the bed is within 1 °C of the average value. The gases (≥ 99.97 % N_2, ≥ 99.999 % CO, ≥ 99.9 % Air, 2 % DME in CO (± 2% analytical uncertainty)) were supplied from pressurized cylinders via Brooks 5850S mass flow controllers. The liquids were added by an HPLC pump (Gilson, Model 305, 5SC pump head).

Product characterization downstream from the reactor has been conducted using a GC-FID/TCD detection system. The oxygenates characterized in the experiment, are methanol, 1-butanol, methyl acetate, acetic acid and dimethyl ether. The characterized hydrocarbons are methane. For gaseous components the areas of the GC peaks have been related to concentrations by calibration against certified gas mixtures (± 2% from AGA A/S). For liquid components (at standard conditions), the calibrations have been made, using gas mixtures prepared by injection of a known volume of the liquid component in a Tedlar bag and allowing the liquid to evaporate. The product characterization relied on online GC analysis. In the experiment in which ketene was observed a mass spectrometer was also used for effluent gas analysis (Hiden Analytical QGA).

The downstream tubing is heat traced to avoid condensation of the reaction products. The gas flow rate is measured downstream from the reactor with a soap film bubble flow meter, operating at ambient temperature and pressure.

The measured flow rate and the measured concentration of component *i,* is used to determine the molar flow rate of component *i*, denoted F_i. The reported CO and DME conversions, X_{CO} and X_{DME}, respectively, were calculated from the molar flow rates into and out of the reactor. For CO:

$$X_{CO} = \frac{F_{CO}^{in} - F_{CO}^{out}}{F_{CO}^{in}} \tag{10}$$

The conversion of DME was calculated in an analogous way.

The product selectivity towards MA is calculated based on the molar content of carbon in the products, as measured by an online GC, according to the formula:

$$S_{MA} = \frac{3 \cdot F_{MA}^{out}}{3 \cdot F_{MA}^{out} + F_{MeOH}^{out} + 2 \cdot F_{AcOH}^{out}}$$

(11)

Because the reaction mixtures in all experiments mainly consist of CO (≥ 98 %), the carbon balance for the reactions is calculated based on the carbon coming from DME. Including CO in the calculation, could potentially result in carbon balances artificially close to 100 %. The carbon balance is calculated, based on the molar content of carbon in DME, MA, MeOH and acetic acid:

$$C_X = \frac{F_{DME}^{out} + F_{MA}^{out} + 0.5 \cdot (F_{MeOH}^{out} + F_{AcOH}^{out})}{F_{DME}^{in}} \cdot 100\%$$

(12)

The temperature programmed oxidation (TPO) experiments were performed in a flow reactor setup, in a flow of 20 % O_2 in N_2, at a heating rate of 10 K/min. 100 mg – 250 mg samples were used. The setup is described in a previous study of Christensen et al. [53].

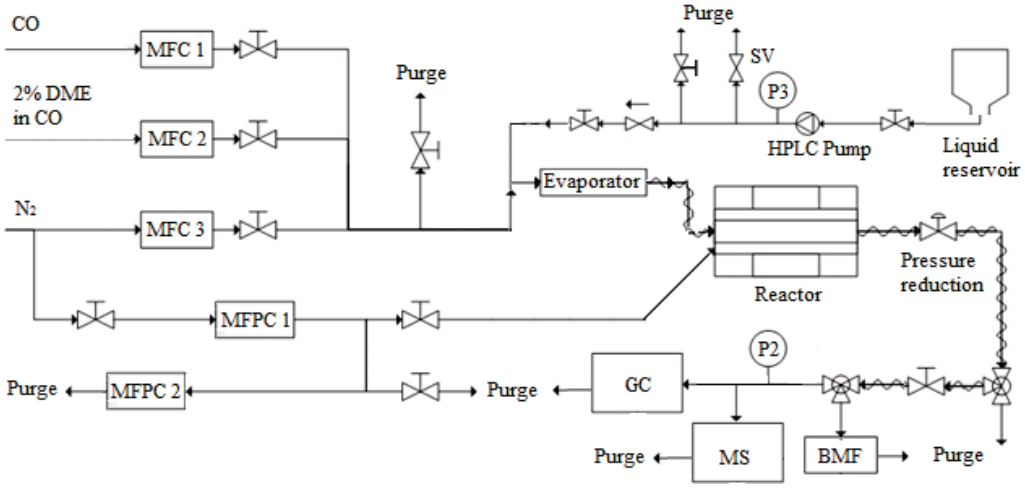

Figure 6. High-pressure fixed-bed reactor.

3 Results

In this section the results obtained in the PhD project are presented. In section 3.1 the reaction mechanism of acetyl formation on Mordenite is investigated in detail. In Section 3.2 a combined DFT and experimental study of the reaction mechanism of MA synthesis on Mordenite is shown. Section 3.3 contains the results of a deactivation study of Mordenite.

3.1 The reaction mechanism of the formation of acetyl on Mordenite

In this study an unprecedented insight into the carbonylation of dimethyl ether over Mordenite was provided through the identification of ketene (CH_2CO) as a reaction intermediate [54] (See SECTION 3.2 for the article). The formation of ketene was predicted by detailed DFT calculations and verified experimentally by the observation of doubly deuterated acetic acid (CH_2DCOOD), when D_2O was introduced in the feed during the carbonylation reaction.

The additional experimental details, which are not included in the article, are shown in Appendix 6.6.1 (Experiment with D_2O) and 6.6.2 (Experiment with H_2O).

3.2 Ketene as a Reaction Intermediate in the Carbonylation of Dimethyl Ether to Methyl Acetate over Mordenite

Angewandte International Edition Chemie

Reaction Mechanisms

International Edition: DOI: 10.1002/anie.201410974
German Edition: DOI: 10.1002/ange.201410974

Ketene as a Reaction Intermediate in the Carbonylation of Dimethyl Ether to Methyl Acetate over Mordenite**

Dominik B. Rasmussen, Jakob M. Christensen, Burcin Temel, Felix Studt, Poul Georg Moses, Jan Rossmeisl, Anders Riisager, and Anker D. Jensen**

In memory of Haldor F. A. Topsøe

Abstract: *Unprecedented insight into the carbonylation of dimethyl ether over Mordenite is provided through the identification of ketene (CH_2CO) as a reaction intermediate. The formation of ketene is predicted by detailed DFT calculations and verified experimentally by the observation of doubly deuterated acetic acid (CH_2DCOOD), when D_2O is introduced in the feed during the carbonylation reaction.*

A number of acidic zeolites are selective catalysts for dimethyl ether (DME) carbonylation, and Mordenite has the highest activity.[1] However, the zeolite catalysts suffer from rapid deactivation because of a build-up of coke and larger carbonaceous species within the zeolite pores.[1c,2] The framework of Mordenite contains two types of cavities: eight-membered ring (8-MR) side pockets and 12-MR main channels. It has been reported that methyl acetate (MA) synthesis takes place within the 8-MR,[3] whereas the 12-MR has been suggested to be responsible for the coke formation which leads to catalyst deactivation.[2a,d] During the initial phase of DME carbonylation, DME reacts with the Brønsted sites, thus forming methyl groups and water [Eqs. (1) and (2)]:

$$CH_3OCH_3 + [SiO(H)Al] \rightleftharpoons [SiO(CH_3)Al] + CH_3OH \quad (1)$$

$$CH_3OH + [SiO(H)Al] \rightleftharpoons [SiO(CH_3)Al] + H_2O \quad (2)$$

These reactions, in which the Brønsted acid sites are methylated, give rise to an induction period. The steady-state phase involves the reaction of CO with the methyl groups, thus forming acetyl species, which in turn react with DME to produce MA and regenerate the methyl groups [Eqs. (3) and (4)]:

$$CO + [SiO(CH_3)Al] \rightarrow [SiO(COCH_3)Al] \quad (3)$$

$$CH_3OCH_3 + [SiO(COCH_3)Al] \rightarrow [SiO(CH_3)Al] + CH_3COOCH_3 \quad (4)$$

Experimental studies showed that formation of the acetyl species is the rate-limiting reaction step, and that the subsequent reaction between DME and acetyl is comparatively fast.[1a,b] Herein, we present unprecedented insights into the formation of acetyl over Mordenite in the steady-state phase, including the DFT energies and energy barriers for all reaction steps, and present experimental verification of the theoretical model by showing that ketene is a reaction intermediate as predicted by the DFT calculations.

We employ the BEEF-vdW functional,[4] which has been shown to quantitatively describe van der Waals interactions of molecules within zeolite pores,[5] as well as reaction kinetics.[6] Formation of the acetyl group was investigated for the 12-MR and 8-MR at the T1-O4 and T3-O3 sites, respectively (see Figure S1 in the Supporting Information, SI).[7] These sites are the preferred adsorption sites for methyl groups, as shown in Table S1 in the SI. The T3-O8 site in the 8-MR was found to be the most favorable adsorption site of methyl groups in previous DFT studies employing cluster models,[8] and for comparison we also investigated the formation of acetyl at this site (see Figures S2 and S3).

The reaction path for formation of acetyl, determined by DFT calculations, begins by the reaction of CO with a surface methyl group which yields an acetyl carbocation [Eq. (5)]:

$$CO + [SiO(CH_3)Al] \rightarrow CH_3CO^+\text{-}[SiOAl]^- \quad (5)$$

Figure 1 shows that the energy barrier for this step is 6 kJ mol^{-1} lower at T3-O3 (8-MR) than at T1-O4 (12-MR),

[*] D. B. Rasmussen, Prof. J. M. Christensen, Prof. A. D. Jensen
Department of Chemical and Biochemical Engineering
Technical University of Denmark
Building 229, 2800 Kgs. Lyngby (Denmark)
E-mail: jmc@kt.dtu.dk
aj@kt.dtu.dk
Dr. B. Temel, Dr. P. G. Moses
Haldor Topsøe Research Laboratories
Nymøllevej 55, 2800 Kgs. Lyngby (Denmark)
Dr. F. Studt
SUNCAT Center for Interface Science and Catalysis
SLAC National Accelerator Laboratory
2575 Sand Hill Road, Menlo Park, CA 94025 (USA)
Prof. J. Rossmeisl
Department of Physics, Technical University of Denmark
Building 307, 2800 Kgs. Lyngby (Denmark)
Prof. A. Riisager
Center for Catalysis and Sustainable Chemistry
Department of Chemistry, Technical University of Denmark
Building 207, 2800 Kgs. Lyngby (Denmark)

[**] This work was financed by the Technical University of Denmark and the Catalysis for Sustainable Energy Initiative (CASE) funded by the Danish Ministry of Science, Technology and Innovation.

Supporting information for this article is available on the WWW under http://dx.doi.org/10.1002/anie.201410974.

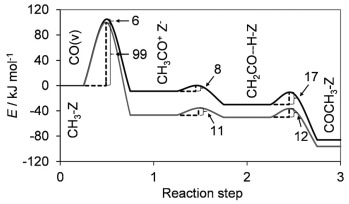

Figure 1. Reaction paths for formation of acetyl from a methyl group and CO within the 12-MR on T1-O4 and the 8-MR on T3-O3. Reaction steps: 0. CO in vacuum, methyl group on the zeolite; 1. acetyl carbocation and negatively charged zeolite; 2. ketene physisorbed onto a Brønsted acid site; 3. acetyl group on zeolite. Black line: reaction steps in the main channel (T1-O4); gray line: reaction steps in the side pocket (T3-O3).

and the optimized geometries of the reaction steps and transition states are shown in Figure 2. Among the sites in the 8-MR the energy barrier for this step is 7 kJ mol^{-1} lower at T3-O8 than at T3-O3, but the methyl group at T3-O8 is, in contrast, 11 kJ mol^{-1} less stable than that at T3-O3. A definite conclusion about the relative importance of these two sites would thus require a full micro-kinetic model. Next, the acetyl carbocation can react to form ketene which is physisorbed on a Brønsted acid site [Eq. (6)]. This reaction occurs with a low barrier (T1-O4: 8 kJ mol^{-1}, T3-O3: 11 kJ mol^{-1}). Alternatively, the acetyl carbocation can react directly to give the acetyl. This reaction involves a simple translational transition state with a very low-energy barrier (T1-O4: 2 kJ mol^{-1}, T3-O3: 1 kJ mol^{-1}, T3-O8: 20 kJ mol^{-1}). Both possibilities involve very low energy barriers, and the carbocation is therefore expected to be short-lived. It thus seems reasonable that the carbocation escaped detection in the NMR study by Corma and co-workers.[9] The ketene on the Brønsted acid site is restructured to acetyl [Eq. (7)]. This reaction also occurs with a low barrier (12-MR: 17 kJ mol^{-1}, 8-MR: 12 kJ mol^{-1}), and the steady-state concentration of ketene is thus also expected to be very low.

$$CH_3CO^+\text{-}[SiOAl]^- \rightarrow CH_2CO\text{-}[SiO(H)Al] \quad (6)$$

$$CH_2CO\text{-}[SiO(H)Al] \rightarrow [SiO(COCH_3)Al] \quad (7)$$

The results of our DFT calculations are summarized in Figure 1 and show that ketene is a potential reaction intermediate in both the 8-MR and the 12-MR. Additionally, we show that formation of acetyl is significantly faster in the 8-MR than in the 12-MR (the 6 kJ mol^{-1} difference in barrier translates into a factor of about 5 on the rates at 438 K) in good agreement with previous experimental and theoretical studies.[3,8b]

To evaluate the prediction of the DFT model wherein ketene is a reaction intermediate, we experimentally investigated whether ketene is present in the system. To detect the ketene experimentally, we introduced D_2O into the CO/DME feed after the MA synthesis had been given 5.7 hours to approach a steady state. The essential part of the experiment is that the gas-phase ketene is the only species in the system which will form doubly deuterated acetic acid upon introduction of deuterated water [Eq. (8)]:

$$C_2H_2O + D_2O \rightarrow CH_2DCOOD \quad (8)$$

It is well established that ketene reacts readily with D_2O in this way already at room temperature.[10] The other possible pathways to acetic acid formation, such as acetyl hydration, MA hydrolysis, and MeOH carbonylation [Eq. (9) to (12)] all result in acetic acid isotopes with, at most, a single deuterium atom.

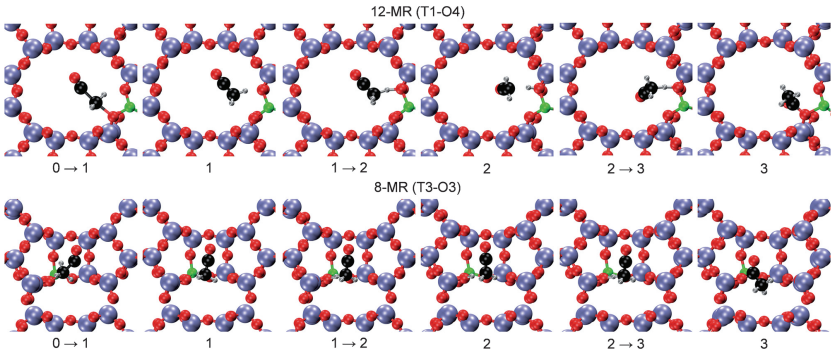

Figure 2. The optimized structures of the reaction intermediates and transition states for the reaction of CO with a methyl group in the 12-MR main channel (top) and in the 8-MR side pocket (bottom). Reaction steps: 0. CO in vacuum, methyl group on the zeolite; 1. acetyl carbocation and negatively charged zeolite; 2. ketene physisorbed onto a Brønsted acid site; 3. acetyl group on zeolite. Arrows indicate transition states. O red, Si blue, H gray, C black, Al green.

$$D_2O + [SiO(COCH_3)Al] \rightarrow CH_3COOD + [SiO(D)Al] \quad (9)$$

$$D_2O + CH_3OCH_3 \rightarrow 2\,CH_3OD \quad (10)$$

$$D_2O + CH_3COOCH_3 \rightarrow CH_3COOD + CH_3OD \quad (11)$$

$$CH_3OD + CO \rightarrow CH_3COOD \quad (12)$$

A distinction between the isomers is possible because previous isotopic studies have shown that the methyl groups are not deprotonated over acidic zeolites by either MeOH, DME, or D_2O, and scrambling of methyl protons does therefore not occur.[1b,11] Consequently, ketene is the only potential source of CH_2DCOOD (molar mass 62 u), while other routes to acetic acid lead to CH_3COOD (molar mass 61 u). We have therefore used mass spectrometry to test if CH_2DCOOD is produced when D_2O is introduced. To avoid that the crossover between adjacent masses in the mass detection leads to an erroneous conclusion, we do not base the analysis on absolute signals, but rather on the $m/z = 62$ to $m/z = 61$ mass ratio.

During the first 5.7 hours of the experiment (Figure 3) the rate of MA synthesis gradually increased, whereas the rate of methanol synthesis concurrently decreased. Then, D_2O was

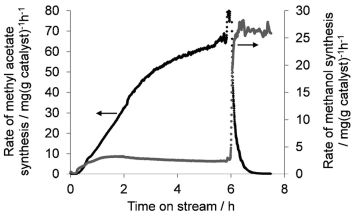

Figure 3. The rate of methyl acetate and methanol formation on H-MOR. Conditions: 9.8 bar CO, 0.2 bar DME, 300 Nml min^{-1}, 3.0 g catalyst, 438 K.

introduced into the CO/DME feed, at a constant flow of 0.01 mL min^{-1}, which corresponds to 4 mol% of the total reactant flow. Upon the introduction of deuterated water the carbonylation reaction was terminated by removal of the methyl groups as CH_3OD [Eq. (2) in the reverse direction], and the MA production stopped. Figure 4 shows the mass ratio between $m/z = 62$ (CH_2DCOOD) and $m/z = 61$ (CH_3COOD) as a function of time on stream during the experiment (the raw $m/z = 62$ and $m/z = 61$ signals are shown in Figure S4).

Before the addition of D_2O into the system, the ratio between the signals from doubly and singly deuterated acetic acid isotopes was a noise signal, but as D_2O was introduced, a well-defined peak emerged (the result of a control experiment with H_2O is shown in the SI). The peak in the mass ratio can be rationalized in terms of our theoretical model. Ketene is an intermediate in the carbonylation of DME to MA. Immediately upon the introduction of D_2O the carbonylation

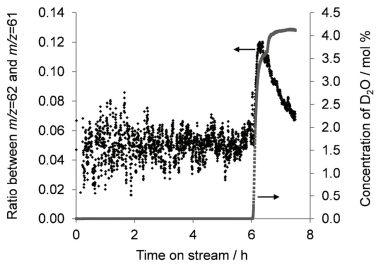

Figure 4. The ratio between the MS signal at $m/z = 62$ (doubly deuterated acetic acid) and $m/z = 61$ (singly deuterated acetic acid). Reaction conditions: 9.8 bar CO, 0.2 bar DME, 300 Nml min^{-1}, 3.0 g catalyst, 438 K.

reaction was still running, and ketene intermediates were available for conversion into CH_2DCOOD [Eq. (8)], whereby the $m/z = 62$ signal became more prominent. However, as shown in Figure 3, deuterated water also suppressed the carbonylation reaction by removing the essential methyl groups on the zeolite [Eq. (2) in the reverse direction], and when the carbonylation reaction thus stopped, and no more ketene intermediate was formed, the $m/z = 62$ signal from CH_2DCOOD dropped towards the noise level.

In conclusion, we have presented a theoretical DFT model of unprecedented detail for the carbonylation of DME over Mordenite zeolites. The theoretical model predicts the involvement of a ketene intermediate, which was not previously known to be involved in the reaction. We have experimentally identified ketene, which verifies our theoretical model. However, in addition to substantiating the DFT model, the observation of the highly reactive ketene molecule is also important because of its potential implications for zeolite catalysis. As an example, ketene undergoes base-catalyzed polymerization into polyketones at very low temperatures.[12] Ketene could therefore be of importance for the build-up of coke and larger carbonaceous structures which deactivate the catalyst in the carbonylation reaction. The observation of ketene is potentially also important for the ongoing fundamental studies of the formation of the initial C–C bonds using acidic zeolite catalysts for hydrocarbon synthesis.[13]

Experimental Section

All DFT calculations in this study were performed using the grid-based, projector augmented wave, DFT program GPAW and the ASE program package.[14] A grid spacing of less than 0.18 Å was used and the reciprocal space was sampled by a (1,1,2)-mesh of Monkhorst-Pack k-points. The exchange-correlation energy and potential were calculated within the generalized gradient approximation with the BEEF-vdW functional.[4] The transition states were found with the climbing-image NEB method and confirmed by frequency analysis using a displacement of 0.02 Å (see Table S2).[15] The structures and reaction paths were optimized until the residual force, acting on the atoms, was below 0.03 eV Å^{-1}.

Mordenite ($SiO_2/Al_2O_3 = 20$) was obtained from Zeolyst (CBV21A). The initial ammonium form was converted to the protonated form by heating it at 773 K for 3 h (heating rate 1 K min^{-1}) in a flow of dry air (300 Nml min^{-1}). Before the experiment, the catalyst (3.00 g, 125–250 μm) was calcined in the reactor at 773 K in a flow (300 Nml min^{-1}) of 10 % O_2 in N_2 for 3 h (heating rate 1 K min^{-1}) and cooled to the reaction temperature. The experiment was conducted in a high-pressure fixed-bed reactor,[16] in which the catalyst was loaded in a quartz tube (OD 10 mm, ID 8 mm). The carbonylation reaction was performed using 2 % DME in CO (AGA) at a flow of 300 Nml min^{-1}, 438 K and 10 bar. Deuterated water (Sigma–Aldrich, 99.9 atom % D), was added by an HPLC pump (Gilson, Model 305, 5SC pump head). The reactor effluent was transferred by heated lines to a mass spectrometer (Hiden Analytical QGA) and to a gas chromatograph (Agilent Technologies, model 6890N) equipped with a DB1 column connected to flame-ionization detector and a Porapak N column, followed by a 13x Molesieve column, connected to a thermal conductivity detector.

Keywords: carbonylation · density functional calculations · heterogeneous catalysis · reaction mechanisms · zeolites

How to cite: *Angew. Chem. Int. Ed.* **2015**, *54*, 7261–7264
Angew. Chem. **2015**, *127*, 7369–7372

[1] a) P. Cheung, A. Bhan, G. J. Sunley, E. Iglesia, *Angew. Chem. Int. Ed.* **2006**, *45*, 1617–1620; *Angew. Chem.* **2006**, *118*, 1647–1650; b) P. Cheung, A. Bhan, G. J. Sunley, D. J. Law, E. Iglesia, *J. Catal.* **2007**, *245*, 110–123; c) J. Liu, H. Xue, X. Huang, Y. Li, W. Shen, *Catal. Lett.* **2010**, *139*, 33–37.

[2] a) J. L. Liu, H. F. Xue, X. M. Huang, P. H. Wu, S. J. Huang, S. B. Liu, W. J. Shen, *Chin. J. Catal.* **2010**, *31*, 729–738; b) H. F. Xue, X. M. Huang, E. Ditzel, E. S. Zhan, M. Ma, W. J. Shen, *Ind. Eng. Chem. Res.* **2013**, *52*, 11510–11515; c) H. F. Xue, X. M. Huang, E. Ditzel, E. S. Zhan, M. Ma, W. J. Shen, *Chin. J. Catal.* **2013**, *34*, 1496–1503; d) H. F. Xue, X. M. Huang, E. S. Zhan, M. Ma, W. J. Shen, *Catal. Commun.* **2013**, *37*, 75–79.

[3] A. Bhan, A. D. Allian, G. J. Sunley, D. J. Law, E. Iglesia, *J. Am. Chem. Soc.* **2007**, *129*, 4919–4924.

[4] J. Wellendorff, K. T. Lundgaard, A. Møgelhøj, V. Petzold, D. D. Landis, J. K. Nørskov, T. Bligaard, K. W. Jacobsen, *Phys. Rev. B* **2012**, *85*, 235149.

[5] R. Y. Brogaard, P. G. Moses, J. K. Norskov, *Catal. Lett.* **2012**, *142*, 1057–1060.

[6] R. Y. Brogaard, R. Henry, Y. Schuurman, A. J. Medford, P. G. Moses, P. Beato, S. Svelle, J. K. Norskov, U. Olsbye, *J. Catal.* **2014**, *314*, 159–169.

[7] C. Baerlocher, L. B. McCusker, Database of Zeolite Structures: http://www.iza-structure.org/databases/.

[8] a) M. Boronat, C. Martinez-Sanchez, D. Law, A. Corma, *J. Am. Chem. Soc.* **2008**, *130*, 16316–16323; b) M. Boronat, C. Martinez, A. Corma, *Phys. Chem. Chem. Phys.* **2011**, *13*, 2603–2612.

[9] I. Lezcano-González, J. A. Vidal-Moya, M. Boronat, T. Blasco, A. Corma, *Angew. Chem. Int. Ed.* **2013**, *52*, 5138–5141; *Angew. Chem.* **2013**, *125*, 5242–5245.

[10] a) W. Caminati, F. Scappini, G. Corbelli, *J. Mol. Spectrosc.* **1979**, *75*, 327–332; b) T. F. Kahan, T. K. Ormond, G. B. Ellison, V. Vaida, *Chem. Phys. Lett.* **2013**, *565*, 1–4.

[11] a) D. M. Marcus, K. A. McLachlan, M. A. Wildman, J. O. Ehresmann, P. W. Kletnieks, J. F. Haw, *Angew. Chem. Int. Ed.* **2006**, *45*, 3133–3136; *Angew. Chem.* **2006**, *118*, 3205–3208; b) Z. M. Cui, Q. Liu, S. W. Baint, Z. Ma, W. G. Song, *J. Phys. Chem. C* **2008**, *112*, 2685–2688.

[12] a) G. Natta, G. Mazzanti, G. Pregaglia, M. Binaghi, M. Peraldo, *J. Am. Chem. Soc.* **1960**, *82*, 4742–4743; b) P. Zarras, O. Vogl, *Prog. Polym. Sci.* **1991**, *16*, 173–201; c) H. Egret, J. P. Couvercelle, J. Belleney, C. Bunel, *Eur. Polym. J.* **2002**, *38*, 1953–1961.

[13] a) J. E. Jackson, F. M. Bertsch, *J. Am. Chem. Soc.* **1990**, *112*, 9085–9092; b) J. F. Haw, W. G. Song, D. M. Marcus, J. B. Nicholas, *Acc. Chem. Res.* **2003**, *36*, 317–326; c) D. Lesthaeghe, V. Van Speybroeck, G. B. Marin, M. Waroquier, *Ind. Eng. Chem. Res.* **2007**, *46*, 8832–8838; d) U. Olsbye, S. Svelle, M. Bjorgen, P. Beato, T. V. W. Janssens, F. Joensen, S. Bordiga, K. P. Lillerud, *Angew. Chem. Int. Ed.* **2012**, *51*, 5810–5831; *Angew. Chem.* **2012**, *124*, 5910–5933.

[14] a) S. R. Bahn, K. W. Jacobsen, *Comput. Sci. Eng.* **2002**, *4*, 56; b) J. J. Mortensen, L. B. Hansen, K. W. Jacobsen, *Phys. Rev. B* **2005**, *71*, 035109; c) J. Enkovaara, C. Rostgaard, J. J. Mortensen, J. Chen, M. Dulak, L. Ferrighi, J. Gavnholt, C. Glinsvad, V. Haikola, H. A. Hansen, H. H. Kristoffersen, M. Kuisma, A. H. Larsen, L. Lehtovaara, M. Ljungberg, O. Lopez-Acevedo, P. G. Moses, J. Ojanen, T. Olsen, V. Petzold, N. A. Romero, J. Stausholm-Moller, M. Strange, G. A. Tritsaris, M. Vanin, M. Walter, B. Hammer, H. Hakkinen, G. K. H. Madsen, R. M. Nieminen, J. K. Norskov, M. Puska, T. T. Rantala, J. Schiotz, K. S. Thygesen, K. W. Jacobsen, *J. Phys. Condens. Matter* **2010**, *22*, 253202.

[15] G. Henkelman, B. P. Uberuaga, H. Jonsson, *J. Chem. Phys.* **2000**, *113*, 9901–9904.

[16] J. M. Christensen, P. M. Mortensen, R. Trane, P. A. Jensen, A. D. Jensen, *Appl. Catal. A* **2009**, *366*, 29–43.

Received: November 12, 2014
Revised: April 13, 2015
Published online: May 12, 2015

Additional DFT results

Table S1. Stability of the methyl groups in the main channel on the T1 site and in the side pocket on the T3 site, relatively to the most stable methyl group on the same site.

Position	E / kJ mol^{-1}	Position	E / kJ mol^{-1}
T1-O1	12	T3-O3	0
T1-O4	0	T3-O8	11
		T3-O9	32

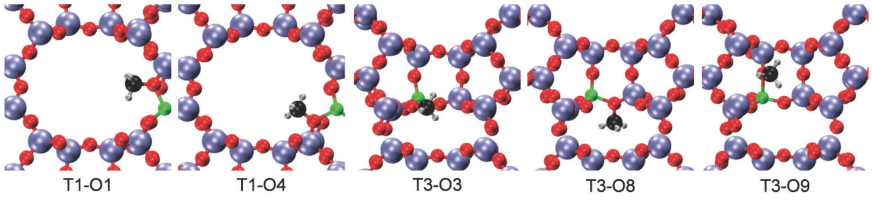

Figure S1. The optimized structures of the methyl groups in the main channel on the T1 site and in the side pocket on the T3 site. O red, Si blue, H gray, C black, Al green.

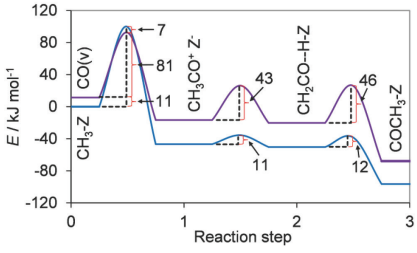

Figure S2. Reaction paths for formation of acetyl from methyl and CO within the 8-MR on the T3-O3 and T3-O8 sites. Reaction steps: 0 CO in vacuum, methyl group on the zeolite; 1 Acetyl carbocation and negatively charged zeolite; 2 Ketene physisorbed on a Brønsted acid site; 3 Acetyl group on zeolite. Blue line: reaction steps on the T3-O3 site; Purple line: reaction steps on the T3-O8 site.

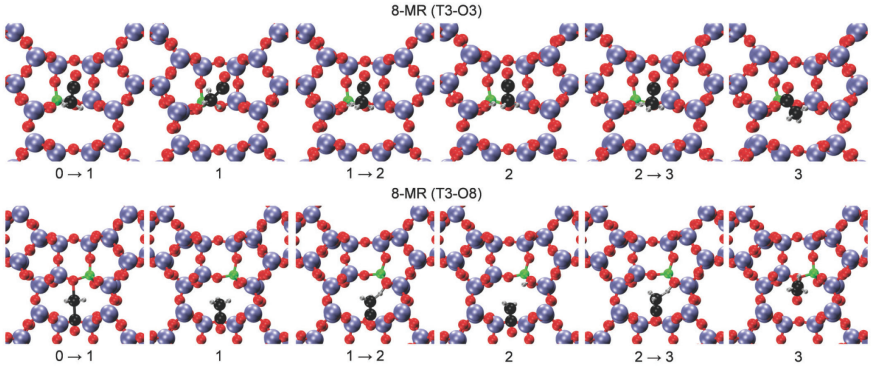

Figure S3. The optimized structures of the reaction intermediates and transition states for the reaction of CO with a methyl group in the side pocket on the T3-O3 and T3-O8 sites. Reaction steps: 0 CO in vacuum, methyl group on the zeolite; 1 Acetyl carbocation and negatively charged zeolite; 2 Ketene physisorbed on a Brønsted acid site; 3 Acetyl group on zeolite. Arrows indicate transition states. O red, Si blue, H gray, C black, Al green.

Table S2. The calculated frequencies of the transitions states for the reaction of CO with a methyl group on the T1-O4, T3-O3 and T3-O8 sites. Only the vibrations of the guest molecules are calculated. Reaction steps: 0 CO in vacuum, methyl group on the zeolite; 1 Acetyl carbocation and negatively charged zeolite; 2 Ketene physisorbed on a Brønsted acid site; 3 Acetyl group on zeolite. Arrows indicate transition states.

Reaction step		T1-O4 cm^{-1}	T3-O3 cm^{-1}	T3-O8 cm^{-1}
	CO(v)	2157		
0	CH3-Z	20, 107, 253, 654, 1137, 1155, 1451, 1466, 1491, 3030, 3115, 3158	60, 155, 283, 647, 1129, 1156, 1449, 1475, 1486, 3041, 3132, 3158	81i, 105, 266, 646, 1121, 1149, 1441, 1469, 1484, 3052, 3148, 3180
0 → 1		476i, 36i, 119, 165, 167, 191, 214, 326, 358, 1066, 1096, 1206, 1365, 1388, 2191, 3025, 3222, 3277	490i, 43, 93, 105, 117, 140, 214, 345, 351, 1089, 1129, 1210, 1369, 1387, 2174, 3065, 3248, 3290	446i, 55, 116, 161, 163, 198, 205, 335, 361, 1086, 1092, 1193, 1365, 1392, 2196, 3105, 3301, 3310
1		68i, 124, 125, 137, 195, 317, 423, 481, 951, 994, 1007, 1311, 1335, 1354, 2070, 2286, 2998, 3055	82, 126, 175, 187, 210, 339, 423, 463, 970, 1002, 1020, 1347, 1358, 1378, 2240, 2602, 2801, 3038	88i, 55i, 96, 122, 166, 175, 395, 421, 926, 977, 997, 1307, 1341, 1359, 2273, 2975, 3039, 3078
1 → 2		602i, 49i, 31, 95, 135, 346, 387, 458, 564, 925, 1020, 1075, 1265, 1350, 1451, 2230, 3032, 3094	730i, 56, 170, 194, 201, 362, 409, 492, 555, 883, 1039, 1057, 1256, 1368, 1400, 2218, 3032, 3110	1136i, 24i, 32, 133, 227, 291, 389, 492, 572, 914, 1037, 1099, 1226, 1355, 1482, 2212, 3020, 3100
2		54, 110, 136, 161, 207, 396, 433, 553, 619, 779, 989, 1134, 1224, 1371, 2172, 2916, 3102, 3193	51i, 21, 79, 130, 185, 371, 421, 543, 631, 824, 996, 1130, 1249, 1374, 2161, 2732, 3115, 3206	90i, 64, 85, 99, 156, 188, 344, 430, 504, 596, 967, 1051, 1150, 1375, 2157, 3170, 3265, 3638
2 → 3		512i, 103i, 91, 116, 132, 378, 395, 511, 561, 905, 1043, 1047, 1277, 1363, 1423, 2236, 3036, 3111	707i, 33, 108, 148, 149, 362, 397, 492, 554, 887, 1040, 1055, 1258, 1361, 1406, 2218, 3036, 3111	911i, 27i, 64, 190, 227, 336, 388, 507, 559, 869, 1019, 1104, 1247, 1366, 1446, 2210, 3030, 3131
3		52i, 42, 116, 142, 280, 377, 537, 589, 963, 1038, 1097, 1386, 1435, 1460, 1880, 3008, 3094, 3142	42i, 101, 165, 186, 281, 348, 536, 575, 962, 1048, 1095, 1381, 1443, 1459, 1881, 3032, 3103, 3150	51i, 95, 138, 214, 269, 359, 535, 548, 961, 1033, 1063, 1381, 1441, 1451, 1904, 3053, 3124, 3167

Additional experimental results

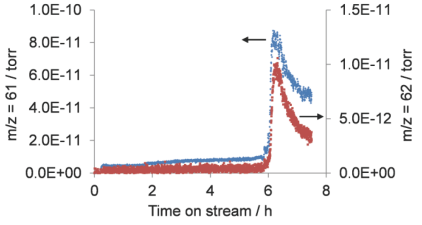

Figure S4. The MS signal at *m/z*=62 (doubly deuterated acetic acid) and m/z=61 (singly deuterated acetic acid). Conditions: 9.8 bar CO, 0.2 bar DME, 300 Nml/min, 3.0 g catalyst, 438 K.

To confirm that the peak in the mass ratio in Figure 4 in the main article was not an artifact of the experimental procedure, the experiment has also been performed using ordinary distilled water (H_2O). The signals corresponding to acetic acid (m/z = 60), singly deuterated acetic acid (m/z = 61) and doubly deuterated acetic acid (m/z = 62) were measured.

During the first 2.7 h of the experiment (Figure S5) the rate of MA synthesis increased, while the rate of MeOH synthesis concurrently decreased. Then, H_2O was introduced into the CO/DME feed, at a constant rate of 0.01 ml/min, corresponding to 4 mol % of the total reactant flow. Just as in the experiment with D_2O, this terminated the carbonylation reaction due to the removal of the methyl groups as MeOH, and the MA formation stopped.

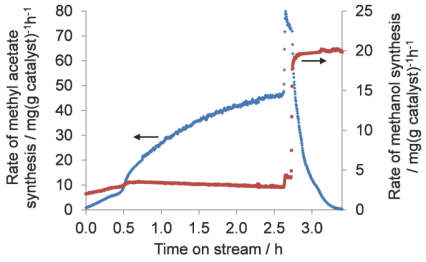

Figure S5. The rate of methyl acetate and methanol formation on H-MOR. Conditions: 9.8 bar CO, 0.2 bar DME, 300 Nml/min, 3.0 g catalyst, 438 K.

Before the addition of H_2O into the system, the ratio between m/z = 61 (CH_3COOD) and m/z = 60 (CH_3COOH) was a noise signal (Figure S6), but as H_2O was introduced, first the ratio very briefly increased (< 8 min) and then dropped to a lower level. The increase of the signal ratio was a short-lived artifact, caused by the small flow change in the system upon the introduction of water into the feed stream. When the flow stabilized, the signal ratio dropped to a lower level because of the increased concentration of acetic acid in the system, which was formed in the reaction between water and surface acetyl (13):

$$H_2O + [SiO(COCH_3)Al] \rightarrow CH_3COOH + [SiO(H)Al] \quad (13)$$

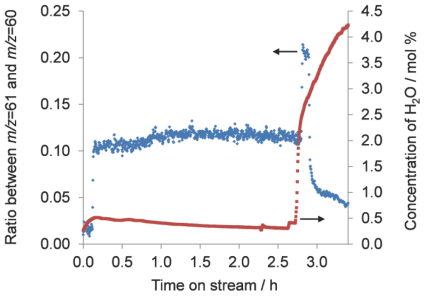

Figure S6. The ratio between the MS signal at *m/z*=61 (singly deuterated acetic acid) and m/z=60 (acetic acid). Conditions: 9.8 bar CO, 0.2 bar DME, 300 Nml/min, 3.0 g catalyst, 438 K.

The ratio between m/z = 62 (CH_2DCOOD) and m/z = 61 (CH_3COOD) was, as expected, a noise signal during the entire experiment (Figure S7), and the brief fluctuation of the signal upon water introduction was caused by a flow fluctuation in the system, as already discussed.

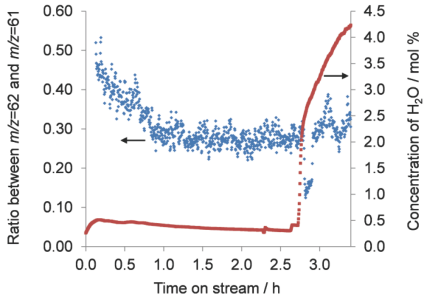

Figure S7. The ratio between the MS signal at *m/z*=62 (doubly deuterated acetic acid) and m/z=61 (singly deuterated acetic acid). Conditions: 9.8 bar CO, 0.2 bar DME, 300 Nml/min, 3.0 g catalyst, 438 K.

Contrary to the experiment with H_2O, in which short-lived (< 8 min) signal fluctuations arose due to flow changes in the system, the peak in the ratio between m/z = 62 (CH_2DCOOD) and m/z = 61 (CH_3COOD) shown in Figure 4 in the main article, was measured for over 1.5 h, showing that ketene is an intermediate in the carbonylation of DME to MA.

3.3 A combined DFT and experimental study of the reaction mechanism of dimethyl ether carbonylation to methyl acetate on Mordenite

Here the reaction mechanism of dimethyl ether carbonylation to methyl acetate on Mordenite was studied with periodic density functional theory calculations including dispersion forces and experimentally at pressures between 10 bar and 100 bar (See section 3.4 for the article manuscript). The theoretical study showed that the reaction of CO with the surface methyl groups, the rate-limiting step, is faster in the side pockets than in the main channel. Additionally, in contrast to the previous DFT studies of this reaction, the reaction of dimethyl ether with surface acetyl was demonstrated to occur with low energy barriers in the side pockets and in the main channel. The experimental study of the reaction kinetics showed that methyl acetate inhibits the reaction rate by forming inactive complexes with surface methyl groups.

3.4 Reaction Mechanism of Dimethyl Ether Carbonylation to Methyl Acetate on Mordenite – A Combined DFT/Experimental Study

Reaction Mechanism of Dimethyl Ether Carbonylation to Methyl Acetate on Mordenite – A Combined DFT/Experimental Study

Dominik B. Rasmussen[1], Jakob M. Christensen[1,*], Burcin Temel[2], Felix Studt[3], Poul Georg Moses[2], Jan Rossmeisl[4], Anders Riisager[5], Anker D. Jensen[1,*]

[1] Department of Chemical and Biochemical Engineering, Technical University of Denmark, Building 229, 2800 Kgs. Lyngby, Denmark

[2] Haldor Topsøe A/S, Nymøllevej 55, DK-2800 Kgs. Lyngby, Denmark

[3] SUNCAT Center for Interface Science and Catalysis, SLAC National Accelerator Laboratory, 2575 Sand Hill Road, Menlo Park, CA 94025, USA

[4] Department of Physics, Technical University of Denmark, Building 307, 2800 Kgs. Lyngby, Denmark

[5] Center for Catalysis and Sustainable Chemistry, Department of Chemistry, Technical University of Denmark, Building 207, 2800 Kgs. Lyngby, Denmark

[*] Corresponding authors: jmc@kt.dtu.dk (Jakob M. Christensen), aj@kt.dtu.dk (Anker D. Jensen)

Abstract

The reaction mechanism of dimethyl ether carbonylation to methyl acetate on Mordenite was studied theoretically with periodic density functional theory calculations including dispersion forces and experimentally in a fixed bed flow reactor at pressures between 10 bar and 100 bar. The theoretical study showed that the reaction of CO with surface methyl groups, the rate-limiting step, is faster in the side pockets than in the main channel; the reaction of dimethyl ether with surface acetyl to methyl acetate was demonstrated to occur with low energy barriers in the side pockets and in the main channel. The experimental study of the reaction kinetics showed that methyl acetate inhibits the reaction rate by forming inactive complexes with surface methyl groups.

1 Introduction

The global economy and modern society are heavily dependent on stable oil prices and supply. Currently, most transportation fuel is of fossil origin and its continuous use is thus not sustainable. The steadily increasing prices of fossil fuels and the vulnerability of the global economy to disruption of oil supplies are other factors, which make it evident that the demand for alternative fuels will continue to increase. Ethanol (EtOH) can play an important role in this context as a gasoline additive or substitute [1-3]. Catalytic conversion of syngas to EtOH is an attractive option due to its flexibility with respect to feedstock and potentially high energy efficiency. A number of catalysts for direct conversion of syngas to EtOH have been developed, but their activity and selectivity towards EtOH are relatively low [3-14]. Recently, an alternative, two-stage method was demonstrated wherein dimethyl ether (DME), which can be formed efficiently and selectively from syngas via methanol, reacts with CO to form methyl acetate (MA) [15-17]. MA is then in a subsequent step hydrogenated to EtOH and methanol (MeOH). The main advantage of this indirect process is its unprecedented

selectivity towards EtOH, while MeOH, the main by-product, and the unreacted syngas are easily recycled. The challenge that needs to be solved before this process can find industrial application is to increase the activity and stability of the catalyst for MA synthesis [18]. The subsequent hydrogenation of MA to MeOH and EtOH is facile. A number of acidic zeolites are selective catalysts for DME carbonylation and Mordenite has the highest activity [19-21]. However, the zeolite catalysts suffer from rapid deactivation due to build-up of coke and large carbonaceous species within the zeolite pores [21-25]. The framework of Mordenite contains two types of cavities: eight-membered ring (8-MR) side pockets and 12-MR main channels. It has been reported that MA synthesis takes place in the 8-MR [26], whereas the 12-MR have been suggested to be responsible for the coke formation that leads to catalyst deactivation [22, 25]. During the initial phase of DME carbonylation, DME reacts with the Brønsted sites, forming methyl groups and water [Eqs. (1) and (2)]:

$$CH_3OCH_3 + [SiO(H)Al] \rightleftharpoons [SiO(CH_3)Al] + CH_3OH \quad (1)$$

$$CH_3OH + [SiO(H)Al] \rightleftharpoons [SiO(CH_3)Al] + H_2O \quad (2)$$

These reactions, in which the Brønsted acid sites are methylated, give rise to an induction period. The steady-state phase involves the reaction of CO with the methyl groups, forming acetyl species, which in turn react with DME, to produce MA and regenerate the methyl groups [Eqs. (3) and (4)]:

$$CO + [SiO(CH_3)Al] \rightarrow [SiO(CH_3CO)Al] \quad (3)$$

$$CH_3OCH_3 + [SiO(CH_3CO)Al] \rightarrow [SiO(CH_3)Al] + CH_3COOCH_3 \quad (4)$$

The previous experimental studies showed that formation of the acetyl species is the rate-limiting reaction step; the subsequent reaction between DME and acetyl is comparatively fast [19, 20]. Also, the reaction kinetics were studied at differential conditions for pressures up to 12 bar, and the reaction rate was shown to be independent of the DME pressure and

proportional to the CO pressure [19, 20]. The previous theoretical studies employing cluster models showed that the reaction of CO with methyl groups is faster in the side pockets than in the main channel [27, 28], in good agreement with the experimental results; however, it remains to be demonstrated that the reaction of DME with acetyl in the side pockets is faster than the reaction of CO with methyl.

In this study we investigate the induction and the steady-state phase of DME carbonylation on Mordenite in the main channel and in the side pockets, using periodic DFT calculations including the dispersion forces. Additionally, we study the reaction kinetics at high pressures, between 10 bar and 100 bar. The results of the kinetic studies are used to develop a kinetic model.

2 Methods

2.1 DFT calculations

All DFT calculations in this study were performed, using the grid-based, projector augmented wave, DFT program GPAW [29, 30] and the ASE program package [31]. Periodic boundary conditions were used for all systems except the molecules in vacuum. A grid spacing of less than 0.18 Å was used for all calculations unless otherwise stated. The reciprocal space was sampled by a (1,1,2)-mesh of Monkhorst-Pack k-points [32]. The convergence criteria for the integral of the absolute density change and the integral of the square of the residuals of the Kohn-Sham equations in the self-consistent field were $1.0 \cdot 10^{-5}$ electrons and $1.0 \cdot 10^{-9}$ eV^2/electron, respectively. The exchange-correlation energy and potential were calculated within the generalized gradient approximation with the BEEF-vdW functional [33]. The electronic temperatures of 0.1 eV and 0.0 eV were used for the periodic and non-periodic calculations, respectively.

The unit cell parameters of silicate Mordenite were calculated by energy minimization of the optimized structures with respect to the unit cell parameters. These calculations employed a grid spacing of 0.10 Å. The calculated unit cell parameters (a = 18.323 Å, b = 20.795 Å, c = 7.626 Å) compare very well with the experimental values (a = 18.094 Å, b = 20.516 Å, c = 7.542Å) [34]. The framework of Mordenite contains 2 types of cavities: 1) eight-membered ring (8-MR) side pockets, parallel to the b axis and 2) 12-MR main channels, parallel to the a axis. There are 4 nonequivalent tetrahedral sites in the unit cell of Mordenite: (1) T1 in the 12-MR, T2 and T4 at the intersection between the 12-MR and 8-MR and T3 in the 8-MR. The acidic form of Mordenite was created, by replacing a single Si atom in the silicate unit cell with Al. The unit cell parameters of silicate Mordenite were used in all calculations.

The calculations involving molecules in vacuum employed supercells with a vacuum layer of 5.0 Å around the molecule. All systems were optimized using the Broyden-Fletcher-Goldfarb-Shanno (BFGS) algorithm [35-38]. The localization of the transition states and the calculation of the energy barriers were performed using the climbing-image nudged elastic band method [39]. The minimum energy paths were relaxed using the fast inertial relaxation engine (FIRE) [40] and the saddle points were verified by vibrational frequency analysis. The structures and reaction paths were optimized until the residual force, acting on the atoms, was below 0.03 eV/Å.

2.2 Experimental details

Mordenite (SiO_2/Al_2O_3 = 20) was obtained from Zeolyst (CBV21A) and all Al sites were used for calculation of the turnover frequencies. The initial ammonium form was converted to the acidic form by heating it at 773 K for 3 h (heating rate 1 K min^{-1}) in a flow of dry air. Before the experiments the catalyst (0.15-1.50 g, 125-250 μm) was calcined in the reactor at 773 K in a flow (200 Nml min^{-1} g^{-1}) of 10 % O_2 in N_2 for 3 h (heating rate 1 K min^{-1}) and

cooled to the reaction temperature. The experiments were conducted in a high-pressure fixed-bed reactor in which the catalyst was loaded in a quartz tube (OD 10 mm, ID 8 mm) inside a pressure shell [12]. The carbonylation reactions were performed using 2% DME in CO (AGA) at a flow of 300 Nml min^{-1}, 438 K. The reactor effluent was transferred by heated lines to a mass spectrometer (Hiden Analytical QGA) and to a gas chromatograph (Agilent Technologies, model 6890N) equipped with a DB1 column connected to flame-ionization detector and a Porapak N column, followed by a 13x Molesieve column, connected to a thermal conductivity detector.

3 Results and Discussion

3.1 DFT study of the reaction path

Table 1 shows the stability of the protons and methyl groups on the T1 and T3 sites, and the optimized structures of the methyl groups are shown in Figure 1. The protons are almost equally stable on T1, T1-O4 being only 0.03 eV more energetically favorable than T1-O1. On T3, T3-O3 is clearly the preferred adsorption site, more stable than T3-O8 (0.19 eV) and T3-O9 (0.17 eV). A similar trend in adsorption strength is observed for methyl groups: T1-O4 and T3-O3 are the favored adsorption sites, at least 0.12 eV more stable than the other sites.

Table 1. Stability of the protons and methyl groups in the main channel on the T1 site and in the side pocket on the T3 site. The energies are relative to the most stable proton or methyl group on the same site.

H-Z				CH_3-Z			
Position	E (eV)	Position	E (eV)	Position	E (eV)	Position	E (eV)
T1-O1	0.03	T3-O3	0.00	T1-O1	0.12	T3-O3	0.00
T1-O4	0.00	T3-O8	0.19	T1-O4	0.00	T3-O8	0.12
		T3-O9	0.17			T3-O9	0.49

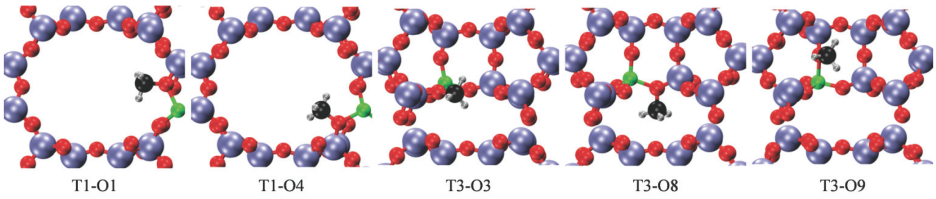

Figure 1. The optimized structures of the methyl groups in the main channel on the T1 site and in the side pocket on the T3 site. O red, Si blue, H gray, C black, Al green.

During the initiation phase of MA synthesis, the Brønsted acid sites react with DME and MeOH, and are, as a result, substituted with methyl groups. Molecules, which adsorb on the Brønsted acid sites more strongly than DME or MeOH, without being decomposed, can potentially inhibit the initiation phase. To investigate this effect, we have calculated the adsorption energies of the molecules typically found in the effluent gas during DME carbonylation, on the Brønsted acid sites on T1-O4 and T3-O3 (Table 2). The adsorption energies of ammonia are also included, as they give a measure of the acidity of the proton. The optimized structures of the adsorbed molecules are shown in Figure 2.

Table 2. Adsorption energies of DME, MeOH, MA, H_2O, AcOH, and NH_3 on a proton in the main channel on the T1-O4 site and in the side pocket on the T3-O3 site. The energies are relative to the Brønsted acid site and the molecule in vacuum.

Species	T1 H-O4 E_{ads} (eV)	T3 H-O3 E_{ads} (eV)
NH_3	-1.37	-1.47
MA	-1.12	-1.01
DME	-0.98	-0.99
MeOH	-0.89	-1.09
AcOH	-1.05	-0.90
H_2O	-0.74	-0.87

Ammonia is, as expected due to its basic nature, the molecule that adsorbs most strongly on the Brønsted acid sites (as an ammonium cation) and it is 0.10 eV more stable on T3-O3 than on T1-O4. This result shows that the proton is more acidic in the side pocket than in the main channel, which is in good agreement with the experimental results [26, 41, 42]. The other

molecules adsorb in geometries, in which the oxygen atom in the molecule forms a hydrogen bond with the acidic proton and the molecule is oriented in a manner that leads to additional, weaker, hydrogen bonds between the hydrogen atoms in the molecule and the oxygen atoms in the Mordenite framework. AcOH and MA always adsorb most strongly through the oxygen atom in the carbonyl group. In the main channel, MA and AcOH adsorb more strongly than DME (0.14 eV, 0.07 eV) and MeOH (0.23 eV, 0.16 eV), so both species (especially MA) can potentially inhibit the initiation phase through blockage of the Brønsted acid sites. In the side pocket, MA adsorbs with a similar strength as DME (0.02 eV difference), but weaker than MeOH (0.08 eV). Consequently, MA may inhibit the formation of methyl groups from DME in the side pocket; the inhibition of the path starting from MeOH will likely be less severe. The adsorption energy of AcOH in the side pocket is lower than that of DME and MeOH by 0.09 eV and 0.19 eV, respectively. AcOH is therefore less likely than MA to inhibit the formation of methyl groups from DME; the formation of methyl groups from MeOH is not expected to be affected at all. Water is the molecule that adsorbs least strongly and should therefore not be able to block the Brønsted acid sites. However, we have only investigated single-molecule adsorption, and clusters of water molecules may be significantly more stable. This effect would be especially important in the side pockets, which have been shown experimentally to be the preferential location of water clusters [43].

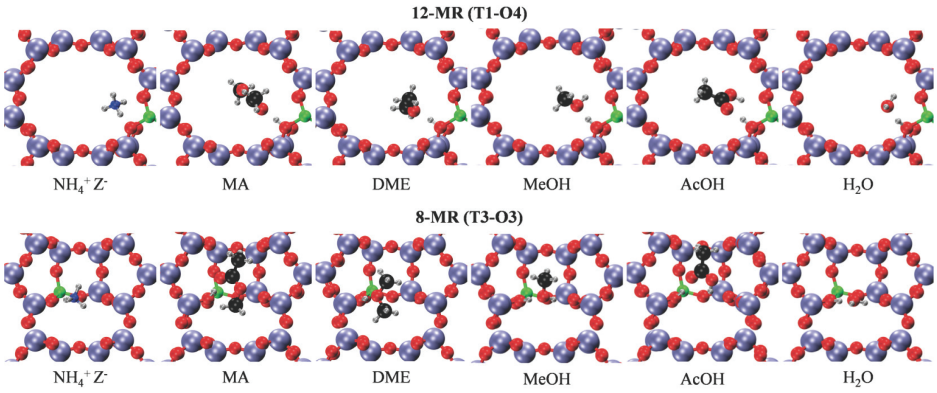

Figure 2. The optimized structures of the molecules typically found in the effluent gas during DME carbonylation on the Brønsted acid sites within the 12-MR on T1-O4 and the 8-MR on T3-O3.

To investigate the reaction path for MA synthesis, we have calculated the activation and reaction energies for the reactions [Eqn. (1) to Eqn. (4)] (Table 3).

In the main channel formation of the methyl groups from MeOH is faster than from DME (0.07 eV lower energy barrier), whereas in the side pocket both paths are equally active (0.01 eV difference in activation energies). The energy barriers for the reactions of DME and MeOH with a Brønsted acid site, are lower in the side pocket than in the main channel by 0.25 eV and 0.17 eV, respectively, showing that the reactions are significantly faster in the side pocket. Both DME and MeOH are protonated upon the reaction with the acid proton and the transition states involve a transfer of a methyl group to the zeolite (Figure3).

Table 3. Activation E_{act} and reaction ΔE energies (eV) for reactions [Eq. (1) to Eq. (4)] within the 12-MR on T1-O4 and the 8-MR on T3-O3.

Reaction	T1-O4		T3-O3	
	E_{act}	ΔE	E_{act}	ΔE
DME + H-Z → MeOH + CH_3-Z	0.62	0.02	0.37	0.01
MeOH + H-Z → H_2O + CH_3-Z	0.55	-0.18	0.38	-0.19
CO + CH_3-Z → CH_3CO^+ + Z^-	1.09	-0.09	1.03	-0.48
CH_3CO^+ → CH_3CO-Z	0.02	-0.81	0.01	-0.53
DME + CH_3CO-Z → CH_3-MA^+ + Z^-	0.00	-0.24	0.24	0.13
CH_3-MA^+ + Z^- → MA + CH_3-Z	0.58	-0.24	0.88	-0.48
MeOH + CH_3CO-Z → MA + H-Z	0.00	-0.50	0.02	-0.38
DME + CH_3-Z → TMO^+ + Z^-	0.36	-0.03	0.70	-0.09
H_2O + CH_3CO-Z → CH_3COOH + H-Z	0.06	-0.36	0.18	-0.24

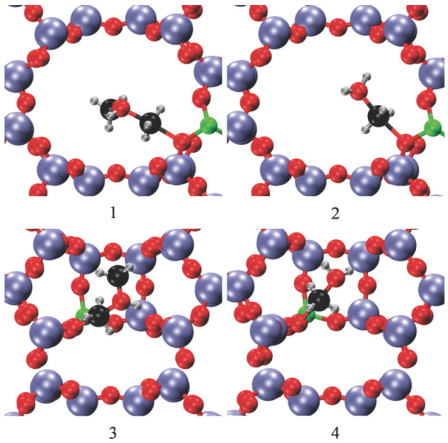

Figure 3. Optimized structures of the transition states for the reaction of: 1) DME with a Brønsted acid site within the 12-MR on T1-O4, 2) MeOH with a Brønsted acid site within the 12-MR on T1-O4, 3) DME with a Brønsted acid site within the 8-MR on T3-O3, 4) MeOH with a Brønsted acid site within the 8-MR on T3-O3.

The initiation phase of the MA synthesis ends when all Brønsted acid sites have reacted to methyl groups. In the first step of the steady-state phase, a methyl group reacts with CO to form an acetyl carbocation (Figure 4). This is the rate-limiting reaction step and the energy barrier for it is 0.06 eV lower in the side pocket than in the main channel. The optimized geometries of the reaction steps and transition states are shown in Figure 5 (T1-O4) and

Figure 6 (T3-O3). Next, the acetyl carbocation is restructured to acetyl with a very low energy barrier (T1-O4: 0.02 eV, T3-O3 0.01 eV). As we reported in a previous study, the acetyl carbocation can alternatively react to ketene with slightly higher activation energies (T1-O4: 0.09 eV, T3-O3: 0.12 eV) [44]. Ketene is then restructured to acetyl - this also occurs with low energy barriers (T1-O4: 0.18 eV, T3-O3: 0.12 eV). The surface acetyl reacts with DME, forming a cationic CH_3-MA complex, which subsequently decomposes to MA and a methyl group. The formation of the CH_3-MA complex occurs with no energy barrier in the main channel. The activation energy for this step is 0.24 eV in the side pockets. The transfer of the methyl group from the CH_3-MA complex to the zeolite proceeds with higher energy barriers (T1-O4: 0.58 eV, T3-O3: 0.88 eV) than the formation of the complex (T1-O4: 0.00 eV, T3-O3: 0.24 eV).

Under realistic experimental conditions some MeOH is always present in the system and for this reason we have also investigated the reaction between MeOH and the surface acetyl groups. This reaction occurs with no energy barrier in the main channel and with a very low (0.02 eV) energy barrier in the side pocket. This result shows that if MeOH is present in the system it will react very rapidly with the acetyl groups (much faster than DME), forming MA and a Brønsted acid site.

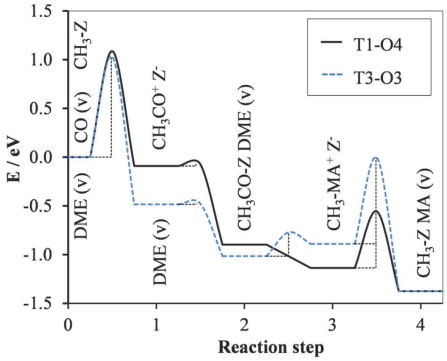

Figure 4. Reaction paths for formation of MA within the 12-MR on T1-O4 and the 8-MR on T3-O3. Reaction steps: 0 CO and DME in vacuum, methyl group on the zeolite; 1 Acetyl carbocation, DME in vacuum and negatively charged zeolite; 2 Acetyl group on zeolite, DME in vacuum; 3 CH_3-MA cation and negatively charged zeolite; 4 MA in vacuum, methyl group on zeolite. Black line: reaction steps in the main channel (T1-O4); Blue line: reaction steps in the side pocket (T3-O3).

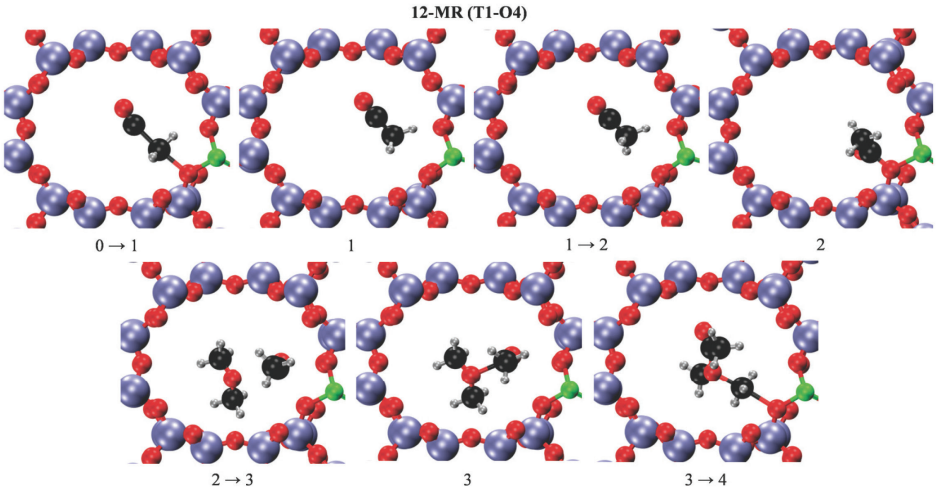

Figure 5. The optimized structures of the reaction intermediates and transition states for formation of MA within the 12-MR on T1-O4. Reaction steps: 0 CO and DME in vacuum, methyl group on the zeolite; 1 Acetyl carbocation, DME in vacuum and negatively charged zeolite; 2 Acetyl group on zeolite, DME in vacuum; 3 CH_3-MA cation and negatively charged zeolite; 4 MA in vacuum, methyl group on zeolite.

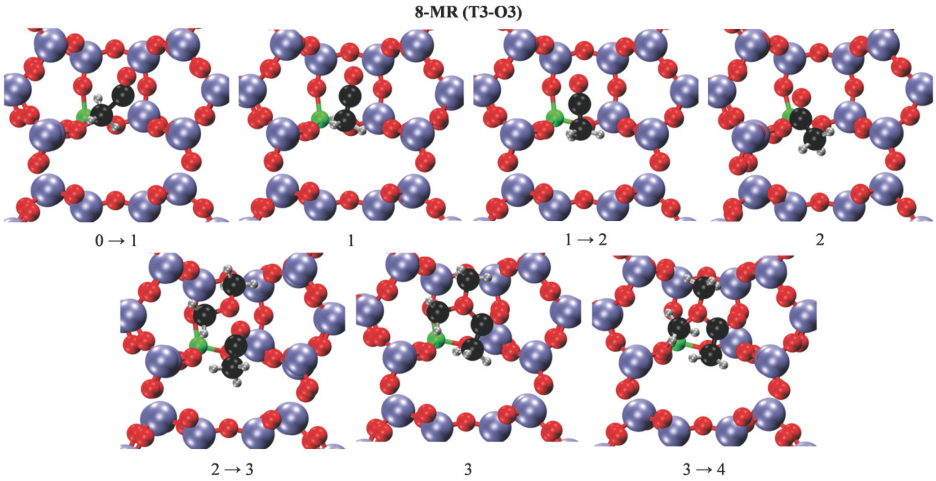

Figure 6. The optimized structures of the reaction intermediates and transition states for formation of MA within the 8-MR on T3-O3. Reaction steps: 0 CO and DME in vacuum, methyl group on the zeolite; 1 Acetyl carbocation, DME in vacuum and negatively charged zeolite; 2 Acetyl group on zeolite, DME in vacuum; 3 CH_3-MA cation and negatively charged zeolite; 4 MA in vacuum, methyl group on zeolite.

Two other reactions, which may play a role during DME carbonylation on Mordenite, are the formation of trimethyloxonium (TMO) species and AcOH. The energy barriers for the reaction of methyl groups with DME are 0.36 eV and 0.70 eV on T1-O4 and T3-O3, respectively – much less than for the reactions of methyl groups with CO (T1-O4: 1.09 eV, T3-O3: 1.03 eV). Thus, TMO is formed much faster than acetyl carbocations (which react to acetyl). However, unlike acetyl, TMO is not very stable – the formation energies on T1-O4 and T3-O3 are -0.03 eV and -0.09 eV, respectively. Consequently, TMO is probably not sufficiently stable to block the T1-O4 and T3-O3 sites, unless it rapidly reacts further to other, more stable species, such as hydrocarbons. The energy barriers for the reaction of acetyl with water (T1-O4: 0.06 eV, T3-O3: 0.18 eV) are lower than for the reaction with DME (T1-O4: 0.58 eV, T3-O3: 0.88 eV). This result shows that if any water is present in the system, acetic acid will be the main product instead of MA.

Our DFT calculations show that the attack of CO on a methyl group, the rate-limiting reaction step, is more facile in the side pocket than in the main channel (the 0.06 eV difference in barriers translates into a factor of about 5 on the rates at 438K). This is good agreement with previous experimental and theoretical studies [26-28]. Also, we see that the energy difference of 0.06 eV in barriers, compares very well with adsorption energy of ammonia being 0.10 eV larger in the side pocket than in the main channel. This confirms that the adsorption energy of ammonia is a good reactivity descriptor in solid acid catalysis, as proposed in the study of Wang et al. [45] and Brogaard et al. [46]. Additionally, we show that the reaction of DME with acetyl is significantly faster than the attack of CO on a methyl group, both in the main channel and the side pocket, which is in good agreement with the experimental results [19, 20]. In the previous studies of Boronat et al. [28], it was shown that the reaction between acetyl and DME does not occur in a number of geometries, where one of the species is in the side pocket and the other in the 8-MR channel below the side pocket. In our study, we present a reaction path, in which acetyl is formed from a methyl group on the T3-O3 site (Figure 6) - this results in an adsorption geometry of acetyl that makes it possible to react with DME completely inside the side pocket. This new reaction path requires much lower activation energy than the paths investigated in the previous studies.

3.2 Experimental study of the reaction path

The DFT study of the reaction mechanism (Section 3.1) has shown that the carbonylation of the surface methyl groups is the rate-limiting reaction step and the reaction rate is higher in the side pockets; the subsequent reaction of the formed surface acetyl with DME is comparatively fast. Additionally, MA can potentially block the Brønsted acid sites in the main channel, and to a lesser extent in the side pockets. In this section, the results of the complementary experimental study of the reaction path are presented.

Figure 7 shows the rate of MA synthesis at a fixed total pressure of 10 bar and various DME concentrations in CO. The reaction rate is constant (0.68 mol(mol Al)$^{-1}$h^{-1}) for DME concentrations between 0.5 % (33 % DME conversion) and 2 % (9 % DME conversion). At the DME concentration of 0.15 % (85 % DME conversion) the reaction rate decreases by 19 % to a value of 0.55 mol(mol Al)$^{-1}$h^{-1}. These results show that the rate of MA synthesis does not depend on the DME pressure even at a value as low as 0.0335 bar (10 bar total pressure, 67 % of 0.5 vol%). This is in good agreement with previous experimental studies of Cheung et al. [19, 20]. At high DME conversions, the local DME pressure varies noticeably throughout the catalyst bed; the back end of the catalyst experiences a considerably lower DME pressure than the front end. Under these conditions, the rate of MA synthesis shows dependence on the DME pressure.

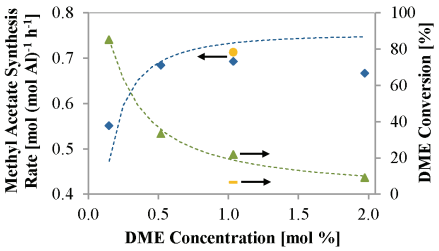

Figure 7. MA synthesis rate and DME conversion as functions of DME concentration in CO at a total pressure of 10 bar: (♦) Measured MA synthesis rate, 1.5 g catalyst; (▲) Measured DME conversion, 1.5 g catalyst; The dashed lines are the values calculated using the kinetic model, 1.5 g catalyst; (•) Measured MA synthesis rate, 0.5 g catalyst; (-) Measured DME conversion, 0.5 g catalyst.

For a fixed composition of the reaction mixture (2% DME in CO), the rate of MA synthesis increases with increasing total pressure (Figure 8). However, the relationship is not linear. The measured reaction rates should lie on a straight line because the reaction does not depend on the DME pressure under these conditions and is first order in the CO pressure. Also, it has been confirmed that the measured reaction rates were not limited by the diffusion (Appendix A). To test whether the reaction is inhibited by MA, we performed 2 experiments

with a reduced catalyst amount. In the experiment performed at 10 bar and 1% DME in CO (Figure 7), the reduction of the catalyst mass to 1/3 decreased the DME conversion from 22 % to 7 %, but the normalized reaction rate remained unchanged (<3 % change). In the experiment at 100 bar and 2% DME in CO (Figure 8), the reduction of the catalyst amount to 1/10 reduced the conversion from 39 % to 6 % and the normalized MA synthesis rate increased by 39 %. These results show that MA synthesis is inhibited by the reaction product if its partial pressure is sufficiently high. In the experiment at 10 bar, the DME conversion and thereby the MA pressure is too low to cause any appreciable inhibition of the reaction. Thus, a further lowering of the DME conversion by a reduction of the catalyst amount and the resulting decrease of MA pressure does not have any effect on the reaction rate. In the experiment at 100 bar, the conversion of DME is high (39 %) and the resulting pressure of MA in the catalyst bed is also significant. By reducing the catalyst amount to 1/10, the conversion of DME and thereby the MA pressure is reduced to 1/7 of the initial value. Consequently, the inhibition of the reaction rate by MA is significantly diminished.

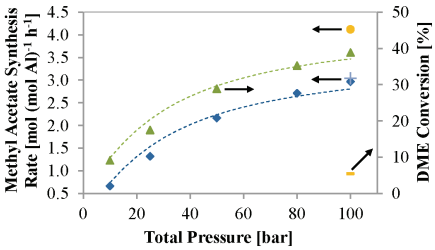

Figure 8. MA synthesis rate as a function of total reaction pressure (2 % DME in CO): (♦) Measured MA synthesis rate, 1.5 g catalyst; (▲) Measured DME conversion, 1.5 g catalyst; The dashed lines are the values calculated using the kinetic model, 1.5 g catalyst; (●) Measured MA synthesis rate, 0.15 g catalyst; (-) Measured DME conversion, 0.15 g catalyst. (+) Measured MA synthesis rate (100 bar, 1.1 % DME in CO, 1.5 g catalyst).

To examine the nature of the MA inhibition further, we performed an experiment at 100 bar, in which the concentration of DME in CO was reduced from 2 % to 1 % (Figure 8). Despite the reduction of the DME pressure in the system, the reaction rate remained the same

showing that MA does not react with acetyl; a reaction, in which MA would compete with DME and the reaction rate would depend on the DME pressure. Thus, it seems likely that MA suppresses the reaction by rendering the methyl groups inactive.

Our DFT model shows that the formation of the cationic CH_3-MA complexes from a methyl group and a MA molecule in vacuum is endothermic both in the main channel (0.24 eV) and in the side pocket (0.48 eV). Consequently, the CH_3-MA species are not very stable and cannot explain the detrimental effect of MA on the reaction rate. However, MA may be weakly bound to the methyl groups by hydrogen bonds, making them inaccessible for the reaction with CO. Currently, the exact nature of the inactive complexes between the methyl groups and MA remains equivocal.

3.3 Development of the kinetic model of the steady-state reaction phase

To describe the state of the catalyst under experimental conditions in steady state (after the initiation phase), we develop a kinetic model based on the experimental data in section 3.2. Our DFT calculations show that the activation energies for the carbonylation of the methyl groups are significantly lower than the energy barriers for the reverse reaction (> 0.9 eV difference, Table 3). Consequently, we assume an irreversible reaction of CO with a methyl group, in which acetyl is formed [Eqs. (5)]. The irreversibility of the reaction of CO with a methyl group has been shown experimentally in previous studies [19, 20].

$$CO + CH_3 - Z \overset{k_1}{\rightarrow} CH_3CO - Z \quad (5)$$

The methyl group can react with MA, in a quasi-equilibrated reaction, forming an inactive complex C:

$$MA + CH_3 - Z \overset{K_2}{\Leftrightarrow} C - Z \quad (6)$$

Acetyl reacts with DME, in a quasi-equilibrated reaction, forming MA and regenerating the methyl group:

$$DME + CH_3CO - Z \overset{K_3}{\Leftrightarrow} MA + CH_3 - Z \quad (7)$$

The elementary reactions [Eq. (5)] to [Eq. (7)], the quasi-equilibrium assumption for the reactions [Eq. (6)] and [Eq. (7)], and a steady-state approximation lead to the following rate expression for MA synthesis rate:

$$r_{MA} = \frac{k_1 p_{CO}}{1+K_2 p_{MA}+K_3^{-1}\frac{p_{MA}}{p_{DME}}} \quad (8)$$

The rate expression [Eq. (8)] shows that the reaction rate is proportional to the pressure of CO. The first term describing the MA inhibition is proportional to the MA pressure and the equilibrium constant for reaction [Eq. (6)]. The second MA-inhibition term is proportional to the MA pressure and inversely proportional to the DME pressure. Thus, it will become prominent at high MA pressures and low DME pressures; which is the case at high DME conversions.

We determine the rate constants k_1, K_2, and K_3 by modeling the catalyst system as a plug flow reactor and fitting the rate constants to the experimental data using non-linear least squares regression. Figure 7 and Figure 8 show the rates of MA synthesis and the conversion degrees of DME, as measured experimentally and calculated using the kinetic model. As seen in Figures 7 and 8 the developed kinetic model provides an excellent description of all experimental data, showing that the assumptions made in the model are fully consistent with the experiments.

Using the kinetic model, we have calculated the coverage of the surface species as a function of the catalyst mass at 10 bar and 100 bar (Figure 9), to obtain information on the state of the catalyst surface under experimental conditions. At the total pressure of 10 bar, methyl, acetyl, and CH_3-MA cover 87%, 5% and 8% of the catalyst surface, respectively, at

the reactor outlet, thus showing that methyl groups are the most abundant surface intermediate. The CH_3-MA complexes, which block the methyl groups that are necessary for further reactions, cover only 8 % of the surface, reflecting a very limited MA inhibition at these conditions. In the high pressure limit, at 100 bar, the surface coverages of methyl, acetyl, and CH_3-MA are 21 %, 7 %, and 72 %, respectively, at the reactor outlet, and the MA coverage quickly grows to about 50 % after about 1/6 of the catalyst mass. This result shows that in this limit, the majority of the methyl groups is blocked as inactive CH_3-MA complexes and is not available for the reaction with CO. The surface coverage of acetyl is low (7%); however, it is 28 % higher compared to the acetyl coverage at 10 bar.

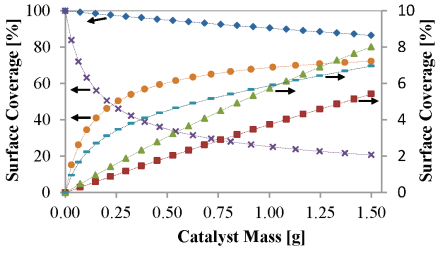

Figure 9. Surface coverage profiles of methyl, acetyl, and CH_3-MA complexes through the catalyst, calculated using the kinetic model. 10 bar, 2 % DME in CO, Surface coverage of: (♦) Methyl, (■) Acetyl, (▲) Methyl-MA complex. 100 bar, 2 % DME in CO, Surface coverage of: (×) Methyl, (-) Acetyl, (●) Methyl-MA complex.

At differential reaction conditions, the MA pressure in the catalyst is very low, and the rate expression [Eq. (4)] reduces to:

$$r_{MA} \approx k_1 p_{CO} \tag{5}$$

Thus, our results are in good agreement with the previous experimental studies [19, 20], in which the DME carbonylation on Mordenite was studied at differential reaction conditions. Additionally, the rate expression [Eq. (8)] which we propose here, is also able to describe the

reaction rates at high DME conversions, which are interesting from the industrial point of view.

4 Conclusion

Our detailed DFT study of the DME carbonylation on Mordenite shows that the reaction of CO with a surface methyl group, the rate-limiting step, is faster in the side pocket than in the main channel. The difference between the energy barriers for the rate limiting step at these two sites compares very well to the difference in adsorption energies of ammonia, confirming that the adsorption energy of ammonia is a good activity descriptor in solid acid catalysis. Also, we demonstrate that the reaction of DME with a surface acetyl, a reaction in which MA is formed and the methyl group is regenerated, is possible in the side pocket and is not rate-limiting – a result which was not previously known. Additionally, we show that MA and AcOH adsorb stronger than DME and MeOH on the Brønsted acid sites in the main channel, which can explain why cofeeding of MA and AcOH inhibits the deactivation of Mordenite during DME carbonylation [47]. In the side pocket, MA adsorbs on the Brønsted acid site with a similar strength as DME and MeOH. Consequently, the length of the initiation phase may depend of the MA pressure. Our experimental results show that MA inhibits the reaction rate of MA synthesis by forming inactive complexes with surface methyl groups. The kinetic model that we have developed for the steady-state phase of the reaction includes the effect of MA inhibition and provides an excellent description of the experimental data.

Acknowledgments

The project is financed by the Technical University of Denmark (DTU) and the Catalysis for Sustainable Energy research initiative (CASE), funded by the Danish Ministry of Science, Technology and Innovation.

Appendix A.

Assuming that the catalyst particles are spherical the effectiveness factor (η) can be calculated using equation [Eq. (A.1)]:

$$\eta = \frac{3}{\varphi}\left(\frac{1}{\tanh\varphi} - \frac{1}{\varphi}\right) \quad \text{(A.1)}$$

The Thiele modulus (φ) is given by equation [Eq. (A.2)]:

$$\varphi = R \cdot \sqrt{\frac{k \cdot \rho}{D_{eff}}} \quad \text{(A.2)}$$

where R is the particle radius, k is the reaction rate, ρ is the particle density and D_{eff} is the effective diffusivity, which is calculated as:

$$D_{eff} = \frac{D_{12} \cdot \phi_p}{\tau} \quad \text{(A.3)}$$

where D_{12} is the binary diffusion coefficient, ϕ_p is the particle porosity and τ is the tortuosity. D_{12} for the diffusion of DME in CO is $2.29 \cdot 10^{-3}$ $cm^2 \cdot s^{-1}$, calculated using the method of Brokaw for polar gases and Lennard-Jones potentials [48, 49]. The parameter values used in the calculations are: particle radius $R = 93.8$ µm (the middle of the used sieve interval), rate constant $k = 1.18 \cdot 10^{-3} cm^3 \cdot g^{-1} \cdot s^{-1}$ (the highest rate constant, k_1, in the kinetic model), the pressure of 100 bar (the highest reaction pressure), particle density $\rho = 1.09\, g \cdot cm^{-3}$, porosity $\phi_p = 0.36$ and tortuosity $\tau = 5.6$ [50]. The Thiele modulus and effectiveness factor are $2.78 \cdot 10^{-3}$ and 1.00, respectively. Thus, the reaction is not limited by the diffusion.

References

[1] J.L. Keller, Hydrocarb. Process. 58 (1979) 127.
[2] I. Wender, Fuel Process. Technol. 48 (1996) 189.
[3] R.G. Herman, Catal. Today 55 (2000) 233.
[4] M.M. Bhasin, W.J. Bartley, P.C. Ellgen, T.P. Wilson, J. Catal. 54 (1978) 120.
[5] M. Ichikawa, Bull. Chem. Soc. Jpn. 51 (1978) 2273.
[6] P. Courty, D. Durand, E. Freund, A. Sugier, J. Mol. Catal. 17 (1982) 241.
[7] K.J. Smith, R.B. Anderson, Can. J. Chem. Eng. 61 (1983) 40.
[8] J.G. Nunan, C.E. Bogdan, K. Klier, K.J. Smith, C.W. Young, R.G. Herman, J. Catal. 116 (1989) 195.
[9] E. Tronconi, L. Lietti, P. Forzatti, I. Pasquon, Appl. Catal. 47 (1989) 317.
[10] P. Courty, P. Chaumette, C. Raimbault, P. Travers, Rev. Inst. Fr. Pet. 45 (1990) 561.
[11] J.A. Dalmon, P. Chaumette, C. Mirodatos, Catal. Today 15 (1992) 101.
[12] J.M. Christensen, P.M. Mortensen, R. Trane, P.A. Jensen, A.D. Jensen, Appl. Catal., A 366 (2009) 29.
[13] J.M. Christensen, P.A. Jensen, N.C. Schiodt, A.D. Jensen, Chemcatchem 2 (2010) 523.
[14] J.M. Christensen, P.A. Jensen, A.D. Jensen, Ind. Eng. Chem. Res. 50 (2011) 7949.
[15] X. San, Y. Zhang, W. Shen, N. Tsubaki, Energy Fuels 23 (2009) 2843.
[16] X. Li, X. San, Y. Zhang, T. Ichii, M. Meng, Y. Tan, N. Tsubaki, ChemSusChem 3 (2010) 1192.
[17] Y. Zhang, X. San, N. Tsubaki, Y. Tan, J. Chen, Ind. Eng. Chem. Res. 49 (2010) 5485.
[18] P. Haro, P. Ollero, A.L.V. Perales, C.R. Valle, Energy 44 (2012) 891.
[19] P. Cheung, A. Bhan, G.J. Sunley, E. Iglesia, Angew. Chem., Int. Ed. 45 (2006) 1617.
[20] P. Cheung, A. Bhan, G.J. Sunley, D.J. Law, E. Iglesia, J. Catal. 245 (2007) 110.
[21] J. Liu, H. Xue, X. Huang, Y. Li, W. Shen, Catal. Lett. 139 (2010) 33.
[22] J.L. Liu, H.F. Xue, X.M. Huang, P.H. Wu, S.J. Huang, S.B. Liu, W.J. Shen, Chin. J. Catal. 31 (2010) 729.
[23] H.F. Xue, X.M. Huang, E. Ditzel, E.S. Zhan, M. Ma, W.J. Shen, Ind. Eng. Chem. Res. 52 (2013) 11510.
[24] H.F. Xue, X.M. Huang, E. Ditzel, E.S. Zhan, M. Ma, W.J. Shen, Chin. J. Catal. 34 (2013) 1496.
[25] H.F. Xue, X.M. Huang, E.S. Zhan, M. Ma, W.J. Shen, Catal. Commun. 37 (2013) 75.
[26] A. Bhan, A.D. Allian, G.J. Sunley, D.J. Law, E. Iglesia, J. Am. Chem. Soc. 129 (2007) 4919.
[27] M. Boronat, C. Martinez-Sanchez, D. Law, A. Corma, J. Am. Chem. Soc. 130 (2008) 16316.
[28] M. Boronat, C. Martinez, A. Corma, Phys. Chem. Chem. Phys. 13 (2011) 2603.
[29] J.J. Mortensen, L.B. Hansen, K.W. Jacobsen, Phys. Rev. B 71 (2005).
[30] J. Enkovaara, C. Rostgaard, J.J. Mortensen, J. Chen, M. Dulak, L. Ferrighi, J. Gavnholt, C. Glinsvad, V. Haikola, H.A. Hansen, H.H. Kristoffersen, M. Kuisma, A.H. Larsen, L. Lehtovaara, M. Ljungberg, O. Lopez-Acevedo, P.G. Moses, J. Ojanen, T. Olsen, V. Petzold, N.A. Romero, J. Stausholm-Moller, M. Strange, G.A. Tritsaris, M. Vanin, M. Walter, B. Hammer, H. Hakkinen, G.K.H. Madsen, R.M. Nieminen, J.K. Norskov, M. Puska, T.T. Rantala, J. Schiotz, K.S. Thygesen, K.W. Jacobsen, J. Phys.: Condens. Matter 22 (2010).
[31] S.R. Bahn, K.W. Jacobsen, Comput. Sci. Eng. 4 (2002) 56.
[32] H.J. Monkhorst, J.D. Pack, Phys. Rev. B 13 (1976) 5188.

[33] J. Wellendorff, K.T. Lundgaard, A. Mogelhoj, V. Petzold, D.D. Landis, J.K. Norskov, T. Bligaard, K.W. Jacobsen, Phys. Rev. B 85 (2012).
[34] A. Alberti, P. Davoli, G. Vezzalini, Z. Kristallogr. 175 (1986) 249.
[35] C.G. Broyden, Math. Comput. 24 (1970) 365.
[36] R. Fletcher, Comput. J. 13 (1970) 317.
[37] D. Goldfarb, Math. Comput. 24 (1970) 23.
[38] D.F. Shanno, Math. Comput. 24 (1970) 647.
[39] G. Henkelman, B.P. Uberuaga, H. Jonsson, J. Chem. Phys. 113 (2000) 9901.
[40] E. Bitzek, P. Koskinen, F. Gaehler, M. Moseler, P. Gumbsch, Phys. Rev. Lett. 97 (2006).
[41] H.G. Karge, V. Dondur, J. Phys. Chem. 94 (1990) 765.
[42] O. Marie, P. Massiani, F. Thibault-Starzyk, J. Phys. Chem. B 108 (2004) 5073.
[43] A. Zecchina, G. Spoto, S. Bordiga, Phys. Chem. Chem. Phys. 7 (2005) 1627.
[44] D.B. Rasmussen, J.M. Christensen, B. Temel, F. Studt, P.G. Moses, J. Rossmeisl, A. Riisager, A.D. Jensen, Angew. Chem., Int. Ed. (2015) n/a.
[45] C.M. Wang, R.Y. Brogaard, B.M. Weckhuysen, J.K. Norskov, F. Studt, J. Phys. Chem. Lett. 5 (2014) 1516.
[46] R.Y. Brogaard, C.M. Wang, F. Studt, ACS Catal. 4 (2014) 4504.
[47] N.J. Hazel, L.A. Key, M.S. Roberts, J.G. Sunley, US Patent 8 624 054 B2 (2014), to BP Chemicals Limited.
[48] R.S. Brokaw, Ind. Eng. Chem. Process Des. Dev. 8 (1969) 240.
[49] B.E. Poling, J.M. Prausnitz, J.P. O'Connell, The Properties of Gases and Liquids, McGraw-Hill, New York, 2001.
[50] A.K. Aboulgheit, M.F. Menoufy, A.K. Elmorsi, S.M. Abdelhamid, Zeolites 7 (1987) 353.

3.5 A study of the deactivation of Mordenite during dimethyl ether carbonylation to methyl acetate

As a first step in the investigation of Mordenite deactivation, we performed a series of DME carbonylation experiments at a fixed total pressure and various DME concentrations in CO. The space time yield (STY) of MA and MeOH during these experiments, are shown in Figure 7 and the conversion of DME and selectivity towards MA are shown in Figure 8. Because the reaction rate of MA synthesis does not depend on the DME pressure, the maximum STY of MA is largely the same in all experiments.

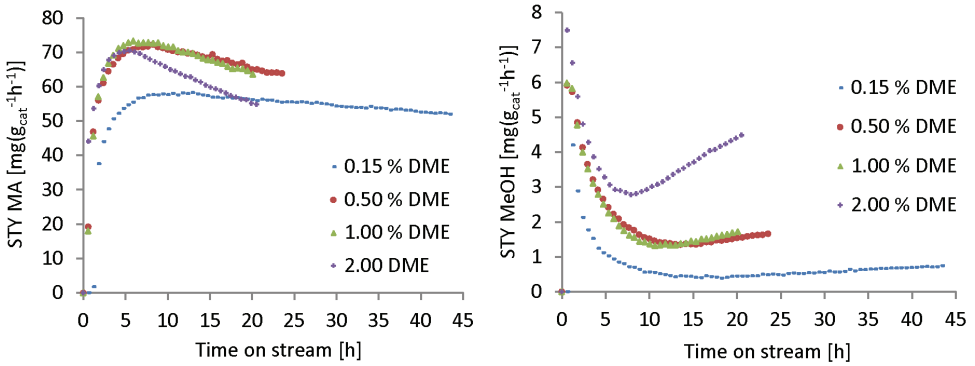

Figure 7. Space time yield of methyl acetate (left) and methanol (right) as a function of time on stream during DME carbonylation on Mordenite. Reaction conditions: 10.0 bar total pressure, 0.15 % - 2.00 % DME in CO, 300 Nml min^{-1}, 1.5 g catalyst, 438 K.

In the experiment with 0.15 % DME in CO, the maximum reaction rate is slightly lower than in the other experiments, due to a very low concentration of DME; this effect is discussed in section 3.2. The product selectivity towards MA is high (> 97 %) in all experiments, except the experiment with the highest DME concentration (2 %), in which the selectivity towards MA peaks at 95 % and declines as the catalyst deactivates. The catalysts deactivate at different rates, depending on the DME concentration in the feed; at the highest DME concentration the deactivation is most rapid, and as the DME concentration in the feed decreases, the deactivation is slower.

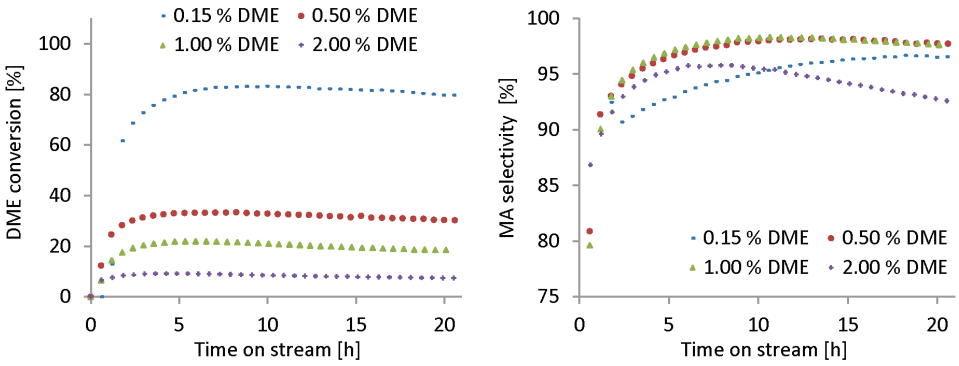

Figure 8. DME conversion (left) and selectivity towards MA based on C mol % (right) as a function of time on stream during DME carbonylation on Mordenite. Reaction conditions: 10.0 bar total pressure, 0.15 % - 2.00 % DME in CO, 300 Nml min^{-1}, 1.5 g catalyst, 438 K.

The STY of MeOH is high in the initiation phase of the experiments and reaches minimum at the steady-state phase. After the steady-state has been reached and the deactivation begins, the MeOH signal again increases in strength. In all experiments, there is a clear correlation between the deactivation degree of the catalyst and the STY of MeOH: the STY of MeOH increases with the deactivation degree. The deactivation is due to formation of coke and thereby is not reversible (except by burning off the coke). To obtain a measure of the deactivation rate, we define the deactivation degree D_X as:

$$D_X = \frac{STY_{MA}^{max} - STY_{MA}}{STY_{MA}^{max}} \cdot 100\% \qquad (13)$$

STY_{MA}^{max} is the maximum STY of MA during an experiment and STY_{MA} is the STY at a given time after STY_{MA}^{max} has been reached. In the expression for D_X it is assumed that the deactivation begins after the steady-state has been reached. This is not necessarily true. However, we use this approximation until a better one becomes available. Figure 9 (left) shows plots of the deactivation degree, D_X, as a function of the deactivation time. The plots of D_X are straight lines, showing that the catalysts deactivate at a constant rate, which is the slope of the line. The straight lines in Figure 9 go almost perfectly through the origin and the small deviation can be explained by the maximum STY of MA, as shown in Figure 7, is not a single point, but is rather spread over some time. The slopes of the plots of D_X express the rate at which the rate of MA synthesis decreases (the deactivation rate). A plot of the deactivation rates as a function of the average DME pressure in the catalyst bed during the experiment is shown in Figure 9 (right). The points lie on a straight line,

showing that for a fixed reaction rate and thereby a fixed pressure of MA in catalyst bed, the deactivation rate is proportional to the average DME pressure in the catalyst bed.

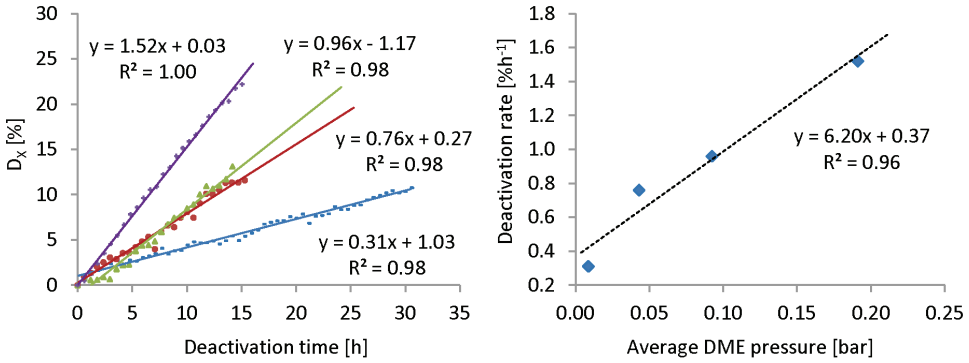

Figure 9. Left: the deactivation degree X_D as a function of deactivation time. Blue: 0.15 % DME; Red: 0.50 % DME; Green: 1.00 % DME; Purple: 2.00 % DME. Right: Deactivation rate as a function of the average DME pressure in the catalyst bed during DME carbonylation on Mordenite. Reaction conditions: 10.0 bar total pressure, 0.15 % - 2.00 % DME in CO, 300 Nml min^{-1}, 1.5 g catalyst, 438 K.

As a next step, a series of experiment has been performed in which the composition of the feed is fixed at 2 % DME in CO, but the total pressure changes. Figure 10 shows the STY of MA and MeOH as a function of time on stream during the experiments. In all experiments, the steady-state phase is reached after the initiation period, and after that the catalysts loses activity due to deactivation. The STY of MeOH decrease in the initiation phase, and gain in strength in the deactivation period. The conversion of DME reaches its maximum at the steady-state and declines in the deactivation period (Figure 11). The product selectivity towards MA is high in all experiments (> 97 %), except the experiment at 10 bar, as already mentioned. Additionally, the product selectivity towards MA decreases as the catalyst deactivates. Figure 12 shows the deactivation degree of the catalyst as a function of the deactivation time.

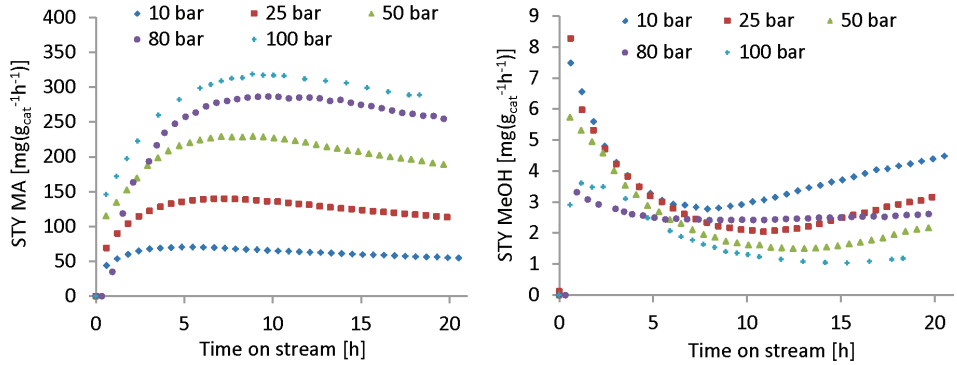

Figure 10. Space time yield of methyl acetate (left) and methanol (right) as a function of time on stream during DME carbonylation on Mordenite. Reaction conditions: 10.0 bar – 100.0 bar total pressure, 2.00 % DME in CO, 300 Nml min^{-1}, 1.5 g catalyst, 438 K.

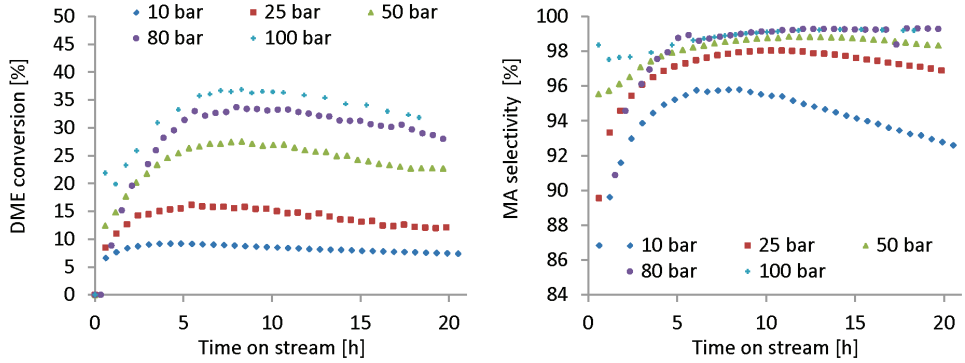

Figure 11. DME conversion (left) and selectivity towards MA based on C mol % (right) as a function of time on stream during DME carbonylation on Mordenite. Reaction conditions: 10.0 bar – 100.0 bar total pressure, 2.00 % DME in CO, 300 Nml min^{-1}, 1.5 g catalyst, 438 K.

In contrast to the experiments at a fixed total pressure, in the experiments with a fixed feed composition there is weak negative correlation between the deactivation rate and the average DME pressure in the catalyst bed (Figure 12, right). This demonstrates that reaction rate and thereby the average pressure of MA in the catalyst bed also affects the deactivation rate. The precise dependence of the deactivation rate on the DME and MA remains, however, not well understood. Although, MA is seen to inhibit the deactivation rate.

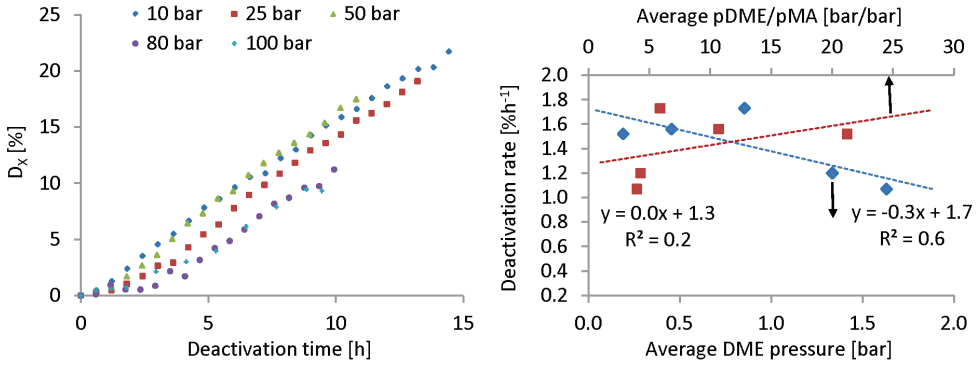

Figure 12. Left: the deactivation degree X_D as a function of deactivation time. Right: Deactivation rate as a function of the average DME pressure or a ratio between the average DME and MA pressure in the catalyst bed during DME carbonylation on Mordenite. Reaction conditions: 10 bar – 100 bar total pressure, 2.00 % DME in CO, 300 Nml min^{-1}, 1.5 g catalyst, 438 K.

We have performed temperature programmed oxidation experiments on the spent catalyst used for the deactivation tests at a fixed feed mixture to obtain information on the type of coke deposited during the experiments. The results of the TPO analysis are shown in Figure 13. The ratio between the hard coke and soft coke depends strongly on the total reaction pressure, and is highest for the experiment performed at 10 bar and decreases with increasing total pressure.

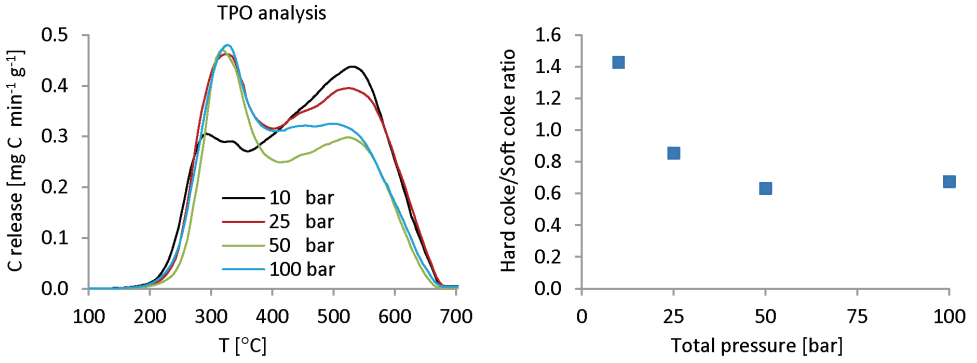

Figure 13. Left: the TPO analysis of the spent catalysts used for deactivation experiments. Right: the ratio between the areas of the TPO peaks corresponding to the hard and soft coke. Reaction conditions: 10 bar – 100 bar total pressure, 2.00 % DME in CO, 300 Nml min^{-1}, 1.5 g catalyst, 438 K.

The analyzed catalysts were on stream for approximately 20 h (10 bar: 21 h; 25 bar: 20 h, 50 bar: 20 h; 100 bar: 18.3 h). However, the deactivation times for the catalysts were different because of the different durations of the initiation phase. Consequently, we can conclude that it is advantageous to run the reaction at high pressures because it reduces the deactivation rate and the ratio between hard coke and soft coke, making a regeneration process easier. Figure 14 shows the total amount of MA and MeOH produced in the deactivation experiments. The amount MA increases with

increasing pressure, although the gain is largest for increasing the pressure from 10 bar to 50 bar. For higher pressures the improvements are smaller.

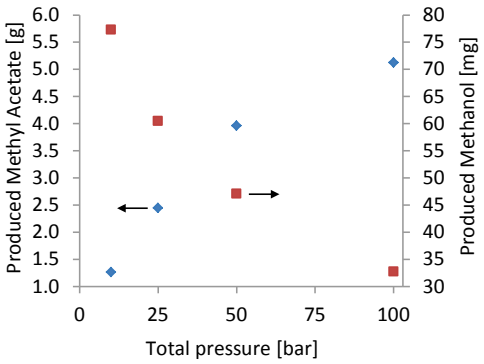

Figure 14. The total amount of methyl acetate and methanol produced in the deactivation experiments. Reaction conditions: 10 bar – 100 bar total pressure, 2.00 % DME in CO, 300 Nml min^{-1}, 1.5 g catalyst, 438 K.

In this section the results of the deactivation study of Mordenite under MA synthesis conditions were presented. For a fixed pressure of CO and thereby a fixed reaction rate, the rate of catalyst deactivation is proportional to the average DME pressure in the catalyst bed. If the DME concentration in the feed is fixed, the deactivation rate decreases with increasing total pressure, the exact nature of this effect remains, however, equivocal. It is advantageous to run DME carbonylation at high pressures, as increasing the reaction pressure increases the amount of MA the catalyst can produce in its life time and reduces the amount of hard coke that is formed.

4 Conclusion

In this project the reaction mechanism of dimethyl ether (DME) carbonylation to methyl acetate (MA) on Mordenite was studied experimentally and by density function theory (DFT) calculations. It was demonstrated experimentally that ketene (C_2H_2O) is a reaction intermediate, a result predicted by the DFT calculations. This is a novel result, which was not known previously. Ketene is a reactive molecule that easily forms polymers and its presence in the catalyst during the MA synthesis may be related to the rapid catalyst deactivation.

The kinetic study of the reaction has revealed that MA inhibits the reaction rate. A kinetic model that takes the effect of MA inhibition into account was developed. The model describes the reaction rate at the steady-state and provides an excellent description of the experimental data. The inhibition of the reaction rate by MA sets a limit on the conversion of reactants, which can be achieved in a process. This is an undesirable property in the industrial perspective.

A deactivation study of Mordenite has revealed that the deactivation rate of the catalyst is proportional to the average DME pressure in the catalyst bed for a fixed MA pressure. MA inhibits the deactivation rate. These results show that the catalyst should be operated at as low DME pressures as possible. A practical realization of such an operation mode would be a reactor in which DME is gradually added along the reactor, so the DME pressure is low everywhere in the catalyst bed. However, the effect of MA inhibition needs to be mitigated before a practical reactor for MA synthesis can be designed.

5 Future work

Currently, Mordenite is not very attractive as a catalyst for DME carbonylation because of its rapid deactivation and the undesirable property that the reaction rate is inhibited by the product. An effective solution of the stability problem requires a more comprehensive study of the deactivation mechanism. A better understanding of the reactions leading to catalyst deactivation could potentially make it possible to inhibit them and thereby prolong the time the catalyst can be used before a regeneration is necessary. The inhibition of the reaction rate by MA requires another study of the possible modifications of Mordenite, which could make the methyl groups react selectively with CO instead of reacting with MA. It has been shown in a study of Blasco et al. that a Cu modified Mordenite produces MA during MeOH carbonylation, while an unmodified Mordenite produces acetic acid [55]. The reaction mechanism proposed in this study involves an active site composed of a bridged Brønsted acid site and a neighboring Cu^+. Methyl groups are formed on the Brønsted acid sites, while Cu^+ activates CO and preferentially binds DME compared to MeOH and water. If Cu^+ adsorbs CO and activates it preferentially to MA this system could potentially also be useful for DME carbonylation. A study of this system and of Mordenite exchanged with other metal cations could potentially contribute to an enhancement of the properties of Mordenite.

6 Appendix

6.1 Optimization of the unit cell of Mordenite

In this study only the unit cell of purely siliceous Mordenite was optimized and the obtained parameters were used in the following calculations. This is a reasonable approximation because it was shown in a DFT study of Mordenite, by Demuth et al. [56] that a substitution of a single Si with Al in the framework had a minimal effect on the lattice constants and could be neglected.

The optimization was carried out in two steps. First, the unit vectors were homogenously scaled from 95% to 105% of the experimental values. The relation between the volume V and the homogenous scaling factor x, is:

$$V_x = xa \cdot xb \cdot xc \ , x \in [0.95; 1.05] \qquad (14)$$

The volume of the unit cell changes correspondingly from 86% (0.95^3) to 116% (1.05^3). Five, equispaced values of x are chosen and the total energies of the resulting systems are calculated:

$$E^{total}(x) \qquad (15)$$

Table 2 shows a plot of the energy as a function of x. The points are fitted with a fourth order polynomial and the optimal value of x, x_v, is found by calculating the minimum of the polynomial. This is a crude estimation of the optimal volume, and it was only used to get an approximate value the scaling factor, x_v.

Table 2. Optimization of the unit cell of Mordenite, using homogenous scaling of the unit vectors. Calculations were made using the RPBE exchange-correlation functional.

x	E^{total} [eV]
0.950	-1070.7665
0.975	-1080.9676
1.000	-1086.9587
1.025	-1087.9941
1.050	-1081.8133
x_v=1.0172	E_v=-1088.3094

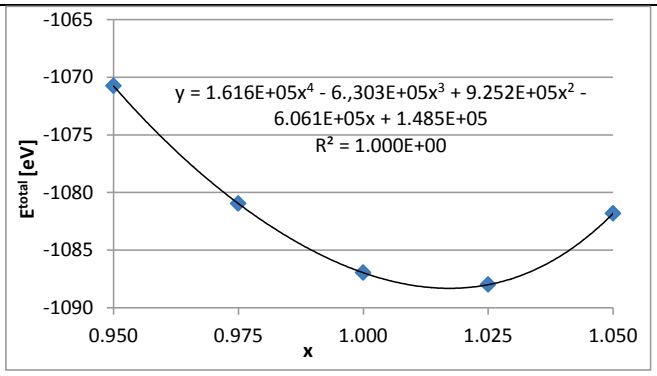

Next, the vector lengths, obtained from the first step, were varied independently. In the first run, the scaling factors: x, y and z, were scanned in a broad interval:

$$x, y, z \in [x_v - 0.05; x_v + 0.05] \qquad (16)$$

The calculations are computationally very demanding so only three equispaced values for every scaling factor were used:

$$x \in [x_1, x_2, x_3]$$
$$y \in [y_1, y_2, y_3] \qquad (17)$$
$$z \in [z_1, z_2, z_3]$$

This amounted to a total of 27 total energy values:

$$E^{total}(x, y, z) \qquad (18)$$

A second order polynomial was fitted to the data, using the polyfit function of ASE. The resulting approximation, $E_{poly}^{total}(x, y, z)$ gave the total energy of the system as a function of the scaling parameters. The values of x, y and z, minimizing the total energy, were found by calculation the minimum of E_{poly}^{total}. This was done using the BFGS algorithm in ASE. The optimized values are called x_{min1}, y_{min1}, z_{min1}. This procedure was repeated and the scaling vectors were scanned in a narrow interval, using the optimized scaling factors:

$$x \in [x_{min1} - 0.01; x_{min1} + 0.01]$$
$$y \in [y_{min1} - 0.01; y_{min1} + 0.01] \qquad (19)$$
$$z \in [z_{min1} - 0.01; z_{min1} + 0.01]$$

While varying the scaling factors individually, it was confirmed that the sampled interval was large enough. This was done by checking that the values found by the BFGS algorithm were in the scanned intervals.

The optimized unit cell parameters, calculated using the RPBE and the BEEF-vdW functionals, are shown in Table 3. The details of the calculations are presented in appendix 6.2.

Table 3. Unit cell parameters for Mordenite, calculated using the RPBE, BEEF-vdW, LDA and GGA exchange-correlation functionals.

Homogenous volume variation						
XC functional	**RPBE**			**BEEF-vdW**		
Vector	**a**	**b**	**c**	**a**	**b**	**c**
[Å]	18.570	20.887	7.672	18.444	20.745	7.620
Volume [Å^3]		2976			2915	
Volume deviation from experimental value		5.3%			3.1%	
Independent vector variation						
XC functional	**RPBE**			**BEEF**		
Vector	**a**	**b**	**c**	**a**	**b**	**c**
[Å]	18.505	20.877	7.664	18.323	20.795	7.626
Volume [Å^3]		2961			2906	
Volume deviation from experimental value [%]		4.7%			2.8%	
Demuth et al. [56] – independent vector variation						
XC functional	**LDA**			**GGA**		
Vector	**a**	**b**	**c**	**a**	**B**	**c**
[Å]	18.101	20.501	7.526	18.260	20.706	7.606
Volume [Å^3]		2793			2876	
Volume deviation from experimental value		1.2%			1.7%	

The unit cell parameters calculated, using the BEEF-vdW functional (BEEF-vdW), are in better agreement with the experimental results than the values obtained using the RPBE exchange-correlation functional (RPBE) (Table 1). This is a well-known behavior [46]. In the study of Demuth et al. [56], the unit cell of Mordenite was optimized and the DFT calculations were performed, both using an LDA [57] and a GGA [58] functionals. The results obtained with the GGA functional, which is of the same type as the RPBE functional, are similar to the results obtained in this study, with the unit vectors, being slightly overestimated.

6.2 Optimization of the unit cell

RPBE, uniform vector variation.

Scaling factor, x	Total Energy [eV]
0.950	-1070.7665
0.975	-1080.9676
1.000	-1086.9587
1.025	-1087.9941
1.050	-1081.8133

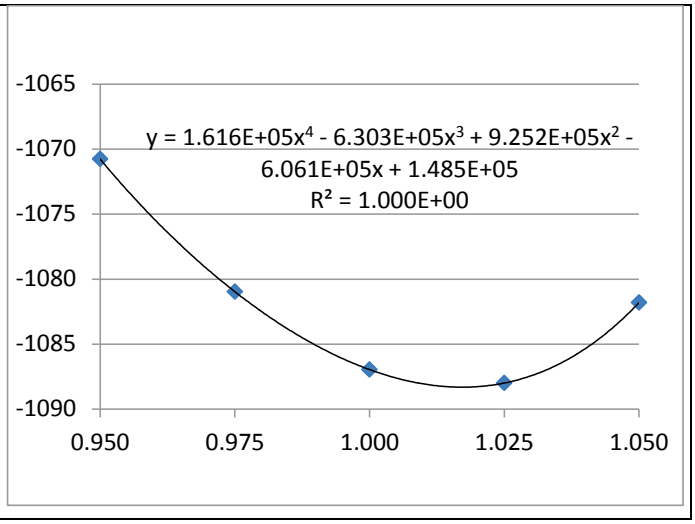

Fitting of the data with a 4th order polynomial gives:

$y=161578.66665649x^4-630281.59995880x^3+925236.37327191x^2$

$-606093.16396002x+148472.76529041$

The minimum is found, using Excel's solver:

x_{min} = 1.0172, and $E(x_{min})$=-1088,3094 eV.

The corresponding unit vectors are:

a	b	c
18.570	20.887	7.672

RPBE, independent vector variation:

Every vector is first multiplied with a scaling factor in the interval [1.00;1.06]. Corresponding to the volume of the unit cell being varied from 100% to 119%. The calculated unit vectors are:

a	b	c
18.524	20.888	7.663
Scaling vectors		
1.01469430	1.01725786	1.01605913

Next, the experimentally determined vectors are multiplied with the calculated scaling factors, varied ± 0.01. The calculated unit vectors are:

a	b	c
18.524	20.888	7.663
Scaling vectors		
1.01361386	1.01669025	1.01616688

The total energy of the unit cell with these parameters is: E=-1086.4368

BEEF-vdW, uniform vector variation.

Scaling factor, x	Total Energy [eV]
0.950	-3521.1629
0.975	-3530.2095
1.000	-3534.8269
1.025	-3534.2165
1.050	-3526.3123

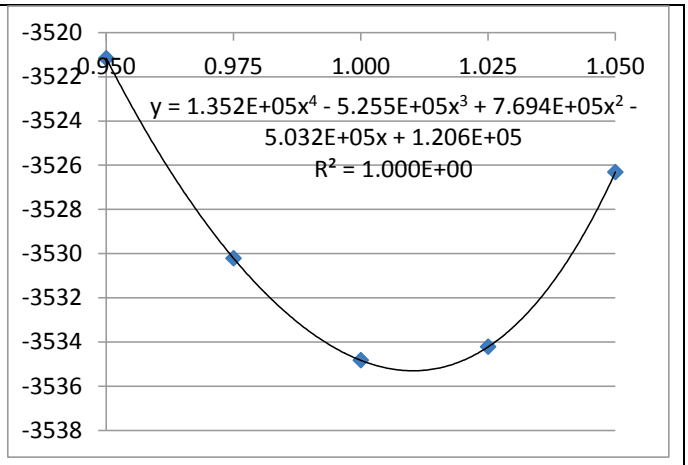

Fitting of the data with a 4th order polynomial gives:

$y = 1.35189333E+05x^4 - 5.25479466E+05x^3 + 7.69400145E+05x^2$

$- 5.03208914E+05x + 1.20564075E+05$

The minimum is found, using Excel's solver:

$x_{min} = 1.0103$, and $E(x_{min})=-3535.2979$ eV.

The corresponding unit vectors are:

a	b	c
18.444	20.745	7.620

BEEF-vdW, independent vector variation:

Every vector is first multiplied with a scaling factor in the interval [0.98;1.08]. Corresponding to the volume of the unit cell being varied from 94% to 126%. The calculated unit vectors are:

a	b	c
18.491	20.578	7.575
Scaling vectors		
1.01286335	1.00214309	1.00438285

Next, the experimentally determined vectors are multiplied with the calculated scaling factors, varied ± 0.01. The calculated unit vectors are:

a	b	c
18.323	20.795	7.626
Scaling vectors		
1.00369235	1.01270062	1.01118240

The total energy of the unit cell with these parameters is: E=-3534.5037.

RPBE, independent vector variation.

Values of x, y, z and the corresponding energies that were calculated for:

$x \in [x_{min1} - 0.01; x_{min1} + 0.01]$

$y \in [y_{min1} - 0.01; y_{min1} + 0.01]$

$z \in [z_{min1} - 0.01; z_{min1} + 0.01]$

are shown in the table below:

x	y	z	E [eV]
1.0040	1.0170	1.0160	-1086.35414977
1.0040	1.0170	1.0260	-1086.29680746
1.0040	1.0270	1.0260	-1086.22099334
1.0040	1.0070	1.0260	-1086.16013834
1.0040	1.0070	1.0060	-1085.87593213
1.0040	1.0170	1.0060	-1086.10782112
1.0040	1.0070	1.0160	-1086.15784400
1.0040	1.0270	1.0060	-1086.14701814
1.0040	1.0270	1.0160	-1086.33889119
1.0140	1.0070	1.0060	-1086.12978682
1.0140	1.0170	1.0060	-1086.28334231
1.0140	1.0170	1.0160	-1086.43196221
1.0140	1.0270	1.0060	-1086.22823297
1.0140	1.0170	1.0260	-1086.28192444
1.0140	1.0270	1.0260	-1086.12162683
1.0140	1.0070	1.0260	-1086.24780646
1.0140	1.0070	1.0160	-1086.35067030
1.0140	1.0270	1.0160	-1086.33643311
1.0240	1.0070	1.0060	-1086.22976214
1.0240	1.0170	1.0160	-1086.33645183
1.0240	1.0170	1.0260	-1086.09749348
1.0240	1.0070	1.0260	-1086.14739442
1.0240	1.0270	1.0260	-1085.82457771
1.0240	1.0170	1.0060	-1086.26816271
1.0240	1.0270	1.0160	-1086.12976334
1.0240	1.0070	1.0160	-1086.34090163
1.0240	1.0270	1.0060	-1086.13156310

The optimized values of the scaling factors and the total energy, as calculated by BFGS:

```
Warning: Desired error not necessarily achieveddue to precision loss
         Current function value: -1086.436820
         Iterations: 5
         Function evaluations: 81
         Gradient evaluations: 16
x, y, z: 1.01361386107 1.01669024536 1.01616688374
E: -1086.43682044

Min E in the list: -1086.43196221
```

The result was stable with respect to the choice of the initial guess of x, y and z.

BEEF-vdW, independent vector variation.

Values of x, y, z and the corresponding energies that were calculated for:

$x \in [x_{min1} - 0.01; x_{min1} + 0.01]$

$y \in [y_{min1} - 0.01; y_{min1} + 0.01]$

$z \in [z_{min1} - 0.01; z_{min1} + 0.01]$

are shown in the table below:

x	y	z	E [eV]
0.9940	1.0030	1.0010	-3534.03085664
0.9940	1.0130	1.0010	-3534.23686949
0.9940	1.0130	1.0110	-3534.44392996
1.0040	1.0030	1.0010	-3534.21094208
0.9940	1.0030	1.0210	-3534.25235824
0.9940	1.0030	1.0110	-3534.27679408
1.0040	1.0130	1.0010	-3534.35094585
1.0040	1.0030	1.0110	-3534.40410675
1.0040	1.0130	1.0110	-3534.50141201
1.0140	1.0030	1.0010	-3534.30963355
1.0040	1.0030	1.0210	-3534.32146894
1.0140	1.0030	1.0210	-3534.27696010
1.0140	1.0130	1.0110	-3534.44775537
0.9940	1.0230	1.0110	-3534.42005234
0.9940	1.0230	1.0210	-3534.31436264
0.9940	1.0230	1.0010	-3534.24741172
1.0040	1.0230	1.0110	-3534.41384677
1.0140	1.0130	1.0010	-3534.36229298
0.9940	1.0130	1.0210	-3534.38130640
1.0040	1.0230	1.0210	-3534.21893273
1.0140	1.0030	1.0110	-3534.43811688
1.0140	1.0230	1.0210	-3533.97205681
1.0140	1.0230	1.0110	-3534.25211435
1.0040	1.0230	1.0010	-3534.31207589
1.0040	1.0130	1.0210	-3534.36926067
1.0140	1.0130	1.0210	-3534.21957284
1.0140	1.0230	1.0010	-3534.23842019

The optimized values of the scaling factors and the total energy, as calculated by BFGS:

```
Warning: Desired error not necessarily achieveddue to precision loss
         Current function value: -3534.503742
         Iterations: 6
         Function evaluations: 171
         Gradient evaluations: 34
x, y, z: 1.00369235111 1.01270061546 1.01118239696
E: -3534.50374177

Min E in the list: -3534.50141201
```

The result was stable with respect to the choice of the initial guess of x, y and z.

6.3 DFT convergence tests

The convergence of the calculations with respect to the real grid spacing, number of k-points and the electronic temperature was tested. The test consisted of calculations of total energy of a single unit cell of purely siliceous Mordenite (Figure 15) for a number of values, for every parameter. This is the strictest test of convergence, because the adsorption energies usually converge faster, than the total energies. In the case of adsorption energies, the faster convergence is related to error cancelation, when the total energies of similar structures are subtracted from each other.

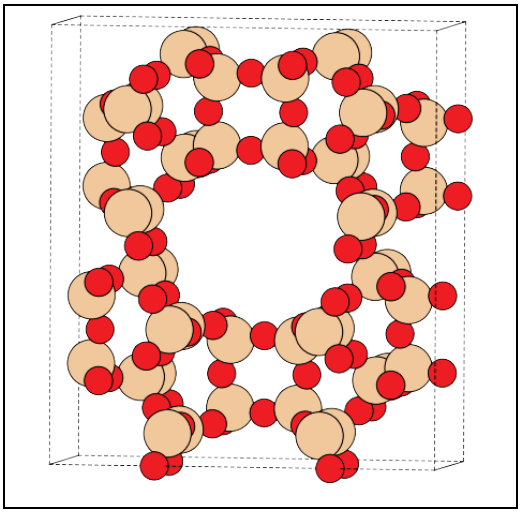

Figure 15. Test system.

The results show that the calculations are completely converged with respect to the number of k-points and the electronic temperature (Table 4). The grid spacing, used for calculation of adsorption energies, is in the region where only a relatively small change of the total energy occurs, which is sufficient for this type of calculation.

Table 4. Total energies as a function of the varied parameter.

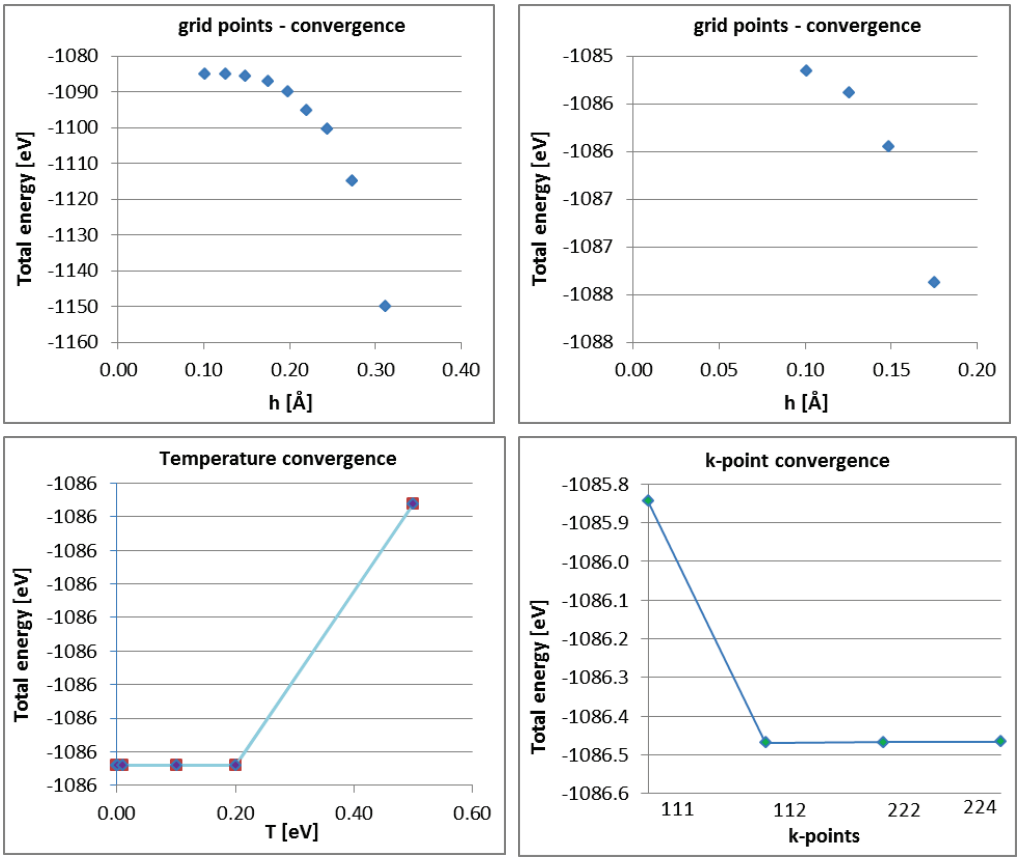

Figure 16 shows a convergence test of the formation energy with respect to the grid spacing for a gas phase reaction:

DME + CO → MA

The convergence test of the formation energy of a methyl group on Mordenite (T1-O4 site), with respect to the grid spacing is shown in Figure 17. The reaction scheme is:

DME(v) + H-Z → CH_3-Z + MeOH(v)

In both cases, a grid spacing of 0.20 Å is completely sufficient to obtain reliable values of the formation energies. Throughout this project we use a grid spacing of 0.18 Å, to minimize the error on the calculated energies arising from the incompleteness of the basis set, in which the electronic densities and wave functions are calculated.

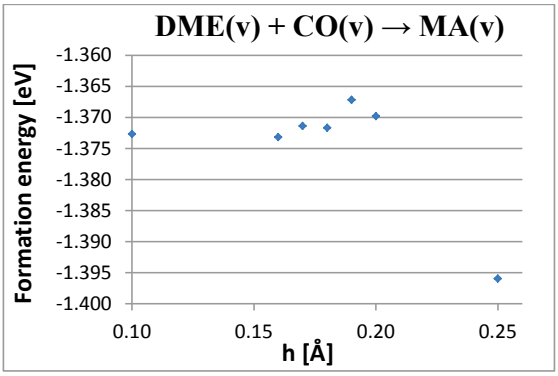

Figure 16. Convergence test of the formation energy for the gas phase reaction of DME with CO, in which MA is formed, with respect to the grid spacing.

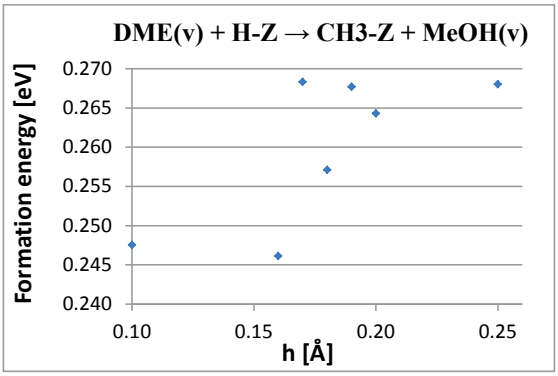

Figure 17. Convergence test of the formation energy of a methyl group on Mordenite from a Brønsted acid site and a DME molecule in vacuum, with respect to the grid spacing.

6.4 Experiments examining DME carbonylation on Mordenite

In the following subsections the raw data from the experimental work are presented.

In sections 6.6.1 and 6.6.2 the results from the experiments in which ketene was detected are shown.

The experiments in which the dependence of the MA synthesis rate on the DME concentration in CO at 10 bar are shown in sections 6.6.3 - 6.6.7.

The dependence of the MA synthesis rate on the total pressure at a fixed reactant mix, are shown in sections 6.6.7 - 6.6.13.

The rate of MA synthesis at 10 bar (2% DME in CO) and 458 K was investigated in experiment, shown in section 6.6.14.

6.4.1 Experiment 1 – Experimental detection of ketene, experiment with D_2O

Overview of the experimental conditions

Catalyst mass	Mean Temperature		Reactant Flow	Total Pressure	Feed Composition	
[g]	[°C]	[K]	[Nml/min]	[bar]	DME [%]	CO [%]
3.0006	164.76	437.91	302.3	10.00	2.0	98.0

Calibration of the reactant flow (2% DME in CO)

	Passage time [s]	**Volume [ml]**	**Flow [ml/min]**	**Normal Flow [Nml/min]**
Temperature 28.8 °C	8.66	50	337.76	297.91
MFC4 Controller	17.13	100	341.51	301.21
Setpoint 300.0	25.63	150	342.37	301.97
	33.41	200	350.19	308.87
	41.69	250	350.80	309.41
	58.72	350	348.69	307.54
	67.75	400	345.39	304.63
	75.91	450	346.79	305.87
	84.94	500	344.36	303.73
	8.65	50	338.15	298.25
	17.30	100	338.15	298.25
	25.97	150	337.89	298.02
	34.68	200	337.37	297.56
	42.77	250	341.95	301.60
	59.62	350	343.43	302.90
	68.9	400	339.62	299.55
	85.69	500	341.35	301.07
	17.03	100	343.51	302.98
	42.84	250	341.39	301.10
Average			342.7	302.30
Standard Deviation				3.7
Relative Standard Deviation [%]				1.2

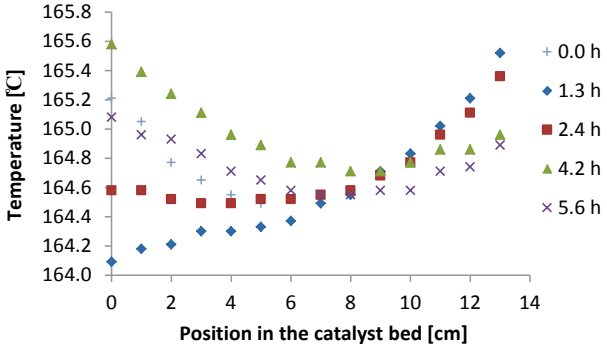

Figure 18. Temperature profile through the catalyst bed during the experiment.

6.4.2 Experiment 2 – Experimental detection of ketene, control experiment with H_2O

Overview of the experimental conditions

Catalyst mass	Mean Temperature		Reactant Flow	Total pressure	Feed Composition	
[g]	[°C]	[K]	[Nml/min]	[bar]	DME [%]	CO [%]
3.0013	165.36	438.51	299.1	10.00	2.0	98.0

Calibration of the reactant flow (2% DME in CO)

	Passage time [s]	Volume [ml]	Flow [ml/min]	Normal Flow [Nml/min]
Temperature 24.7 °C	45.24	250	323.28	296.45
MFC2 Controller	17.86	100	327.55	300.36
Setpoint 85.0	17.87	100	327.36	300.20
	44.80	250	326.45	299.36
Average			326.2	299.09
Standard Deviation				1.6
Relative Standard Deviation [%]				0.5

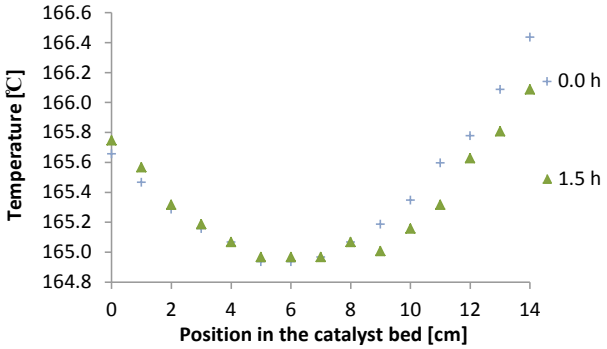

Figure 19. Temperature profile through the catalyst bed during the experiment.

6.4.3 Experiment 3 – DME carbonylation (10 bar, 0.15 % DME in CO, 438 K)

Overview of the experimental conditions

Catalyst mass	Mean Temperature		Reactant Flow	Total pressure	Feed Composition	
[g]	[°C]	[K]	[Nml/min]	[bar]	DME [%]	CO [%]
1.4999	164.49	437.64	302.0	10.00	0.15	99.85

Calibration of the CO flow

	Passage time [s]	**Volume [ml]**	**Flow [ml/min]**	**Normal Flow [Nml/min]**
Temperature 22.9 °C	48.15	250	303.74	280.25
MFC2 Controller	48.04	250	304.43	280.89
Setpoint 88.0	48.19	250	303.49	280.02
	48.29	250	302.86	279.44
	48.05	250	304.37	280.84
	48.10	250	304.05	280.54
Average			303.8	280.33
Standard Deviation				0.5
Relative Standard Deviation [%]				0.2

Calibration of the combined CO, CO/DME (2% DME) flow

	Passage time [s]	**Volume [ml]**	**Flow [ml/min]**	**Normal Flow [Nml/min]**
Temperature 22.9 °C	44.76	250	326.74	301.48
MFC2 Controller	44.72	250	327.03	301.75
Setpoint 88.0	44.79	250	326.52	301.28
MFC4 Controller	44.59	250	327.99	302.63
Setpoint 18.0	44.59	250	327.99	302.63
	44.69	250	327.25	301.95
Average			327.3	301.95
Standard Deviation				0.5
Relative Standard Deviation [%]				0.2

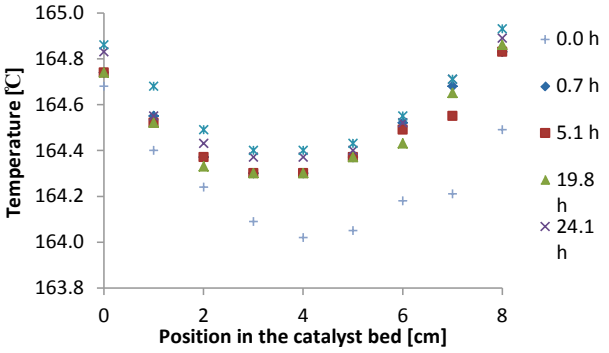

Figure 20. Temperature profile through the catalyst bed during the experiment.

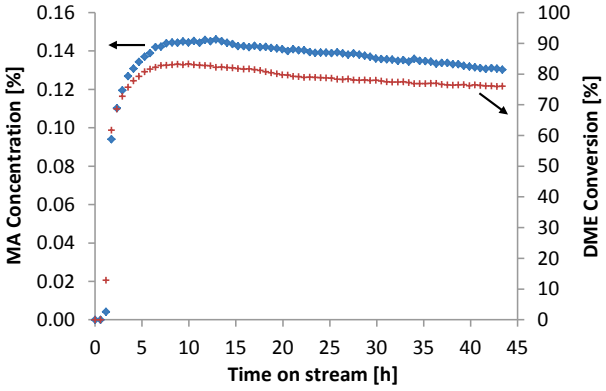

Figure 21. MA concentration and DME conversion during the experiment.

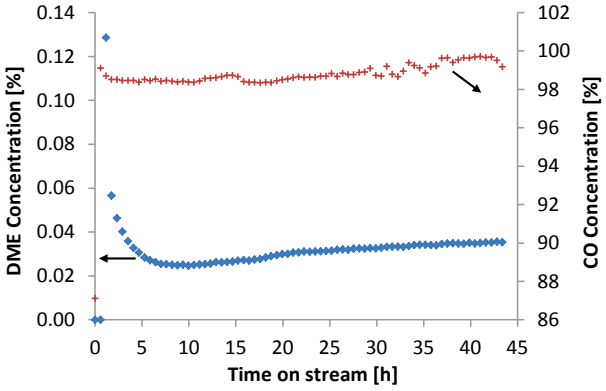

Figure 22. DME and CO concentrations during the experiment.

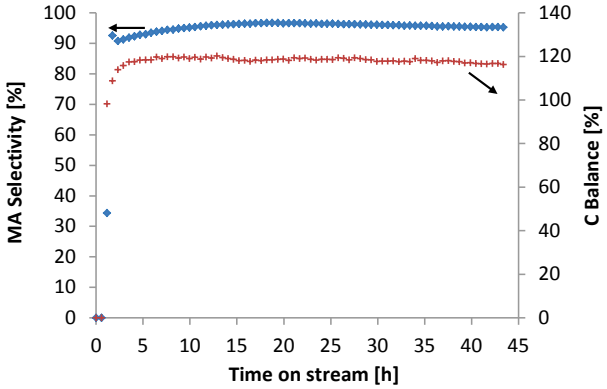

Figure 23. Selectivity towards MA based on C and the C balance during the experiment.

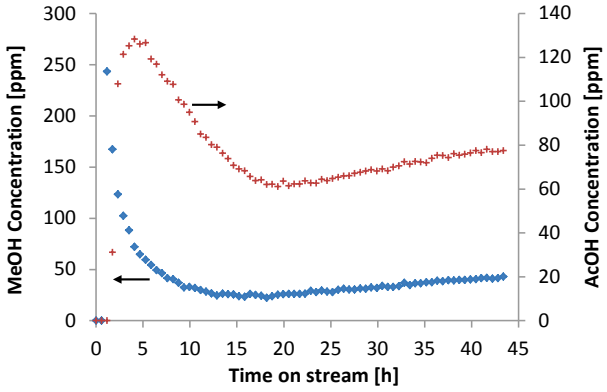

Figure 24. MeOH and AcOH concentrations during the experiment.

6.4.4 Experiment 4 – DME carbonylation (10 bar, 0.52 % DME in CO, 438 K)

Overview of the experimental conditions

Catalyst mass	Mean Temperature		Reactant Flow	Total pressure	Feed Composition	
[g]	[°C]	[K]	[Nml/min]	[bar]	DME [%]	CO [%]
1.5004	164.47	437.62	300.1	10.00	0.52	99.48

Calibration of the CO flow

	Passage time [s]	Volume [ml]	Flow [ml/min]	Normal Flow [Nml/min]
Temperature 23.1 °C	47.89	200	244.31	225.23
MFC2 Controller	47.83	200	244.62	225.51
Setpoint 71.0	59.58	250	245.47	226.30
	47.91	200	244.21	225.14
	59.67	250	245.10	225.96
	59.59	250	245.43	226.26
	47.86	200	244.46	225.37
Average			244.8	225.68
Standard Deviation				0.4
Relative Standard Deviation [%]				0.2

Calibration of the combined CO, CO/DME (2% DME) flow

	Passage time [s]	Volume [ml]	Flow [ml/min]	Normal Flow [Nml/min]
Temperature 23.2 °C	44.89	250	325.80	300.32
MFC2 Controller	44.75	250	326.82	301.26
Setpoint 71.0	44.89	250	325.80	300.32
MFC4 Controller	44.83	250	326.23	300.72
Setpoint 70.0	44.83	250	326.23	300.72
	44.77	250	326.67	301.13
Average			326.3	300.75
Standard Deviation				0.4
Relative Standard Deviation [%]				0.1

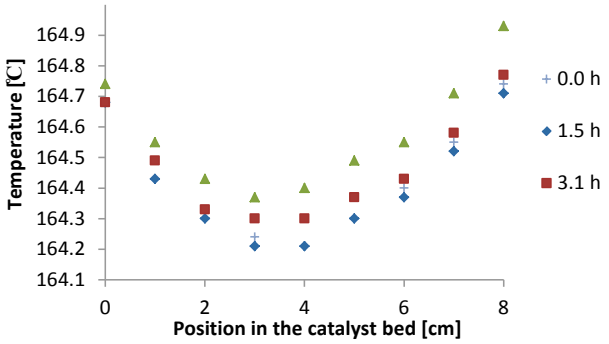

Figure 25. Temperature profile through the catalyst bed during the experiment.

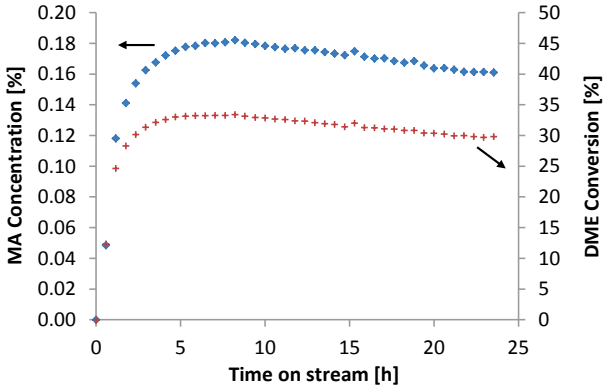

Figure 26. MA concentration and DME conversion during the experiment.

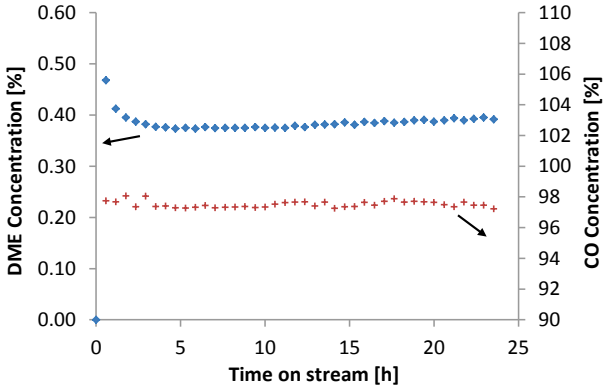

Figure 27. DME and CO concentrations during the experiment.

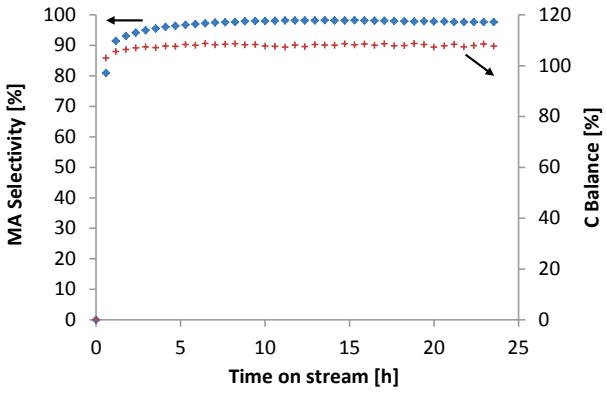

Figure 28. Selectivity towards MA based on C and the C balance during the experiment.

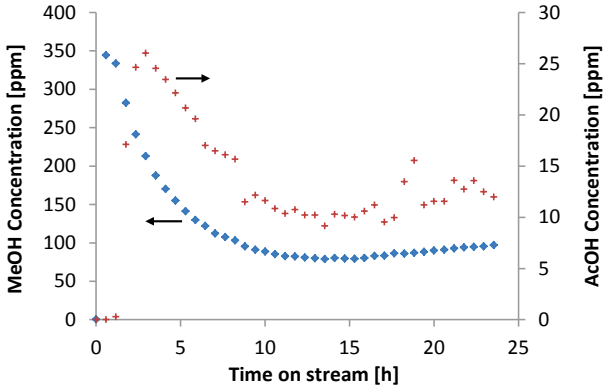

Figure 29. MeOH and AcOH concentrations during the experiment.

6.4.5 Experiment 5 – DME carbonylation (10 bar, 1.04 % DME in CO, 438 K)

Overview of the experimental conditions

Catalyst mass	Mean Temperature		Reactant Flow	Total pressure	Feed Composition	
[g]	[°C]	[K]	[Nml/min]	[bar]	DME [%]	CO [%]
1.5006	164.79	437.94	298.3	10.00	1.04	98.96

Calibration of the CO flow

	Passage time [s]	Volume [ml]	Flow [ml/min]	Normal Flow [Nml/min]
Temperature 25.4 °C	18.12	50	161.42	147.71
MFC2 Controller	35.56	100	164.51	150.54
Setpoint 41.0	53.27	150	164.73	150.74
	70.27	200	166.50	152.36
	88.33	250	165.57	151.51
	18.33	50	159.57	146.02
	35.70	100	163.87	149.95
	53.36	150	164.45	150.48
	71.02	200	164.74	150.75
	88.33	250	165.57	151.51
	124.14	350	164.93	150.93
	142.83	400	163.83	149.92
	159.49	450	165.06	151.04
	177.83	500	164.48	150.51
	17.56	50	166.57	152.43
	35.37	100	165.39	151.35
	53.06	150	165.38	151.33
	71.18	200	164.37	150.41
	88.71	250	164.86	150.86
Average			164.5	150.55
Standard Deviation				1.4
Relative Standard Deviation [%]				1.0

Calibration of the combined CO, CO/DME (2% DME) flow

	Passage time [s]	Volume [ml]	Flow [ml/min]	Normal Flow [Nml/min]
Temperature 25.2 °C	9.20	50	317.9	291.1
MFC2 Controller	17.83	100	328.1	300.4
Setpoint 41.0	26.58	150	330.1	302.2
MFC4 Controller	35.99	200	325.1	297.6
Setpoint 140.0	44.87	250	325.9	298.4
	63.58	350	322.0	294.8
	72.23	400	324.0	296.6
	80.49	450	327.1	299.4
	89.23	500	327.8	300.1
	8.78	50	333.1	305.0
	17.57	100	333.0	304.8
	26.69	150	328.8	301.0
	44.44	250	329.1	301.3
	63.19	350	324.0	296.6
	72.47	400	322.9	295.6
	81.19	450	324.2	296.8
	90.13	500	324.5	297.1
	89.61	500	326.4	298.8
	27.38	150	320.5	293.4
	45.26	250	323.1	295.8
Average			325.9	298.3
Standard Deviation				3.5
Relative Standard Deviation [%]				1.2

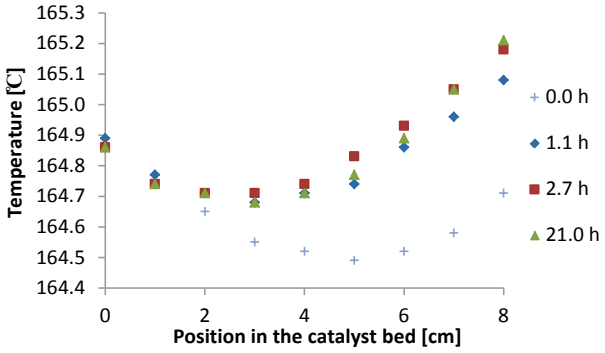

Figure 30. Temperature profile through the catalyst bed during the experiment.

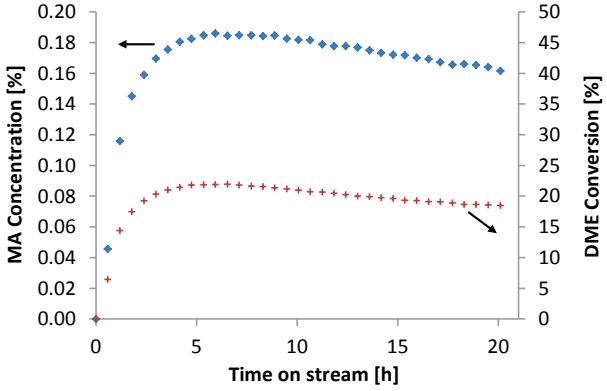

Figure 31. MA concentration and DME conversion during the experiment.

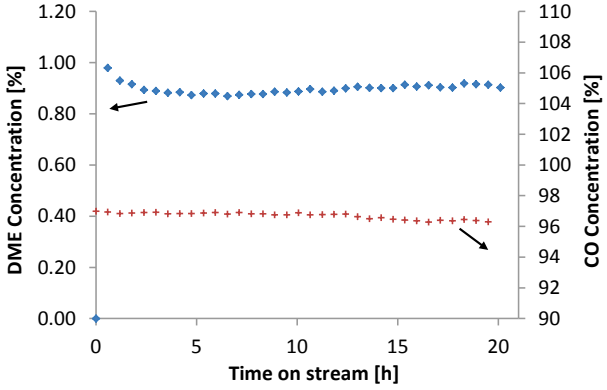

Figure 32. DME and CO concentrations during the experiment.

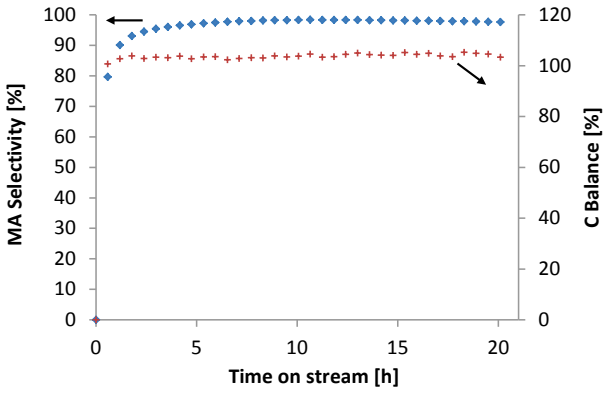

Figure 33. Selectivity towards MA based on C and the C balance during the experiment.

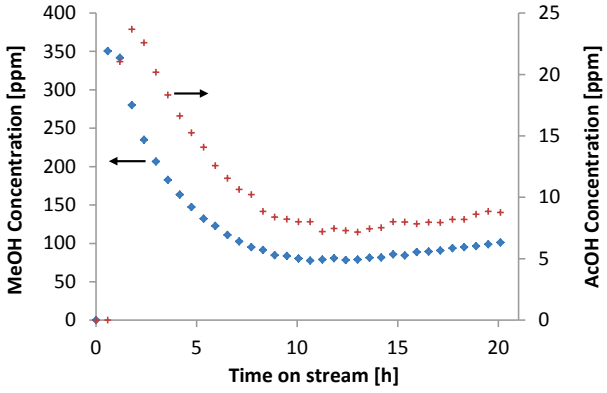

Figure 34. MeOH and AcOH concentrations during the experiment.

6.4.6 Experiment 6 – DME carbonylation (10 bar, 1.04 % DME in CO, 438 K)

Overview of the experimental conditions

Catalyst mass	Mean Temperature		Reactant Flow	Total pressure	Feed Composition	
[g]	[°C]	[K]	[Nml/min]	[bar]	DME [%]	CO [%]
0.5008	164.83	437.98	298.3	10.00	1.04	98.96

The flow was calibrated 4 days before this experiment in experiment 5.

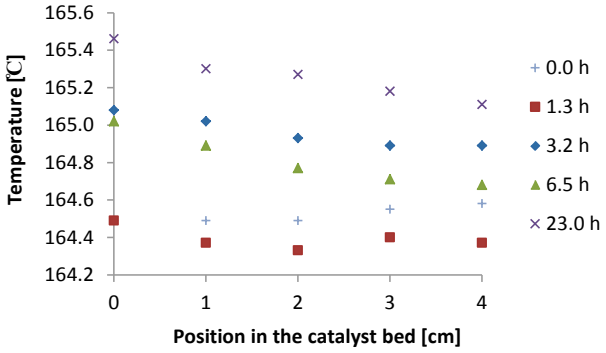

Figure 35. Temperature profile through the catalyst bed during the experiment.

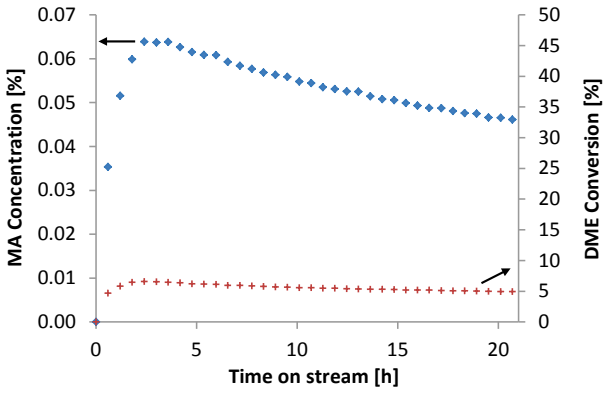

Figure 36. MA concentration and DME conversion during the experiment.

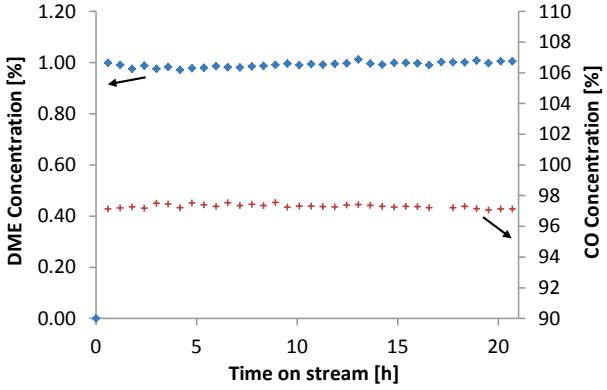

Figure 37. DME and CO concentrations during the experiment.

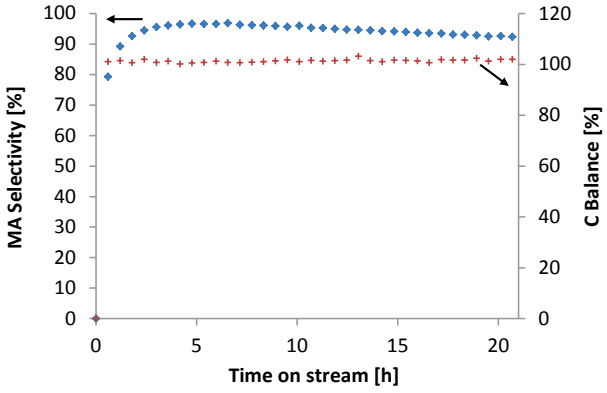

Figure 38. Selectivity towards MA based on C and the C balance during the experiment.

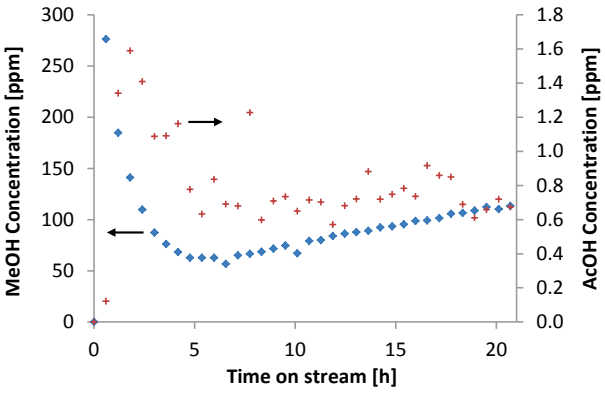

Figure 39. MeOH and AcOH concentrations during the experiment.

6.4.7 Experiment 7 – DME carbonylation (10 bar, 2.0 % DME in CO, 438 K)

Overview of the experimental conditions

Catalyst mass	Mean Temperature		Reactant Flow	Total pressure	Feed Composition	
[g]	[°C]	[K]	[Nml/min]	[bar]	DME [%]	CO [%]
1.5002	164.89	438.04	311.76	10.00	2.00	98.00

Calibration of the CO/DME (2% DME) flow

	Passage time [s]	**Volume [ml]**	**Flow [ml/min]**	**Normal Flow [Nml/min]**
Temperature 28.0 °C	25.62	150	342.51	310.67
MFC4 Controller	8.62	50	339.33	307.79
Setpoint 300.0	25.59	150	342.91	311.04
	8.65	50	338.15	306.72
	25.62	150	342.51	310.67
	16.90	100	346.15	313.98
	33.93	200	344.83	312.78
	42.35	250	345.34	313.24
	17.04	100	343.31	311.40
	33.95	200	344.62	312.59
	8.54	50	342.51	310.67
	25.51	150	343.98	312.01
	59.95	350	341.53	309.79
	77.29	450	340.60	308.94
	8.40	50	348.21	315.85
	25.30	150	346.84	314.60
	33.77	200	346.46	314.26
	16.90	100	346.15	313.98
	33.97	200	344.42	312.41
Average			343.70	311.76
Standard Deviation				2.3
Relative Standard Deviation [%]				0.7

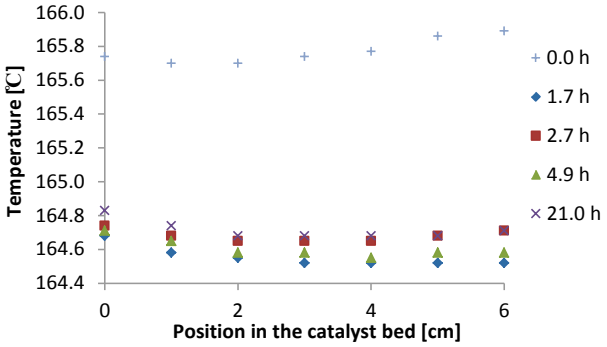

Figure 40. Temperature profile through the catalyst bed during the experiment.

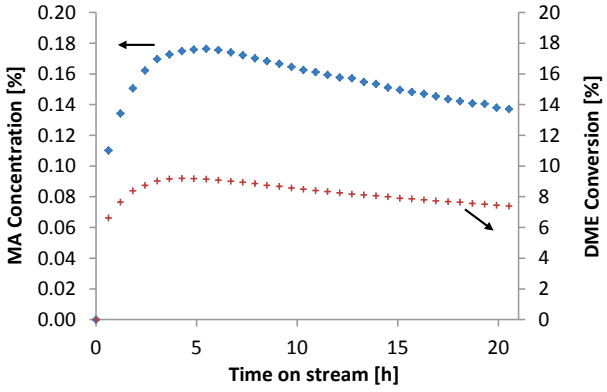

Figure 41. MA concentration and DME conversion during the experiment.

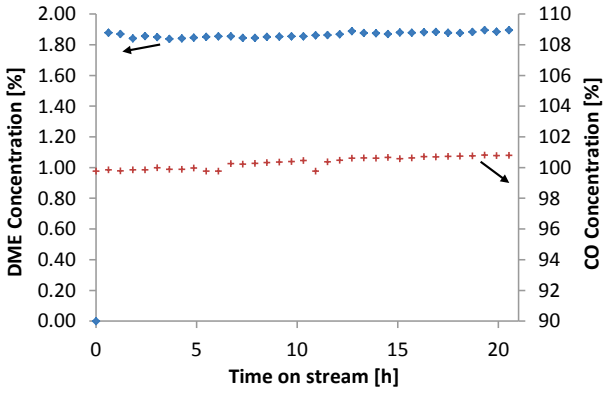

Figure 42. DME and CO concentrations during the experiment.

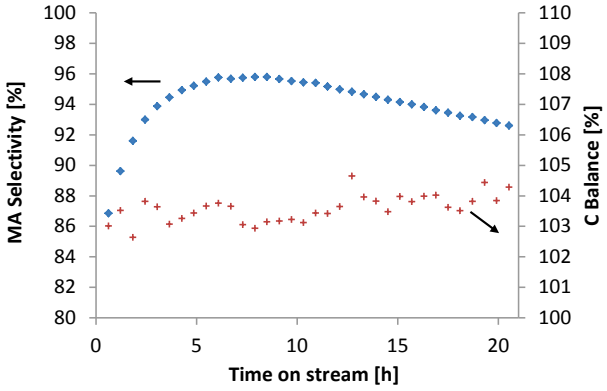

Figure 43. Selectivity towards MA based on C and the C balance during the experiment.

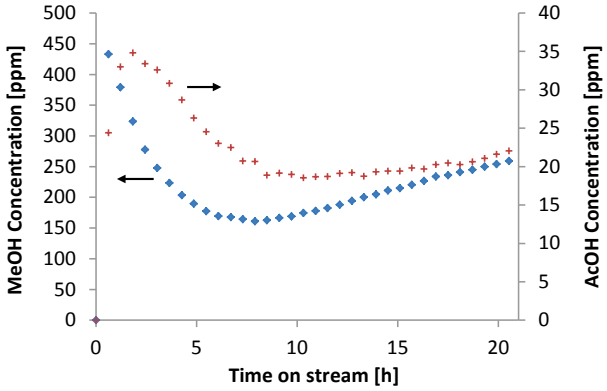

Figure 44. MeOH and AcOH concentrations during the experiment.

6.4.8 Experiment 8 – DME carbonylation (25 bar, 2.0 % DME in CO, 438 K)

Overview of the experimental conditions

Catalyst mass	Mean Temperature		Reactant Flow	Total pressure	Feed Composition	
[g]	[°C]	[K]	[Nml/min]	[bar]	DME [%]	CO [%]
1.5002	165.28	438.43	299.28	25.00	2.00	98.00

Calibration of the CO/DME (2% DME) flow

	Passage time [s]	Volume [ml]	Flow [ml/min]	Normal Flow [Nml/min]
Temperature 28.9 °C	8.84	50	330.88	299.19
MFC4 Controller	17.05	100	343.11	310.25
Setpoint 311.0	17.17	100	340.71	308.08
	42.64	250	342.99	310.14
	17.10	100	342.11	309.34
	34.29	200	341.21	308.53
	42.60	250	343.31	310.43
	8.73	50	335.05	302.96
	25.86	150	339.33	306.83
	42.89	250	340.99	308.33
	8.88	50	329.39	297.85
	34.34	200	340.71	308.08
	42.78	250	341.87	309.13
	17.13	100	341.51	308.80
	34.38	200	340.31	307.72
	60.48	350	338.54	306.12
	69.42	400	337.08	304.80
	8.79	50	332.76	300.90
	25.51	150	343.98	311.04
	42.57	250	343.55	310.65
Average			339.5	306.96
Standard Deviation				3.8
Relative Standard Deviation [%]				1.2

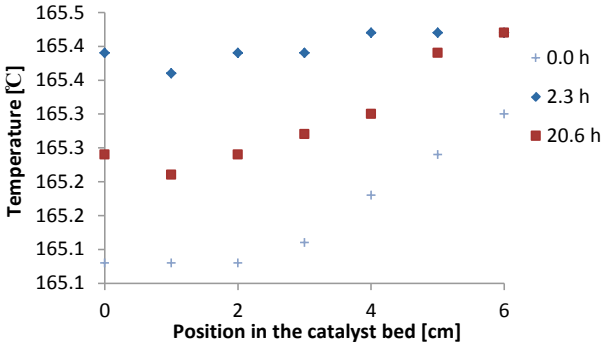

Figure 45. Temperature profile through the catalyst bed during the experiment.

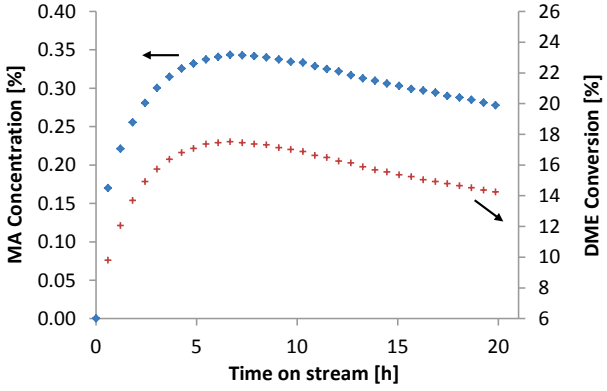

Figure 46. MA concentration and DME conversion during the experiment.

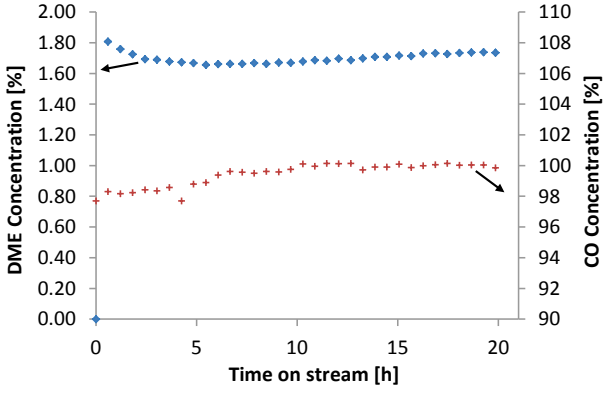

Figure 47. DME and CO concentrations during the experiment.

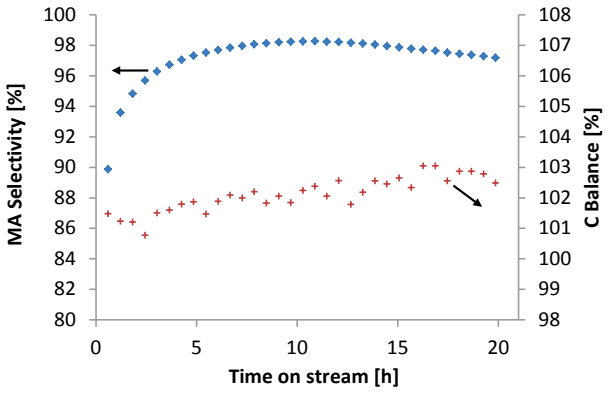

Figure 48. Selectivity towards MA based on C and the C balance during the experiment.

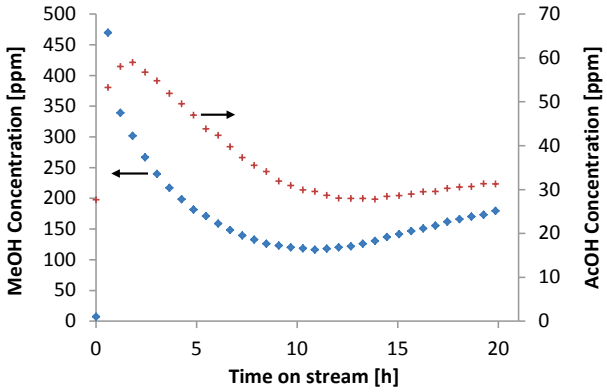

Figure 49. MeOH and AcOH concentrations during the experiment.

6.4.9 Experiment 9 – DME carbonylation (50 bar, 2.0 % DME in CO, 438 K)

Overview of the experimental conditions

Catalyst mass	Mean Temperature		Reactant Flow	Total pressure	Feed Composition	
[g]	[°C]	[K]	[Nml/min]	[bar]	DME [%]	CO [%]
1.5006	164.93	438.08	306.07	50.00	2.00	98.00

Calibration of the CO/DME (2% DME) flow

	Passage time [s]	Volume [ml]	Flow [ml/min]	Normal Flow [Nml/min]
Temperature 28.1 °C	8.81	50	332.01	301.02
MFC4 Controller	25.90	150	338.80	307.18
Setpoint 311.0	8.92	50	327.91	297.31
	34.51	200	339.03	307.39
	43.05	250	339.72	308.01
	17.37	100	336.79	305.35
	34.53	200	338.84	307.21
	42.98	250	340.27	308.51
	8.93	50	327.55	296.97
	25.97	150	337.89	306.35
	42.81	250	341.63	309.74
	17.39	100	336.40	305.00
	34.27	200	341.41	309.54
	42.83	250	341.47	309.59
	17.22	100	339.72	308.01
	34.57	200	338.44	306.85
	17.29	100	338.35	306.77
	43.00	250	340.12	308.37
Average			337.6	306.1
Standard Deviation				3.7
Relative Standard Deviation [%]				1.2

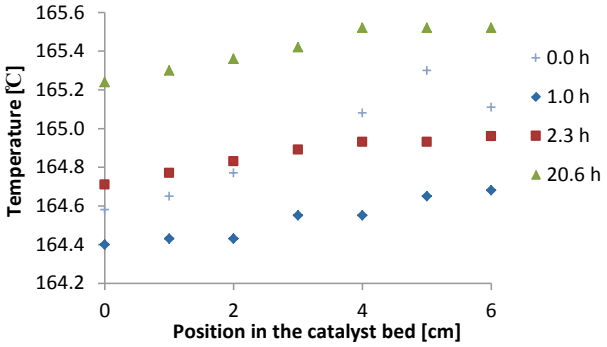

Figure 50. Temperature profile through the catalyst bed during the experiment.

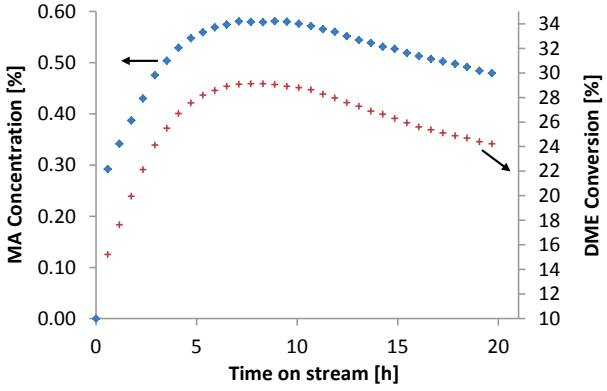

Figure 51. MA concentration and DME conversion during the experiment.

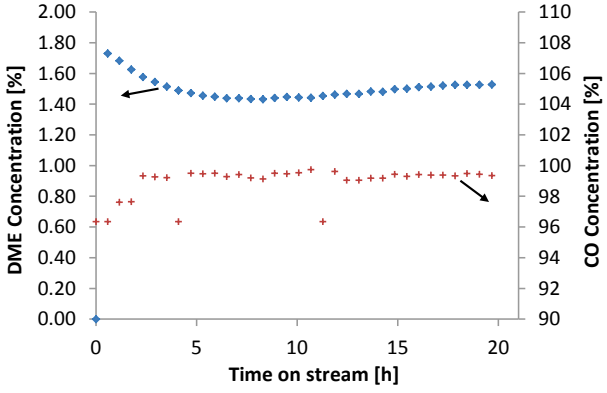

Figure 52. DME and CO concentrations during the experiment.

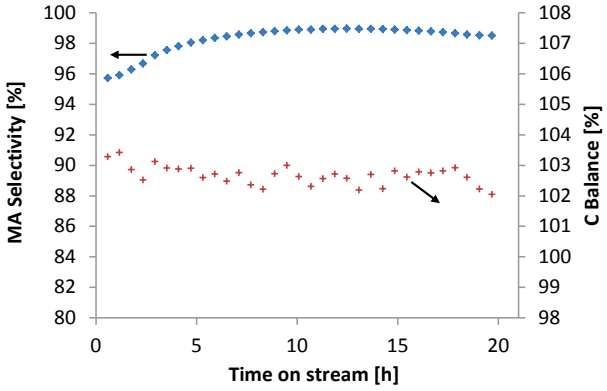

Figure 53. Selectivity towards MA based on C and the C balance during the experiment.

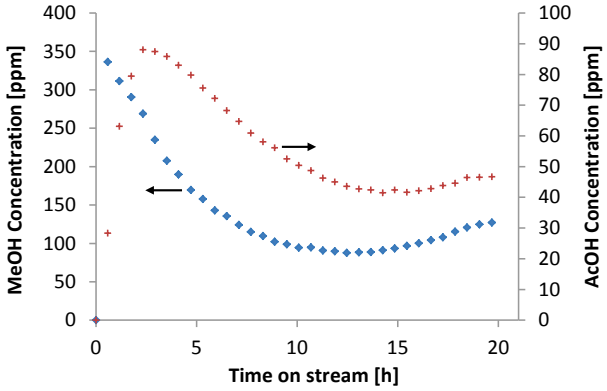

Figure 54. MeOH and AcOH concentrations during the experiment.

6.4.10 Experiment 10 – DME carbonylation (80 bar, 2.0 % DME in CO, 438 K)

Overview of the experimental conditions

Catalyst mass	Mean Temperature		Reactant Flow	Total pressure	Feed Composition	
[g]	[°C]	[K]	[Nml/min]	[bar]	DME [%]	CO [%]
1.4998	165.37	438.52	308.63	80.00	2.00	98.00

Calibration of the CO/DME (2% DME) flow

	Passage time [s]	Volume [ml]	Flow [ml/min]	Normal Flow [Nml/min]
Temperature 26.2 °C	8.77	50	333.52	304.34
MFC4 Controller	25.68	150	341.71	311.81
Setpoint 322.0	42.93	250	340.67	310.86
	17.17	100	340.71	310.90
	17.22	100	339.72	310.00
	34.66	200	337.56	308.03
	8.86	50	330.14	301.25
	26.04	150	336.98	307.50
	43.07	250	339.56	309.85
	8.66	50	337.76	308.21
	25.69	150	341.57	311.69
	42.91	250	340.83	311.01
	17.18	100	340.51	310.72
	43.09	250	339.41	309.71
	60.77	350	336.93	307.45
	87.06	500	335.98	306.58
	25.92	150	338.54	308.92
	60.89	350	336.26	306.84
	77.92	450	337.85	308.29
Average			338.2	308.6
Standard Deviation				2.6
Relative Standard Deviation [%]				0.8

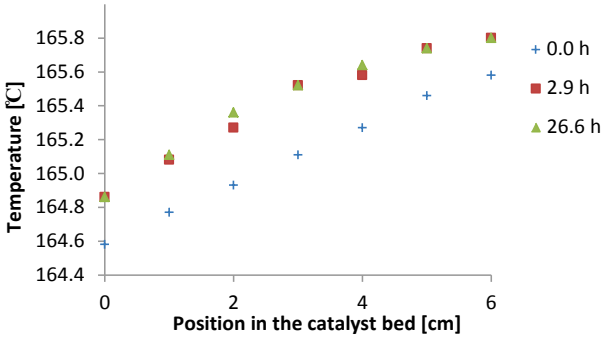

Figure 55. Temperature profile through the catalyst bed during the experiment.

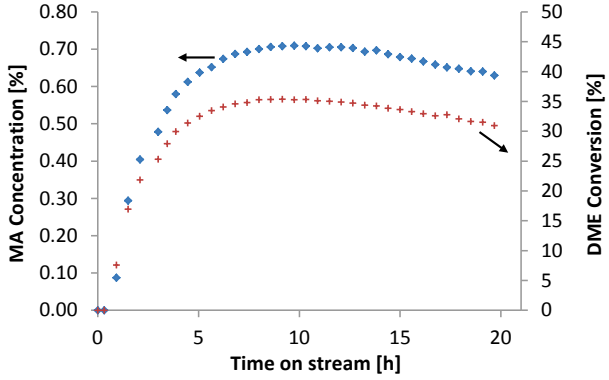

Figure 56. MA concentration and DME conversion during the experiment.

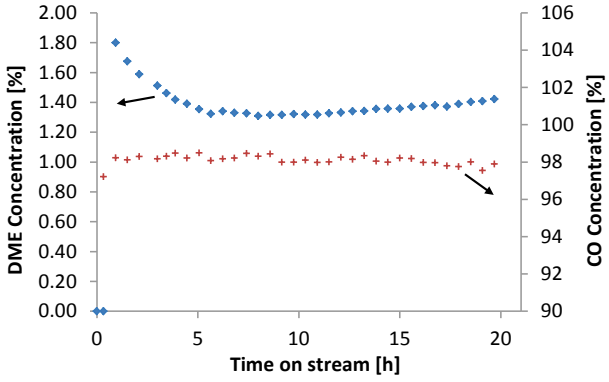

Figure 57. DME and CO concentrations during the experiment.

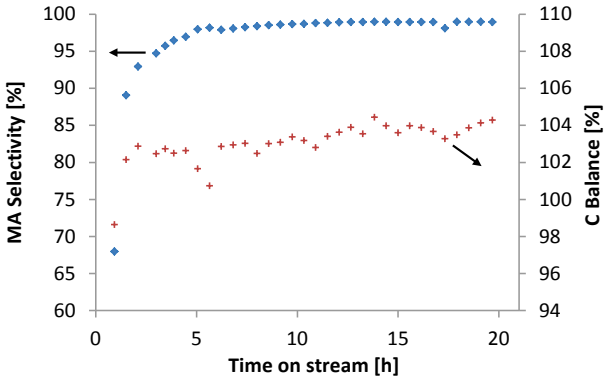

Figure 58. Selectivity towards MA based on C and the C balance during the experiment.

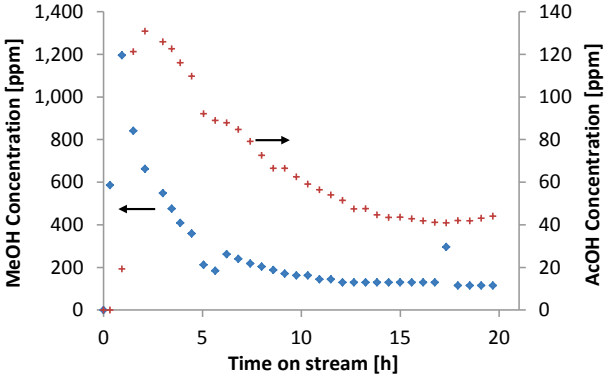

Figure 59. MeOH and AcOH concentrations during the experiment.

6.4.11 Experiment 11 – DME carbonylation (100 bar, 2.0 % DME in CO, 438 K)

Overview of the experimental conditions

Catalyst mass	Mean Temperature		Reactant Flow	Total pressure	Feed Composition	
[g]	[°C]	[K]	[Nml/min]	[bar]	DME [%]	CO [%]
1.5000	165.24	438.39	310.41	100.00	2.00	98.00

Calibration of the CO/DME (2% DME) flow

	Passage time [s]	Volume [ml]	Flow [ml/min]	Normal Flow [Nml/min]
Temperature 26.8 °C	8.53	50	342.91	312.32
MFC4 Controller	17.21	100	339.92	309.60
Setpoint 326.6	25.97	150	337.89	307.75
	42.74	250	342.19	311.66
	8.41	50	347.80	316.78
	25.69	150	341.57	311.11
	34.28	200	341.31	310.86
	17.29	100	338.35	308.17
	34.13	200	342.81	312.23
	60.51	350	338.37	308.19
	78.29	450	336.25	306.26
	87.09	500	335.86	305.90
	16.88	100	346.56	315.65
	34.37	200	340.41	310.05
	60.69	350	337.37	307.28
	78.19	450	336.68	306.65
	8.43	50	346.98	316.03
	25.73	150	341.04	310.62
	42.87	250	341.15	310.72
Average			340.8	310.41
Standard Deviation				3.1
Relative Standard Deviation [%]				1.0

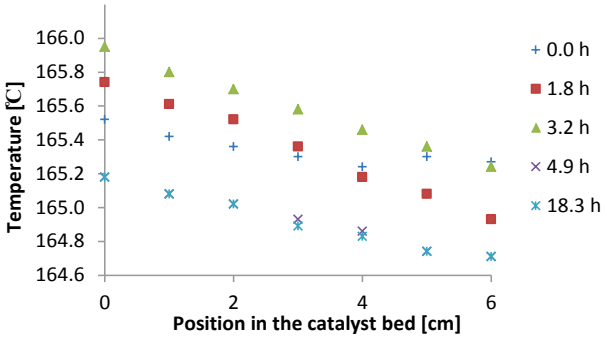

Figure 60. Temperature profile through the catalyst bed during the experiment.

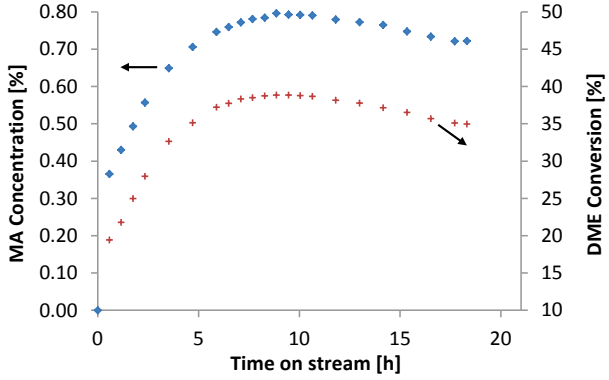

Figure 61. MA concentration and DME conversion during the experiment.

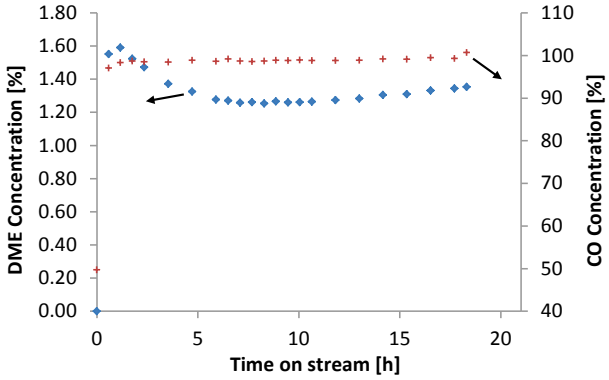

Figure 62. DME and CO concentrations during the experiment.

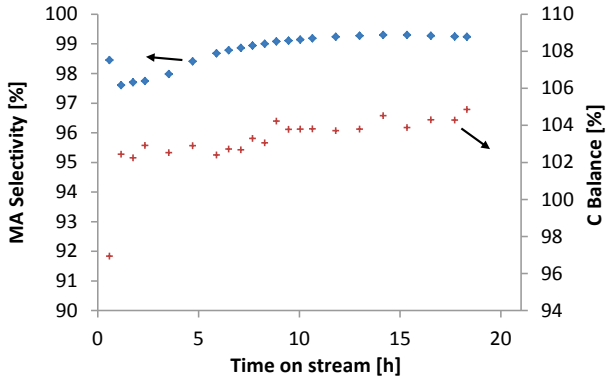

Figure 63. Selectivity towards MA based on C and the C balance during the experiment.

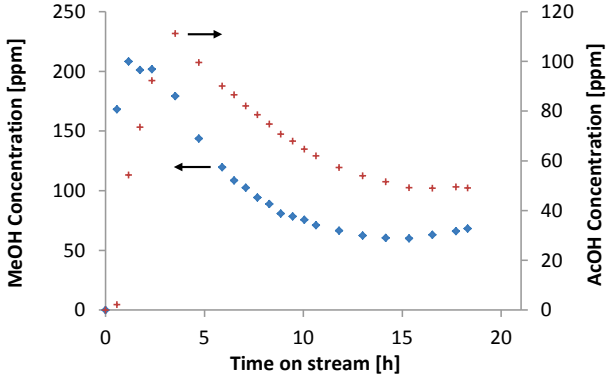

Figure 64. MeOH and AcOH concentrations during the experiment.

6.4.12 Experiment 12 – DME carbonylation (100 bar, 2.0 % DME in CO, 438 K)

Overview of the experimental conditions

Catalyst mass	Mean Temperature		Reactant Flow	Total pressure	Feed Composition	
[g]	[°C]	[K]	[Nml/min]	[bar]	DME [%]	CO [%]
0.1499	164.88	438.03	310.41	100.00	2.00	98.00

Calibration of the CO/DME (2% DME) flow

	Passage time [s]	Volume [ml]	Flow [ml/min]	Normal Flow [Nml/min]
Temperature 26.8 °C	8.53	50	342.91	312.32
MFC4 Controller	17.21	100	339.92	309.60
Setpoint 326.6	25.97	150	337.89	307.75
	42.74	250	342.19	311.66
	8.41	50	347.80	316.78
	25.69	150	341.57	311.11
	34.28	200	341.31	310.86
	17.29	100	338.35	308.17
	34.13	200	342.81	312.23
	60.51	350	338.37	308.19
	78.29	450	336.25	306.26
	87.09	500	335.86	305.90
	16.88	100	346.56	315.65
	34.37	200	340.41	310.05
	60.69	350	337.37	307.28
	78.19	450	336.68	306.65
	8.43	50	346.98	316.03
	25.73	150	341.04	310.62
	42.87	250	341.15	310.72
Average			340.8	310.4
Standard Deviation				3.1
Relative Standard Deviation [%]				1.0

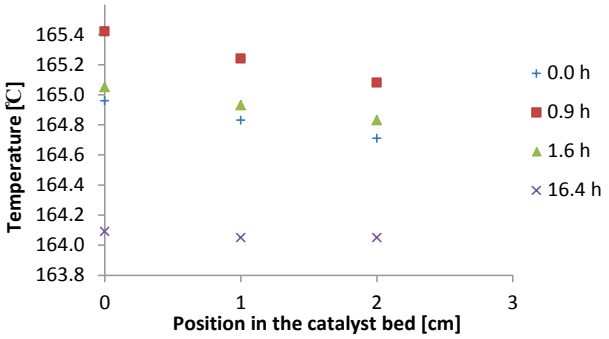

Figure 65. Temperature profile through the catalyst bed during the experiment.

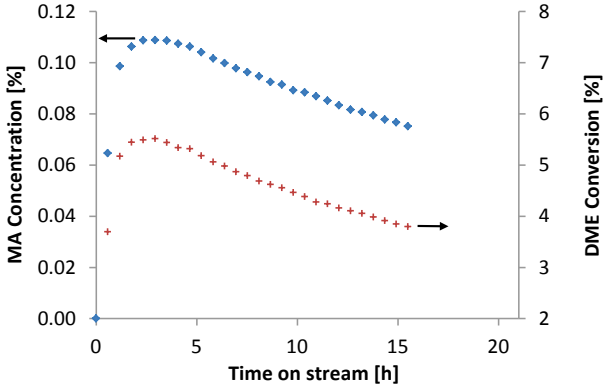

Figure 66. MA concentration and DME conversion during the experiment.

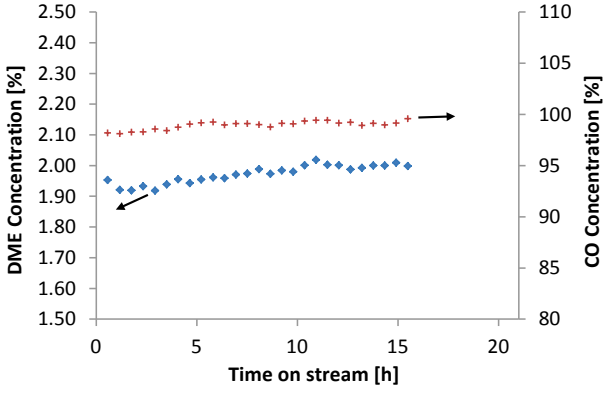

Figure 67. DME and CO concentrations during the experiment.

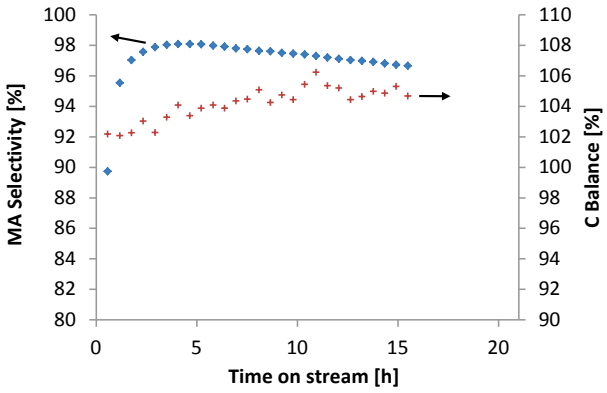

Figure 68. Selectivity towards MA based on C and the C balance during the experiment.

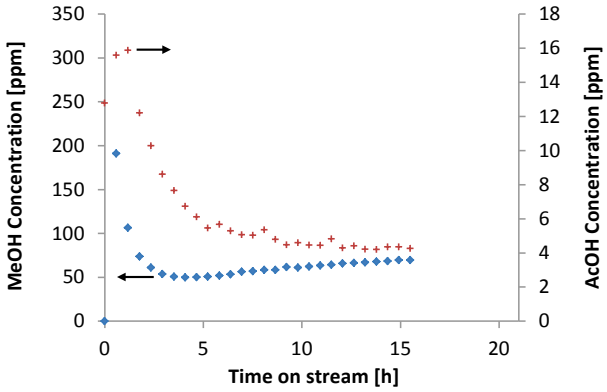

Figure 69. MeOH and AcOH concentrations during the experiment.

6.4.13 Experiment 13 – DME carbonylation (100 bar, 1.1 % DME in CO, 438 K)

Overview of the experimental conditions

Catalyst mass	Mean Temperature		Reactant Flow	Total pressure	Feed Composition	
[g]	[°C]	[K]	[Nml/min]	[bar]	DME [%]	CO [%]
1.5008	164.35	438.50	317.25	100.00	1.11	98.89

Calibration of the CO flow

	Passage time [s]	Volume [ml]	Flow [ml/min]	Normal Flow [Nml/min]
Temperature 24.5 °C	8.47	50	345.34	316.91
MFC4 Controller	16.78	100	348.63	319.93
Setpoint 327.0	25.31	150	346.70	318.16
	33.91	200	345.03	316.63
	42.47	250	344.36	316.02
	8.40	50	348.21	319.55
	16.81	100	348.01	319.36
	25.59	150	342.91	314.68
	33.81	200	346.05	317.57
	42.15	250	346.98	318.42
	8.43	50	346.98	318.42
	16.97	100	344.73	316.35
	25.68	150	341.71	313.58
	34.03	200	343.81	315.51
	42.24	250	346.24	317.74
	8.37	50	349.46	320.70
	16.87	100	346.77	318.23
	25.33	150	346.43	317.91
	33.84	200	345.74	317.29
	42.18	250	346.73	318.19
	8.69	50	336.59	308.89
	17.03	100	343.51	315.24
	25.22	150	347.94	319.30
	33.82	200	345.95	317.47
	42.03	250	347.97	319.32

Average	345.71	317.25
Standard Deviation		2.4
Relative Standard Deviation [%]		1.0

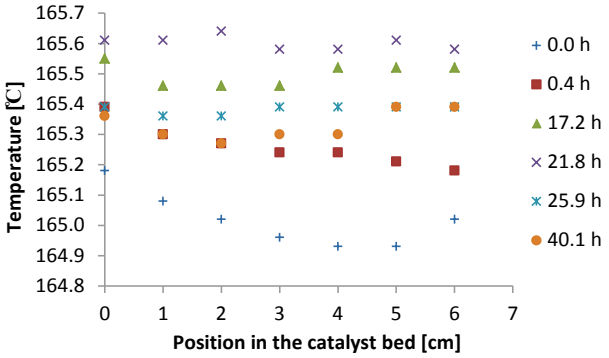

Figure 70. Temperature profile through the catalyst bed during the experiment.

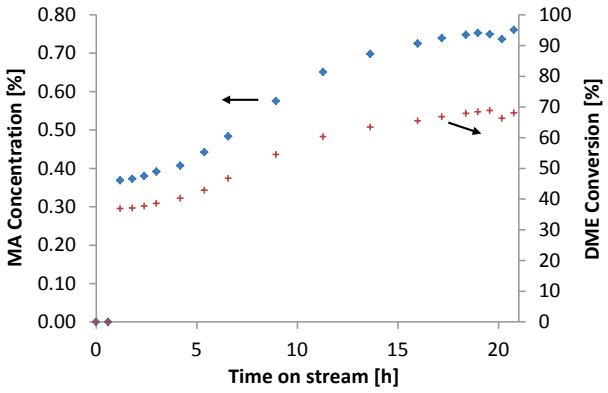

Figure 71. MA concentration and DME conversion during the experiment.

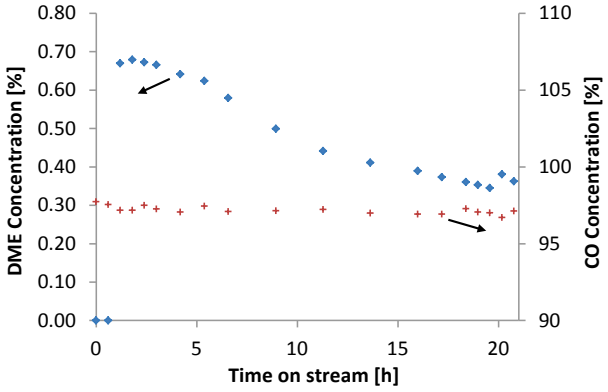

Figure 72. DME and CO concentrations during the experiment.

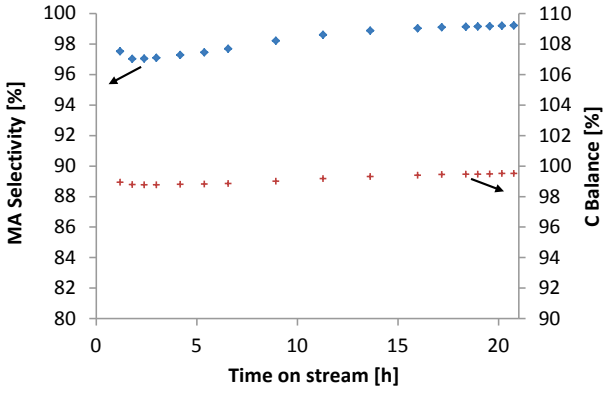

Figure 73. Selectivity towards MA based on C and the C balance during the experiment.

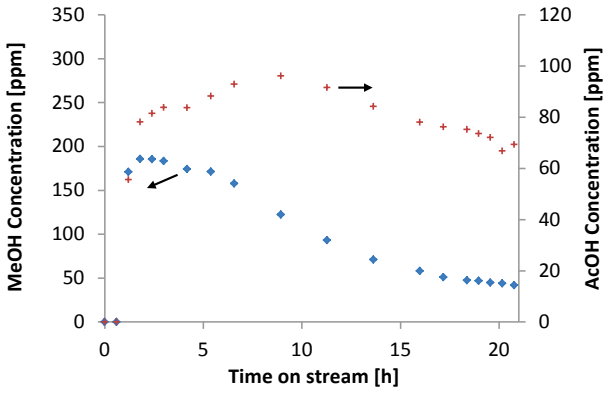

Figure 74. MeOH and AcOH concentrations during the experiment.

6.4.14 Experiment 14 – DME carbonylation (10 bar, 2.0 % DME in CO, 458 K)

Overview of the experimental conditions

Catalyst mass	Mean Temperature		Reactant Flow	Total pressure	Feed Composition	
[g]	[°C]	[K]	[Nml/min]	[bar]	DME [%]	CO [%]
1.5001	184.66	457.81	311.76	10.00	2.00	98.00

Calibration of the CO/DME (2% DME) flow

	Passage time [s]	Volume [ml]	Flow [ml/min]	Normal Flow [Nml/min]
Temperature 28.0 °C	25.62	150	342.51	310.67
MFC4 Controller	8.62	50	339.33	307.79
Setpoint 300.0	25.59	150	342.91	311.04
	8.65	50	338.15	306.72
	25.62	150	342.51	310.67
	16.90	100	346.15	313.98
	33.93	200	344.83	312.78
	42.35	250	345.34	313.24
	17.04	100	343.31	311.40
	33.95	200	344.62	312.59
	8.54	50	342.51	310.67
	25.51	150	343.98	312.01
	59.95	350	341.53	309.79
	77.29	450	340.60	308.94
	8.40	50	348.21	315.85
	25.30	150	346.84	314.60
	33.77	200	346.46	314.26
	16.90	100	346.15	313.98
	33.97	200	344.42	312.41
Average			343.7	311.76
Standard Deviation				2.3
Relative Standard Deviation [%]				0.7

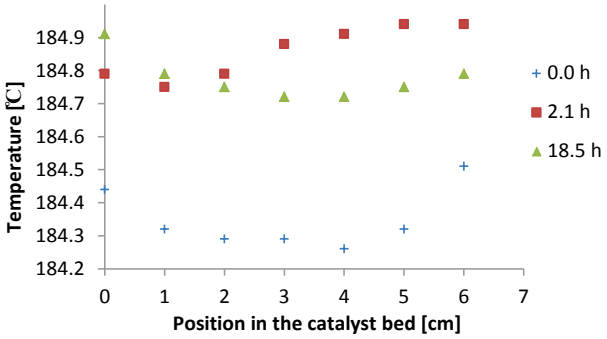

Figure 75. Temperature profile through the catalyst bed during the experiment.

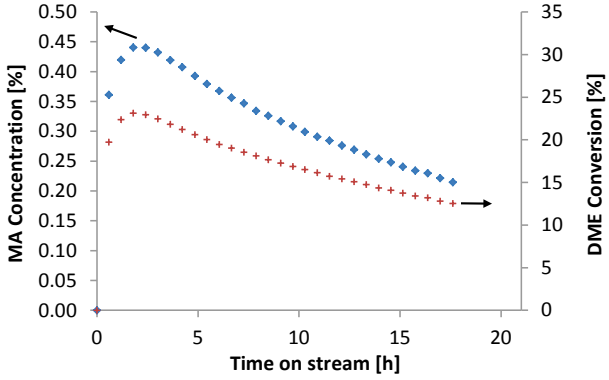

Figure 76. MA concentration and DME conversion during the experiment.

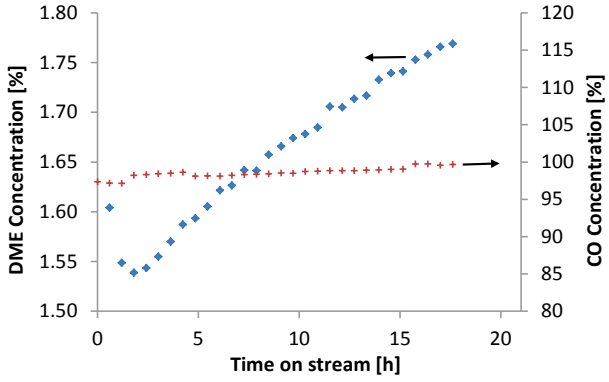

Figure 77. DME and CO concentrations during the experiment.

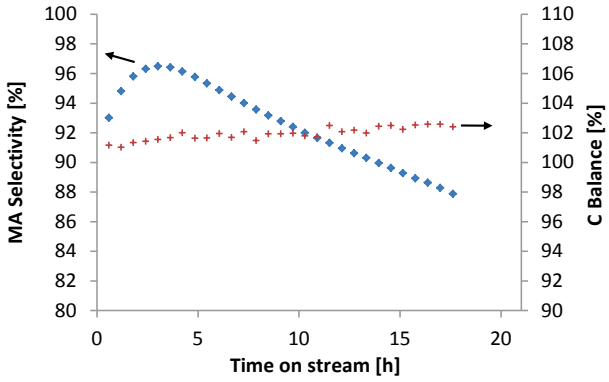

Figure 78. Selectivity towards MA based on C and the C balance during the experiment.

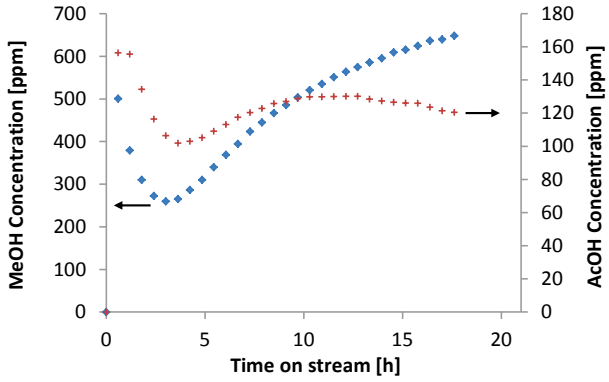

Figure 79. MeOH and AcOH concentrations during the experiment.

6.5 Raw DFT data – Adsorption energies

6.5.1 T1 – BEEF-vdW

	G	H	I	J	K	L	M	N
1	BEEF-vdW							
2	Gasphase molecules							
3	**H2**	-8.0180		**Ketene**	-59.6662			
4	**CO**	-34.7472		**H2C3O2**	-93.0328			
5	**CO2**	-54.6450		**Diketene**	-120.2008			
6	**DME**	-77.2796		**Acetic anhydride**				
7	**H2O**	-27.1803		**CH4**	-34.1407			
8	**MA**	-113.4014		**Triketene 5Ang**	-181.3411			
9	**MeOH**	-52.1316						
10	**AcOH**	-88.3097						
11	**TMO**							
12	**NH3**	-30.8488						
13								
14	**12MR Molecules**		**Total E**	**E ads**				
15	CH3-O4 CO		-3595.9629	-0.18	-34.9293			
16	CH3-O4 DME		-3638.7654	-0.45	-77.7318			
17	CH3-O4 MA		-3675.1099	-2.05	-114.0763			
18	H-O4 Ket		-3595.9057			H2O turns towards CH3-Z		
19	CH3-O4 H2O		-3588.4656					
20	**8MR Molecules**		**Total E**	**E ads**				
21	CH3-O3 CO		-3596.2270	-0.42	-35.1661			
22	CH3-O3 DME		-3638.7585	-0.42	-77.6976			
23	CH3-O3 MA		-3674.4986	-1.41	-113.4377			
24	H-O3 Ket		-3596.1274	0.20				
25								
26								
27								
28								
29								
30								
31								
32								
33								
34	**H**		**Total E**	**E relative**	**RPBE Diff**			
35	H-O1		-3535.8716	0.03				
36	H-O2		-3535.9306	-0.03				
37	H-O3		-3535.8909	0.01				
38	H-O4		-3535.9026	0.00				
39								
40								
41	**NH3_H**		**Total E**	**E Ads**	**RPBE Diff**			
42	H-O1		-3567.7949	-1.04				
43	2H-O1							
44	H-O4		-3568.1225	-1.37				
45	2H-O4							
46								
47								
48								
49								
50	**MA_H**		**Total E**	**E Ads**	**RPBE Diff**			
51	T1 O_H-O1		-3650.3246	-1.02				
52	T1 COC_H-O1		-3650.1124	-0.81				
53	T1 O_H-O4		-3650.4209	-1.12				
54	T1 COC_H-O4		-3650.1704	-0.87				
55								
56								
57								
58								
59	**DME_H**		**Total E**	**E Ads**	**RPBE Diff**			
60	H-O1		-3614.0688	-0.89				
61	H-O2		-3614.0907	-0.91				
62	H-O3		-3614.1525	-0.97				

	G	H	I	J	K	L	M	N
63	H-O4		-3614.1576	-0.98				
64								
65								
66	**MeOH_H**		**Total E**	**E Ads**	**RPBE Diff**			
67	H-O1		-3588.8169	-0.78				
68	H-O2		-3589.0084	-0.97				
69	H-O3		-3588.8693	-0.84				
70	H-O4		-3588.9290	-0.89				
71								
72								
73	**AcOH**		**Total E**	**E Ads**	**CH3 CO H2O**	**RPBE Diff**		
74	OH_H-O1		-3624.7941	-0.58	-1.83			
75	O_H-O1		-3625.0829	-0.87	-2.12			
76	OH_H-O4		-3624.8947	-0.68	-1.93			
77	O_H-O4		-3624.9991	-0.79	-2.04			
78	O_H-O4 v2 more bonds		-3625.2641	-1.05				
79								
80								
81								
82	**H2O_H**		**Total E**	**E Ads**	**RPBE Diff**			
83	H-O1		-3563.7294	-0.65				
84	H-O2		-3563.9357	-0.85				
85								
86	H-O3		-3563.8782	-0.80				
87	H-O4 v1		-3563.7702	-0.69				
88	H-O4 v2		-3563.8210	-0.74				
89								
90	**Ketene_H**		**Total E**	**E Ads**	**CH3 CO**	**RPBE Diff**		
91	H-O1_x		-3596.0305	-0.46	-0.25			
92	H-O1_z		-3596.0832	-0.51	-0.30			
93	H-O1_z neb		-3596.0929	-0.52	-0.31			
94	H-O1_z double u. c.							
95	H-O4		-3596.1356	-0.57	-0.35			
96								
97								
98								
99								
100	**CH3**		**Total E**	**DME H**	**MeOH H**	**RPBE Diff**		
101	T1-Al-O1		-3560.9099	0.14	-0.06			
102	T1-Al-O2		-3560.0497	1.00	0.80			
103	T1-Al-O3		-3560.9959	0.05	-0.14			
104	T1-Al-O4		-3561.0336	0.02	-0.18			
105								
106								
107	**CH3-O4 n H2O**		**Total E**	**E Ads**	**E Ads / H2O**	**Dist**	**RPBE Diff**	
108	1 H2O		-3588.5351	-0.32	-0.32			
109	2 H2O		-3616.0762	-0.68	-0.34			
110	3 H2O		-3643.8813	-1.31	-0.44			
111	**Double cell**							
112	1 H2O							
113	2 H2O							
114	3 H2O							
115								
116								
117	**CH3-O4 n DME**		**Total E**	**Ads**	**E Ads / DME**	**E - 12MR**	**RPBE diff**	
118	1 DME		-3638.7747	-0.46	-0.46	-0.01		
119	2 DME		-3716.7511	-1.16	-0.58			
120	2 DME ver2		-3716.3500	-0.76	-0.38			
121	2 DME ver3		-3716.4198	-0.83	-0.41			
122	3 DME		-3794.1378	-1.27	-0.42			
123	**Double**							
124	1 DME							

	G	H	I	J	K	L	M	N
125	2 DME							
126	2 DME ver2							
127	2 DME ver3							
128	3 DME							
129								
130								
131	**CH3-O4 n MA**		**Total E**	**E Ads**		**Dist**		
132	O_H							
133	OH_H							
134								
135								
136	**Acetyl carbocation**		**Total E**	**CH3 CO**	**RPBE Diff**			
137	T1-Al-O1							
138	T1-Al-O2							
139	T1-Al-O4		-3595.8458	-0.06				
140	T1-Al-O4 for neb		-3595.8726	-0.09				
141								
142								
143								
144								
145	**Acetyl**		**Total E**	**CH3 CO**	**RPBE Diff**			
146	T1-Al-O1		-3596.6576	-0.88				
147								
148								
149	T1-Al-O4		-3596.6736	-0.89				
150								
151								
152								
153								
154	**TMO+**		**Total E**	**CH3 DME**	**RPBE Diff**			
155	T1-Al_O4		-3638.3413	-0.03				
156								
157								
158	**CH3-MA**		**Total E**	**T1-CH3 CO**	**CH3 CO DME**			
159	12MR img10		-3674.1457	-1.09				
160	12MR CH3C(OCH3)2							
161								
162								
163								
164								
165								
166								
167								
168								
169								
170								
171								
172								
173								
174								
175								
176								
177								
178								
179	**12MR DMEgp**		**Total E**	**E relative**				
180	H-O4 no constraint		-3613.6925	-0.51				
181	CH3-O4 no constraint		-3638.8010	-0.49				
182								
183								
184								
185								
186								

6.5.2 T1 – RPBE

	A	B	C	D	E	F
1	RPBE					
2	Gasphase molecules					
3	**H2**	-6.7239		**H2CO**	-21.7319	
4	**CO**	-14.6220		**CH3COCH3**	-54.5129	
5	**CO2**	-22.6413		**Ketene**	-30.1969	
6	**DME**	-45.2170		**H2C3O2**	-43.4881	
7	**H2O**	-14.0263		**Diketene**	-61.1822	
8	**MA**	-61.2103		**Acetic anhydride**	-76.5716	
9	**MeOH**	-29.5451		**CH4**	-23.5124	
10	**AcOH**	-45.6034		**Triketene 5Ang**	-92.6547	
11	**TMO**					
12	**NH3**	-19.1407				
13						
14	**12MR Molecules**		**Total E**	**E ads**		
15	CH3-O4 CO		-1120.3706	-0.03	-14.6561	
16	CH3-O4 DME		-1150.9604	-0.03	-45.2459	
17	CH3-O4 MA		-1167.0323	-1.48	-61.3178	
18	H-O4 Ket		-1120.6190	0.12		
19						
20	**8MR Molecules**		**Total E**	**E ads**		
21	CH3-O3 CO		-1120.2555	0.07	-14.5485	
22	CH3-O3 DME		-1150.3771	0.55	-44.6701	
23	CH3-O3 MA		-1165.6929	-0.15	-59.9859	
24	H-O3 Ket fix. pl.		-1120.4080	0.28		
25	H-O3 Ket no constr.					
26						
27	**MOR**		**Total E**	**E relative**		
28	T1-Al		-1084.7436	0.00		
29	T2-Al		-1084.7365	0.01		
30	T3-Al		-1084.6948	0.05		
31	T4-Al		-1084.6473	0.10		
32						
33						
34	**H**		**Total E**	**E relative**		
35	T1-Al_H-O1		-1090.2731	0.03		
36	T1-Al_H-O2		-1090.3361	-0.03	points away from the channel	
37	T1-Al_H-O3		-1090.3129	-0.01	points away from the channel	
38	T1-Al_H-O4		-1090.3054	0.00	points away from the channel	
39						
40						
41	**NH3_H**		**Total E**	**E Ads**		
42	T1-Al_H-O1		-1110.3331	-0.89		
43	T1-Al H-O1 H-O4				H-O1 end	
44	T1-Al_H-O4		-1110.4598	-1.01		
45	T1-Al_2H-O4				H-O4 end	
46	T1-Al O1_O4 box					
47						
48						
49						
50	**MA_H**		**Total E**	**E Ads**		
51	T1 O_H-O1		-1152.0555	-0.54		
52	T1 COC_H-O1		-1151.7385	-0.22		
53	T1 O_H-O4		-1152.0865	-0.57		
54	T1 COC_H-O4		-1151.7457	-0.23		
55						
56						
57						

	A	B	C	D	E	F
58						
59	**DME_H**		**Total E**	**E Ads**		
60	T1-Al_H-O1		-1136.0002	-0.48		H-O 1.56 Å
61	T1-Al_H-O2		-1135.5597	-0.04		H-O 1.49 Å
62	T1-Al_H-O3		-1135.5795	-0.06		H-O 1.45 Å
63	T1-Al_H-O4		-1136.0422	-0.52		H-O 1.59 Å
64						
65						
66	**MeOH_H**		**Total E**	**E Ads**		
67	T1-Al_H-O1		-1120.3633	-0.51		H-O 1.50 Å
68	T1-Al_H-O2		-1120.2355	-0.39		H-O 1.56 Å
69	T1-Al_H-O3		-1120.0855	-0.23		H-O 1.41 Å
70	T1-Al_H-O4		-1120.4461	-0.60		H-O 1.51 Å
71						
72						
73	**AcOH**		**Total E**	**E Ads**	**CH3 CO H2O**	
74	OH_H-O1		-1136.1049	-0.20	-1.85	
75	O_H-O1		-1136.3873	-0.48	-2.13	
76	OH_H-O4		-1136.1424	-0.23	-1.89	
77	O_H-O4		-1136.3147	-0.41	-2.06	
78						
79						
80						
81						
82	**H2O_H**		**Total E**	**E Ads**		
83	T1-Al_H-O1		-1104.8425	-0.51	H-O 1.60 Å	
84	T1-Al_H-O2_DME		-1104.7152	-0.38	H-O 1.66 Å	Same end result
85	T1-Al_H-O2_MeOH		-1104.7828	-0.45	H-O 1.60 Å	
86	T1-Al_H-O3		-1104.8667	-0.54	H-O 1.55 Å	
87	T1-Al_H-O4		-1104.8722	-0.54	H-O 1.58 Å	
88						
89						
90	**Ketene_H**		**Total E**	**E Ads**	**CH3 CO**	
91	T1-Al_H-O1_x		-1120.6488	-0.15	-0.31	
92	T1-Al_H-O1_z neb		-1120.7440	-0.24	-0.41	parallel to z neb
93	T1-Al_H-O1_z double unit cell		-2226.5068	-0.29	-0.46	
94	T1-Al_H-O2		-1120.4776	0.02	-0.14	desorbed
95	T1-Al_H-O4		-1120.7315	-0.23	-0.40	
96	T1-Al_H-O4_2		-1120.7454	-0.24	-0.41	Ac-O4 start
97						
98						
99						
100	**CH3**		**Total E**	**DME H**	**MeOH H**	
101	T1-Al-O1		-1105.6456	0.33	0.18	
102	T1-Al-O2		-1104.7802	1.20	1.04	
103	T1-Al-O3		-1105.6532	0.32	0.17	
104	T1-Al-O4		-1105.7145	0.26	0.11	
105						
106						
107	**CH3-O4 n H2O**		**Total E**	**E Ads**	**E Ads / H2O**	**Dist**
108	1 H2O		-1119.8898	-0.15	-0.15	
109	2 H2O		-1134.1245	-0.36	-0.18	
110	3 H2O		-1148.6509	-0.86	-0.29	
111	**Double cell**					
112	1 H2O					
113	2 H2O					
114	3 H2O					

	A	B	C	D	E	F
115						
116						
117	**CH3-O4 n DME**		**Total E**	**E Ads**	**E Ads / DME**	**Dist**
118	1 DME		-1150.9785	-0.05	-0.05	
119	2 DME		-1196.2131	-0.06	-0.03	
120	2 DME ver2		-1195.7598	0.39	0.19	
121	2 DME ver3		-1195.7950	0.35	0.18	
122	3 DME		-1240.5583	0.81	0.27	
123	**Double**					
124	1 DME		-2256.7094	-0.06	-0.06	2.255 Å
125	2 DME		-2302.0675	-0.20	-0.10	2.668 Å, 2.680 Å
126	2 DME ver2		-2301.5469	0.32	0.16	
127	2 DME ver3		-2302.0535	-0.19	-0.10	2.784 Å, 3.331 Å
128	3 DME		-2346.5949	0.49	0.16	406 Å, 3.353 Å, 2.702
129						
130						
131	**CH3-O4 n MA**		**Total E**	**E Ads**		**Dist**
132	O_H					
133	OH_H					
134						
135						
136	**Acetyl carbocation**		**Total E**	**CH3 CO**		
137	T1-Al-O1					
138	T1-Al-O1 neb		-1120.4607	-0.12		
139	T1-Al-O2					
140	T1-Al-O4		-1120.4611	-0.12		
141	T1-Al-O4 spin polarized		-1120.4611	-0.12	Mixer	
142	T1-Al-O4 spin polarized		-1120.4610	-0.12	MixerSum	
143						
144						
145	**Acetyl**		**Total E**	**CH3 CO**		
146	T1-Al-O1		-1121.0997	-0.76		
147						
148						
149	T1-Al-O4		-1121.1265	-0.79		
150						
151						
152						
153						
154	**TMO+**		**Total E**	**CH3 DME**		
155	T1-Al_O4		-1150.5892	0.34		
156						
157						
158	**CH3-MA**		**Total E**	**CH3 CO DME**		
159	12MR img10		-1165.9785	-0.42		
160	12MR img10 fmax 0.01					
161	12MR CH3C(OCH3)2		-1166.9008	-1.35		
162						
163						
164						
165	**CH3 CO**		**Total E**	**COg + T1-CH3**		
166	T1-Al CH3-O1 CO(g)		-1120.3353	0.00		
167						
168						
169						
170						
171						

	A	B	C	D	E	F
172						
173						
174						
175						
176						
177						
178						
179	**CH3-M MA(g)**		**Total E**	**CH3-T1 DME CO**	**CH3-O4 T1 MAg**	
180	CH3-O4		-1166.1030	-0.55	0.82	f 0.42
181	CH3-O4 NEB		-1167.0280	-1.47	-0.10	fully relaxed
182						
183						
184	**Acety-M DME(g)**		**Total E**	**CH3-T1 CO DME**	**T1-Ac. DMEg**	
185	Harizontal		-1166.3105	-0.76	0.03	
186	Harizontal_NEB		-1166.2232	-0.67	0.12	
187	Vertical		-1166.0568	-0.50	0.29	
188	CH3-O		-1165.5818	-0.03	0.76	DME desorbed
189	DME-C-O		-1166.3339	-0.78	0.01	
190						
191						
192	**CO-O CH3-O**		**Total E**	**T1-CH3 COg**		
193	CO-O1_CH3-O4		-1119.0412	1.30		

6.5.3 T3 – BEEF-vdW

	Y	Z	AA	AB	AC	AD	AE	AF	AG	AH
1					BEEF-vdW					
2										
3										
4		Si Mordenite								
5		Total E	E relative							
6		-3535.4574								
7										
8	12MR Molecules		Total E	E ads						
9	AcOH_v1		-3624.1277	-0.36						
10	AcOH_v2		-3624.1719	-0.40						
11										
12	CO_v1		-3570.3096	-0.11						
13	CO_v2		-3570.3226	-0.12						
14										
15	DME_v1		-3613.0332	-0.30						
16	DME_v2		-3613.0680	-0.33						
17										
18	H2O_v1		-3562.7275	-0.09						
19	H2O_v2		-3562.7356	-0.10						
20										
21	Ketene_v1		-3595.3350	-0.21						
22	Ketene_v2		-3595.3846	-0.26						
23										
24	MA_v1		-3649.3576	-0.50						
25	MA_v2		-3649.3106	-0.50						
26										
27	MeOH_v1		-3587.7697	-0.18						
28	MeOH_v2		-3587.8225	-0.23						
29										
30										
31										
32										
33										
34	H		Total E	E relative		RPBE Diff				
35	H-O3		-3535.9218	0.00						
36	H-O8		-3535.7350	0.19						
37	H-O9		-3535.7555	0.17						
38										
39										
40										
41	NH3_H		Total E	E Ads	T1 Diff	RPBE Diff				
42	T3-Al-O3 = T1-Al-O3		-3568.2360	-1.47						
43	T3_2H_O3									
44	T3-Al_H-O8									
45	T3_2H_O8		-3568.1941	-1.42						
46	T3-Al_H-O9									
47	T3_2H_O9		-3567.9843	-1.21			O3 end			
48										
49										
50	MA_H		Total E	E Ads	T1 Diff	RPBE Diff				
51	T3 O_H-O3 MA horizontal		-3649.4228	-0.10						
52	T3 O_H-O3MA vertical		-3650.3321	-1.01						
53	T3 COC_H-O3		-3650.0139	-0.69						
54	T3 O_H-O8		-3649.9844	-0.66						
55	T3 COC_H-O8		-3649.9025	-0.58						
56	T3 O_H-O9		-3649.8758	-0.55						
57	T3 COC_H-O9									
58										
59	DME on H		Total E	E Ads	T1 Diff	RPBE Diff				
60	O3		-3614.1870	-0.99						
61	O8		-3613.9511	-0.75						
62	O9		-3613.9574	-0.76						
63										
64										
65										
66	MeOH_H		Total E	E Ads	T1 Diff	RPBE Diff				
67	T3-Al-O3 v1		-3588.9726	-0.92						
68	T3-Al-O3 v2		-3589.0580	-1.00						
69	T3-Al-O3 v3		-3589.1407	-1.09						
70	O8		-3588.9578	-0.90						
71	O9		-3588.9332	-0.88						
72										
73	AcOH		Total E	E Ads	T1 Diff	RPBE Diff				
74	T3_O_H-O3		-3625.0935	-0.86						
75	T3_O_H-O3 v2 more bonds		-3625.1317	-0.90						
76	T3_OH_H-O3		-3625.0257	-0.79						
77	T3_O_H-O8		-3624.8350	-0.60						

	Y	Z	AA	AB	AC	AD	AE	AF	AG	AH
78	T3_OH_H-O8		-3624.7045	-0.47						
79	T3_O_H-O9		-3624.9655	-0.73						
80	T3_OH_H-O9		-3624.3666	-0.14						
81										
82	**H2O_H**		**Total E**	**E Ads**	**T1 Diff**	**RPBE Diff**				
83	T3-Al-O3 v1		-3563.9390	-0.84						
84	T3-Al-O3 v2		-3563.8976	-0.80						
85	T3-Al-O3 v3		-3563.9675	-0.87						
86	O8		-3563.8076	-0.71						
87	O9		-3563.7199	-0.62						
88										
89										
90	**Ketene_H**		**Total E**	**E Ads**	**CH3 CO**	**RPBE Diff**				
91	T3-Al-O3 O up		-3596.3157	-0.73	-0.51					
92	T3-Al-O3 O up NEB *		-3596.3295	-0.74	-0.52					
93	T3-Al-O8 **		-3595.9844	-0.40	-0.18					
94	T3-Al-O9		-3595.8542	-0.27	-0.05					
95	T3-Al-O3_neb on O8		-3596.0184	-0.43	-0.21					
96	* Vert. Ketene in the center of 8MR									
97	** Horiz. Ketene in the center of 8MR									
98										
99										
100	**CH3**		**Total E**	**DME H**	**T3 O3**	**MeOH H**		**RPBE Diff**		
101	T3-Al-O3		-3561.0609	0.01	0.00	-0.19				
102	T3-Al-O8		-3560.9433	0.13	0.12	-0.07				
103	T3-Al-O9		-3560.5697	0.50	0.49	0.30				
104										
105										
106										
107	**CH3-O3 n H2O**		**Total E**	**E Ads**	**E Ads / H2O**	**Dist**	**T1 Diff**	**RPBE Diff**		
108	1 H2O		-3588.7872	-0.55	-0.55					
109	2 H2O		-3616.2261	-0.80	-0.40					
110	3 H2O		-3643.6639	-1.06	-0.35					
111	3 H2O more H bonds		-3643.820338	-1.22	-0.41					
112										
113										
114										
115										
116										
117	**CH3-O3 n DME**		**Total E**	**E Ads**	**E Ads / DME**	**Dist**	**T1 Diff**	**RPBE Diff**		
118	1 DME		-3638.7341	-0.39						
119	1 DME ver2		-3638.7187	-0.38						
120										
121										
122										
123										
124										
125										
126										
127										
128										
129										
130										
131	**CH3-O3 n MA**		**Total E**	**E Ads**		**Dist**				
132	O_H									
133	OH_H									
134										
135										
136	**Acetyl carbocation**		**Total E**	**T3 CH3 COg**	**T1 Diff**	**RPBE Diff**				
137	T3-Al-O3		-3596.3955	-0.59						
138	T3-Al-O3 used for neb		-3596.2923	-0.48						
139	T3_Al-O8 used for neb		-3596.0184	-0.21						
140										
141										
142										
143										
144										
145	**Acetyl**		**Total E**	**CH3 CO**	**T1 Diff**	**RPBE Diff**				
146	T3-Al-O3 up		-3596.8076	-1.00						
147	T3-Al-O3 down		-3596.8031	-1.00						
148	T3-Al-O8_O_up		-3596.4447	-0.64						
149	T3-Al-O8 z		-3596.4963	-0.69						
150	T3-Al-O8 -z		-3596.4846	-0.68						
151	T3-Al-O9		-3595.9642	-0.16						
152	T3-Al-O8 neb		-3596.5120	-0.70						
153										
154	**TMO+**		**Total E**	**CH3 DME**	**T1 Diff**	**RPBE Diff**				

	Y	Z	AA	AB	AC	AD	AE	AF	AG	AH
155	T3-Al_O3		-3638.4340	-0.09						
156										
157										
158	**CH3-MA**		**Total E**	**CH3 CO DME**		**RPBE Diff**				
159	8MR img5		-3673.8233	-0.74						
160	8MR img5	for neb	-3673.8221	-0.73						
161	8MR img5 rot. neb		-3673.8381	-0.75						
162										
163										
164	**CH3-MA**		**Total E**	**CH3 CO DME**						
165	T1_H-O1									
166	T1_H-O4									
167										
168										
169	**8MR DMEgp**		**Total E**	**E relative**						
170	H-O3 no constraint		-3613.7384	-0.54						
171	CH3-O3 no constraint		-3638.5271	-0.19						

6.5.4 T3 – RPBE

	O	P	Q	R	S	T	U	V	W	X
1	RPBE									
2										
3										
4										
5										
6										
7										
8										
9										
10										
11										
12										
13										
14										
15										
16										
17										
18										
19										
20										
21										
22										
23										
24										
25										
26										
27										
28										
29										
30										
31										
32										
33										
34	**H**		**Total E**	**E relative**						
35	T3-Al-O3 = T1-Al-O3		-1090.3222	0.00						
36	T3-Al_H-O8		-1090.1733	0.15						
37	T3-Al_H-O9		-1090.0707	0.25						
38										
39										
40										
41	**NH3_H**		**Total E**	**E Ads**	**T1 Diff**					
42	T3-Al-O3 = T1-Al-O3		-1110.6312	-1.17						
43	T3_2H_O3					H-O3 end				
44	T3-Al_H-O8		-1110.5396	-1.08						
45	T3_2H_O8					H-O8 end				
46	T3-Al_H-O9		-1110.3648	-0.90						
47	T3_2H_O9					H-O9 end				
48										
49										
50	**MA_H**		**Total E**	**E Ads**						
51	T3 O_H-O3 MA horizontal		-1150.4179	1.11						
52	T3 O_H-O3MA vertical		-1151.3810	0.15						
53	T3 COC_H-O3		-1151.0014							
54	T3 O_H-O8									
55	T3 COC_H-O8		-1150.8596							
56	T3 O_H-O9									
57	T3 COC_H-O9		-1150.8038							
58										
59	**DME_H**		**Total E**	**E Ads**	**T1 Diff**					
60	T3-Al-O3		-1135.6970	-0.16		H-O 1.41 Å				
61	T3-Al-O8		-1135.3910	0.15		H-O 1.36 Å				
62	T3-Al-O9		-1135.4085	0.13		H-O 1.53 Å				
63										
64										
65										
66	**MeOH_H**		**Total E**	**E Ads**	**T1 Diff**					
67	T3-Al-O3 v1		-1120.2532	-0.39		H-O Å				
68	T3-Al-O3 v2					H-O Å				
69	T3-Al-O3 v3					H-O Å				
70	T3-Al-O8		-1120.1982	-0.33						
71	T3-Al-O9		-1120.1429	-0.28						
72										
73	**AcOH**		**Total E**	**E Ads**	**T1 Diff**					
74	T3_O_H-O3		-1135.9498	-0.02						

	O	P	Q	R	S	T	U	V	W	X
75	T3_O_H-O3 v2 more bonds									
76	T3_OH_H-O3		-1135.7568	0.17						
77	T3_O_H-O8		-1135.6367	0.29						
78	T3_OH_H-O8		-1135.4873	0.44						
79	T3_O_H-O9		-1135.1626	0.76						
80	T3_OH_H-O9		-1135.1626	0.76						
81										
82	**H2O_H**		**Total E**	**E Ads**	**T1 Diff**					
83	T3-Al-O3 v1		-1104.9347	-0.59						
84	T3-Al-O3 v2					H-O 1.53 Å				
85	T3-Al-O3 v3					H-O 1.54 Å				
86	T3-Al-O8		-1104.7604	-0.41						
87	T3-Al-O9		-1104.6598	-0.31						
88										
89										
90	**Ketene_H**		**Total E**	**E Ads**	**CH3 CO**	**T1 Diff**				
91	T3-Al-O3 O up NEB		-1120.6839	-0.16	-0.35					
92	T3-Al-O8 *		-1120.2658	0.25	0.06					
93	T3-Al-O9 **		-1120.0774	0.44	0.25					
94										
95	* O8-H Vertical Ketene in the center of 8MR									
96	** O9-H Horizontal Ketene in the center of 8MR									
97										
98										
99										
100	**CH3**		**Total E**	**DME H**	**MeOH H**	**T1 Diff**				
101	T3-Al-O3		-1105.7070	0.29	0.13					
102	T3-Al-O8		-1105.6029	0.39	0.24		CH3 points in -y			
103	T3-Al-O9		-1105.2331	0.76	0.61					
104										
105										
106										
107	**CH3-O3 n H2O**		**Total E**	**E Ads**	**E Ads / H2O**	**Dist**				
108	1 H2O		-1119.9743	-0.24	-0.24					
109	2 H2O		-1133.8179	-0.06	-0.03					
110	3 H2O		-1147.7387	0.05	0.02					
111	3 H2O more H bonds		-1147.6299	0.16	0.05					
112										
113										
114										
115										
116										
117	**CH3-O3 n DME**		**Total E**	**E Ads**		**Dist**				
118	1 DME		-1150.367115	0.56						
119										
120										
121										
122										
123										
124										
125										
126										
127										
128										
129										
130										
131	**CH3-O3 n MA**		**Total E**	**E Ads**		**Dist**				
132	O_H									
133	OH_H									
134										
135										
136	**Acetyl carbocation**		**Total E**	**CH3 CO**	**T1 Diff**					
137	T3-Al-O3		-1120.7028	-0.37						
138	T3-Al-O3_neb		-1120.7072	-0.38						
139	T3-Al-O3 spin polarized		-1120.7038	-0.37						
140	T3-Al_8MR		-1120.2081	0.12						
141	T3 CH3CO gp B O8 above		-1120.7007	-0.37			COCH3-O8 end			
142										
143										
144										
145	**Acetyl**		**Total E**	**CH3 CO**	**T1 Diff**					
146	T3-Al-O3 up		-1121.0613	-0.73	0.06		H-O Å	Used for NEB		
147	T3-Al-O3 down		-1121.0758	-0.75			H-O Å			
148	T3-Al-O8_O_up		-1120.6511	-0.32			H-O Å			

	O	P	Q	R	S	T	U	V	W	X
149	T3-Al-O8 O_-z		-1120.7007	-0.37						
150	T3-Al-O8 O_z		-1120.7038	-0.37						
151	T3-Al-O9		-1120.1490	0.18						
152										
153										
154	**TMO+**		**Total E**	**CH3 DME**	**T1 Diff**					
155	T3-Al_O3		-1150.0892	0.83						
156										
157										
158	**CH3-MA**		**Total E**	**CH3 CO DME**						
159	8MR img5		-1165.0556	0.49						
160	8MR img5 fmax 0.01									
161	8MR img5 rot. Meb		-1165.0287	0.52						
162	8MR img5 rot. Neb fmax 0.01									
163										
164	**CH3-MA**		**Total E**	**CH3 CO DME**						
165	T3 8MR		-1165.0556	0.49						
166										
167										
168	**MA(g) CH3-M**		**Total E**	**T3 CH3 CO DME**	**T3 CH3 MA(g)**					
169	MA-O3 horizontal		-1165.1562		1.76					
170	MA-O3 vertical		-1166.1226		0.79					
171	MA-O3_-z		-1166.1392		0.78	Opposite side of the channel				
172	MA-O3_Ac. dw. z		-1165.8086		1.11					
173	MA-O8 horizontal		-1162.79		4.13	f_0.23				
174	MA-O8 vertical		-1166.1634		0.75					
175	MA-O8 vertical NEB 5 Ac-up		-1165.6748		1.24					
176	MA-O2-Si_T1_vertical		-1165.0641		1.85					
177										
178										
179	**MA-CH3(g)**		**Total E**	**CH3-T1 DME CO**	**T3 CH3 MA(g)**					
180	8MR formed middle		-1165.0641		1.85					
181										
182										
183	**CH3 CO(g)**		**Total E**	**COg + T3-CH3**						
184	T3-Al CH3-O3 CO(g) NEB		-1120.2369	0.09						
185										
186										
187	**DME(g) H-MOR**		**Total E**	**T3 HM DME(g)**	**T1 Difference**					
188	DME horizontal		-1135.4597	0.08		DME--H-M				
189	DME vertical		-1135.7361	-0.20		DME--H-M				
190										
191										
192	**DME(g) Ac-O3**		**Total E**	**CH3-O4 T1 CO(g) DME(g)**						
193	DME horizontal Ac_up		-1165.1985	0.35			vert. End			
194	DME vertical Ac_up		-1165.5044	0.04	f_0.16		half way out to 12MR			
195	DME horizontal Ac_down		-1165.3098	0.24			H-DME bond			
196	DME vertical Ac_down		-1164.7364	0.81						
197										
198										
199	**DME(g) Ac-O8**		**Total E**	**T3 CH3 CO(g) DME(g)**						
200	DME_horizontal_Ac_z		-1165.1526	0.39						
201	DME_horizontal_Ac_-z		-1165.2410	0.31						
202	DME_Ac_z xy		-1165.3598	0.19	f_0.11 CH3 in 12MR					

6.5.5 T2 – RPBE

	AI	AJ	AK	AL	AM	AN	AO	AP	AQ	AR
1	**RPBE**									
2										
3										
4										
5										
6										
7										
8										
9										
10										
11										
12										
13										
14										
15										
16										
17										
18										
19										
20										
21										
22										
23										
24										
25										
26										
27										
28										
29										
30										
31										
32										
33										
34	**H**		**Total E**	**E relative**						
35	T2-Al-O4 = T1-Al-O4		-1090.2225	0.12						
36	T2-Al_H-O5		-1090.3402	0.00						
37	T2-Al_H-O6		-1090.0291	0.32						
38	T2-Al_H-O7		-1090.3444	0.00						
39										
40										
41	**NH4**		**Total E**	**E Ads**						
42	T2-Al-O4 = T1-Al-O4		-1110.3315	-0.97						
43	T2_2H_O4				H-O4 end					
44	T2-Al_H-O5		-1110.5412	-1.18						
45	T2_2H_O5		-1110.5056	-1.14	H-O5 end					
46	T2-Al_H-O6		-1110.0024	-0.64						
47	T2_2H-O6				H-O6 end					
48	T2-Al_H-O7		-1110.5553	-1.19						
49	T2_2H_O7				H end					
50										
51										
52	**MA(g) H-MOR**									
53	T2-Al-O4									
54	T2-Al-O5									

	AI	AJ	AK	AL	AM	AN	AO	AP	AQ	AR
55	T2-Al-O6									
56	T2-Al-O7									
57										
58										
59	**DME on H**		**Total E**	**Ads DME,H**	**T1 Difference**					
60	T2-Al-O4		-1135.9201	-0.36	0.16	H-O 1.55 Å				
61	T2-Al-O5		-1135.6872	-0.13		H-O 1.38 Å				
62	T2-Al-O6 y					Desorption	2.83 Å			
63	T2-Al-O6 z					Desorption	2.98 Å			
64	T2-Al-O7		-1135.7811	-0.22		H-O 1.39 Å				
65										
66	**MeOH on H**		**Total E**	**Ads E MeOH**	**T1 Difference**					
67	T2-Al-O4		-1120.2959	-0.41			H-O 1.56 Å			
68	T2-Al-O5		-1120.3706	-0.48			H-O 1.56 Å			
69	T2-Al-O6_H_z		-1119.6714	0.22			H-O 1.88 Å			
70	T2-Al-O6_H_y		-1119.6879	0.20			H-O Å			
71	T2-Al-O7		-1120.4463	-0.56	0.04		H-O 1.55 Å			
72										
73										
74										
75										
76										
77										
78										
79										
80										
81										
82	**H2O on H**		**Total E**	**Ads E**	**T1 Difference**					
83	T2-Al-O4		-1104.6522	-0.28		H-O 1.64 Å				
84	T2-Al-O5		-1104.8653	-0.49		H-O 1.59 Å				
85	T2-Al-O6		-1104.3532	0.02		H-O 1.73 Å				
86	T2-Al-O7		-1104.8783	-0.51	0.03	H-O 1.60 Å				
87										
88										
89										
90	**Ketene**									
91	T2-Al-O4									
92	T2-Al-O5									
93	T2-Al-O6									
94	T2-Al-O7									
95										
96										
97										
98										
99										
100	**CH3**		**Total E**	**DMEg**	**T1 Difference**					
101	T2-Al-O4		-1105.5973	0.42		C-O 1.50 Å				
102	T2-Al-O5		-1105.7329	0.28		C-O 1.50 Å				
103	T2-Al-O6		-1104.5799	1.44		C-O 1.49 Å				
104	T2-Al-O7		-1105.7895	0.23	-0.04	C-O 1.49 Å				
105										
106										
107										
108										

	AI	AJ	AK	AL	AM	AN	AO	AP	AQ	AR
109										
110										
111										
112										
113										
114										
115										
116										
117										
118										
119										
120										
121										
122										
123										
124										
125										
126										
127										
128										
129										
130										
131										
132										
133										
134										
135										
136	**Acetyl carbocation**									
137	T2-AI-O4									
138	T2-AI-O5									
139	T2-AI-O6									
140	T2-AI-O7									
141										
142										
143										
144										
145	**Acetyl**		**Total E**	**T2 CH3 COg**	**T1 Difference**					
146	T2-AI-O4									
147	T2-AI-O5									
148	T2-AI-O6									
149	T2-AI-O7		-1121.0505	-0.64	0.15	O4 end				

6.5.6 T4 – RPBE

	BC	BD	BE	BF	BG	BH	BB	BB	BB
1				**RPBE**					
2									
3									
4									
5									
6									
7									
8									
9									
10									
11									
12									
13									
14									
15									
16									
17									
18									
19									
20									
21									
22									
23									
24									
25									
26									
27									
28									
29									
30									
31									
32									
33									
34	**H**		**Total E**	**Ads E**					
35	T4-Al-O7 = T2-Al-O7		-1090.3012	0.00					
36	T4-Al-O9 = T3-Al-O9		-1090.0253	0.28					
37	T4-Al_H-O10		-1090.1483	0.15					
38									
39									
40									
41	**NH4**		**Total E**	**Ads E**	**T1 Difference**				
42	T4-Al-O7 = T2-Al-O7		-1110.6573	-1.22					
43	T4_2H-O7					H-O7			
44	T4-Al-O9 = T3-Al-O9		-1110.2813	-0.84					
45	T4_2H-O9					H-O5 end			
46	T4-Al_H-O10		-1110.4474	-1.01					
47	T4_2H-O10					8MR opening			
48						middle			
49									
50									

	BC	BD	BE	BF	BG	BH	BB	BB	BB
51									
52									
53									
54									
55									
56									
57									
58									
59	**DME on H**		**Total E**	**Ads DME,H**	**T1 Difference**				
60	T4-Al-O7		-1135.7811	-0.26	0.26	H-O 1.40 Å			
61	T4-Al-O9		-1135.3616	0.16		H-O 1.54 Å			
62	T4-Al-O10		-1135.4871	0.03		H-O 1.40 Å			
63									
64									
65									
66	**MeOH on H**		**Total E**	**Ads E MeOH**	**T1 Difference**				
67	T4-Al-O7		-1120.3835	-0.54	0.06	H-O 1.56 Å			
68	T4-Al-O9		-1120.1183	-0.27		H-O 1.48 Å			
69	T4-Al-O10		-1120.2217	-0.38		H-O 1.53 Å			
70									
71									
72									
73									
74									
75									
76									
77									
78									
79									
80									
81									
82	**H2O on H**		**Total E**	**Ads E**	**T1 Difference**				
83	T4-Al-O7		-1104.9745	-0.65	-0.11	H-O 1.55 Å			
84	T4-Al-O9		-1104.6121	-0.28		H-O 1.60 Å			
85	T4-Al-O10		-1104.7266	-0.40		H-O 1.50 Å			
86									
87									
88									
89	**CH3**		**Total E**	**DMEg**	**T1 Difference**				
90	T4-Al-O7		-1105.7407	0.23	-0.03	C-O 1.50 Å			
91	T4-Al-O9		-1105.2076	0.77		C-O 1.51 Å			
92	T4-Al-O10		-1105.6446	0.33		C-O 1.49 Å			
93									
94									
95	**Acetyl carbocation**		**Total E**	**T4 CH3 COg**	**T1 Difference**				
96	T4-Al-O7 = T2-Al-O7								
97	T4-Al-O9 = T3-Al-O9								
98	T4-Al_H-O10								
99									
100									

	BC	BD	BE	BF	BG	BH	BB	BB	BB
101	**Ketene**		**Total E**	**T4 CH3 COg**	**T1 Difference**				
102	T4-Al-O7 = T2-Al-O7								
103	T4-Al-O9 = T3-Al-O9								
104	T4-Al_H-O10								
105									
106									
107									
108									
109									
110									
111									
112									
113									
114									
115									
116									
117									
118									
119									
120									
121									
122									
123									
124									
125									
126									
127									
128									
129									
130									
131									
132									
133									
134									
135									
136									
137									
138									
139									
140									
141									
142									
143									
144									
145	**Acetyl**		**Total E**	**T4 CH3 COg**	**T1 Difference**				
146	T4-Al-O7		-1121.1389	-0.78	0.01	H-O Å			
147	T4-Al-O9					H-O Å			
148	T4-Al-O10		-1120.9164	-0.55		H-O Å			

References

[1] J.L. Keller, Hydrocarb. Process. 58 (1979) 127.
[2] I. Wender, Fuel Process. Technol. 48 (1996) 189.
[3] R.G. Herman, Catal. Today 55 (2000) 233.
[4] G. Natta, U. Colombo, P. I, P.H. Emmett (Ed.), Catalysis 5 (1957) 131.
[5] P. Courty, D. Durand, E. Freund, A. Sugier, J. Mol. Catal. 17 (1982) 241.
[6] K.J. Smith, R.B. Anderson, J. Catal. 85 (1984) 428.
[7] W.P. Dianis, Appl. Catal. 30 (1987) 99.
[8] J.G. Nunan, C.E. Bogdan, K. Klier, K.J. Smith, C.W. Young, R.G. Herman, J. Catal. 116 (1989) 195.
[9] E. Tronconi, L. Lietti, P. Forzatti, I. Pasquon, Appl. Catal. 47 (1989) 317.
[10] P. Courty, P. Chaumette, C. Raimbault, P. Travers, Rev. Inst. Fr. Pet. 45 (1990) 561.
[11] K.J. Smith, C.W. Young, R.G. Herman, K. Klier, Ind. Eng. Chem. Res. 30 (1991) 61.
[12] J.A. Dalmon, P. Chaumette, C. Mirodatos, Catal. Today 15 (1992) 101.
[13] A. Beretta, Q. Sun, R.G. Herman, K. Klier, Ind. Eng. Chem. Res. 35 (1996) 1534.
[14] J.M. CamposMartin, J.L.G. Fierro, A. GuerreroRuiz, R.G. Herman, K. Klier, J. Catal. 163 (1996) 418.
[15] W.S. Epling, G.B. Hoflund, W.M. Hart, D.M. Minahan, J. Catal. 172 (1997) 13.
[16] M.M. Burcham, R.G. Herman, K. Klier, Ind. Eng. Chem. Res. 37 (1998) 4657.
[17] V. Mahdavi, M.H. Peyrovi, M. Islami, J.Y. Mehr, Appl. Catal., A 281 (2005) 259.
[18] J.M. Christensen, P.M. Mortensen, R. Trane, P.A. Jensen, A.D. Jensen, Appl. Catal., A 366 (2009) 29.
[19] J.M. Christensen, P.A. Jensen, N.C. Schiodt, A.D. Jensen, Chemcatchem 2 (2010) 523.
[20] J.M. Christensen, P.A. Jensen, A.D. Jensen, Ind. Eng. Chem. Res. 50 (2011) 7949.
[21] B. Voss, F. Joensen, J.B. Hansen, J. Bogild Hansen.
[22] X. San, Y. Zhang, W. Shen, N. Tsubaki, Energy Fuels 23 (2009) 2843.
[23] X. Li, X. San, Y. Zhang, T. Ichii, M. Meng, Y. Tan, N. Tsubaki, ChemSusChem 3 (2010) 1192.
[24] J. Liu, H. Xue, X. Huang, Y. Li, W. Shen, Catal. Lett. 139 (2010) 33.
[25] Y. Zhang, X. San, N. Tsubaki, Y. Tan, J. Chen, Ind. Eng. Chem. Res. 49 (2010) 5485.
[26] G. Yang, X. San, N. Jiang, Y. Tanaka, X. Li, Q. Jin, K. Tao, F. Meng, N. Tsubaki, Catal. Today 164 (2011) 425.
[27] P. Haro, P. Ollero, A.L.V. Perales, C.R. Valle, Energy 44 (2012) 891.
[28] P. Haro, P. Ollero, A.L.V. Perales, A. Gomez-Barea, Appl. Energy 102 (2013) 950.
[29] P. Cheung, A. Bhan, G.J. Sunley, E. Iglesia, Angew. Chem., Int. Ed. 45 (2006) 1617.
[30] A. Bhan, A.D. Allian, G.J. Sunley, D.J. Law, E. Iglesia, J. Am. Chem. Soc. 129 (2007) 4919.
[31] P. Cheung, A. Bhan, G.J. Sunley, D.J. Law, E. Iglesia, J. Catal. 245 (2007) 110.
[32] G.G. Volkova, L.M. Plyasova, A.N. Salanov, G.N. Kustova, T.M. Yurieva, V.A. Likholobov, Catal. Lett. 80 (2002) 175.
[33] G.G. Volkova, L.M. Plyasova, L.N. Shkuratova, A.A. Budneva, E.A. Paukshtis, M.N. Timofeeva, V.A. Likholobov, Solid superacids for halide-free carbonylation of dimethyl ether to methyl acetate, in: X.X.Y. Bao (Ed.) Natural Gas Conversion Vii, 2004, p. 403.
[34] C. Baerlocher, L.B. McCusker, Database of Zeolite Structures, in, 2012.
[35] J.L. Schlenker, J.J. Pluth, J.V. Smith, Mater. Res. Bull. 13 (1978) 169.
[36] M. Boronat, C. Martinez-Sanchez, D. Law, A. Corma, J. Am. Chem. Soc. 130 (2008) 16316.
[37] M. Boronat, C. Martinez, A. Corma, Phys. Chem. Chem. Phys. 13 (2011) 2603.

[38] J.L. Liu, H.F. Xue, X.M. Huang, P.H. Wu, S.J. Huang, S.B. Liu, W.J. Shen, Chin. J. Catal. 31 (2010) 729.
[39] H.F. Xue, X.M. Huang, E.S. Zhan, M. Ma, W.J. Shen, Catal. Commun. 37 (2013) 75.
[40] P. Hohenberg, W. Kohn, Phys. Rev. B 136 (1964) B864.
[41] W. Kohn, L.J. Sham, Phys. Rev. 140 (1965) 1133.
[42] J.J. Mortensen, L.B. Hansen, K.W. Jacobsen, Phys. Rev. B 71 (2005).
[43] J. Enkovaara, C. Rostgaard, J.J. Mortensen, J. Chen, M. Dulak, L. Ferrighi, J. Gavnholt, C. Glinsvad, V. Haikola, H.A. Hansen, H.H. Kristoffersen, M. Kuisma, A.H. Larsen, L. Lehtovaara, M. Ljungberg, O. Lopez-Acevedo, P.G. Moses, J. Ojanen, T. Olsen, V. Petzold, N.A. Romero, J. Stausholm-Moller, M. Strange, G.A. Tritsaris, M. Vanin, M. Walter, B. Hammer, H. Hakkinen, G.K.H. Madsen, R.M. Nieminen, J.K. Norskov, M. Puska, T.T. Rantala, J. Schiotz, K.S. Thygesen, K.W. Jacobsen, J. Phys.: Condens. Matter 22 (2010).
[44] S.R. Bahn, K.W. Jacobsen, Comput. Sci. Eng. 4 (2002) 56.
[45] H.J. Monkhorst, J.D. Pack, Phys. Rev. B 13 (1976) 5188.
[46] J. Wellendorff, K.T. Lundgaard, A. Mogelhoj, V. Petzold, D.D. Landis, J.K. Norskov, T. Bligaard, K.W. Jacobsen, Phys. Rev. B 85 (2012).
[47] C.G. Broyden, Math. Comput. 24 (1970) 365.
[48] R. Fletcher, Comput. J. 13 (1970) 317.
[49] D. Goldfarb, Math. Comput. 24 (1970) 23.
[50] D.F. Shanno, Math. Comput. 24 (1970) 647.
[51] G. Henkelman, B.P. Uberuaga, H. Jonsson, J. Chem. Phys. 113 (2000) 9901.
[52] E. Bitzek, P. Koskinen, F. Gaehler, M. Moseler, P. Gumbsch, Phys. Rev. Lett. 97 (2006).
[53] J.M. Christensen, J.D. Grunwaldt, A.D. Jensen, J. Catal. (2015).
[54] D.B. Rasmussen, J.M. Christensen, B. Temel, F. Studt, P.G. Moses, J. Rossmeisl, A. Riisager, A.D. Jensen, Angew. Chem., Int. Ed. (2015) n/a.
[55] T. Blasco, M. Boronat, P. Concepcion, A. Corma, D. Law, J.A. Vidal-Moya, Angew. Chem., Int. Ed. 46 (2007) 3938.
[56] T. Demuth, J. Hafner, L. Benco, H. Toulhoat, J. Phys. Chem. B 104 (2000) 4593.
[57] J.P. Perdew, A. Zunger, Phys. Rev. B 23 (1981) 5048.
[58] J.P. Perdew, Y. Wang, Phys. Rev. B 45 (1992) 13244.

Department of Chemical and Biochemical Engineering
Technical University of Denmark (DTU)

Anker Engelundsvej 1
Building 101A
DK-2800 Kgs. Lyngby

Tlf. +45 4525 2525
www.chec.kt.dtu.dk